Title
The spontaneous and light-sensing neural circuits of the developing retina

Author
Arroyo, David Antonio

Publication Date
2016

Peer reviewed|Thesis/dissertation

The spontaneous and light-sensing neural circuits of the developing retina

by

David A. Arroyo

A dissertation submitted in partial satisfaction of the

requirements for

Doctor of Philosophy

in

Molecular and Cell Biology

in the

Graduate Division

of the

University of California, Berkeley

Committee in charge:

Professor Marla B. Feller, Chair
Professor Diana M. Bautista
Professor Michael R. DeWeese
Professor Daniel E. Feldman

Summer 2016

Abstract

The spontaneous and light-sensing neural circuits of the developing retina

by

David A. Arroyo

Doctor of Philosophy in Molecular and Cell Biology

University of California, Berkeley

Professor Marla B. Feller, Chair

The development of neural circuits is perhaps one of the most fascinating phenomena of nature. Neural circuits combine an intrinsic program, that manifest itself in the form of spontaneous activity and molecular markers, with input from the environment to mature into a perfect arrangement of circuits that define how we interact with the world.

The immature mammalian retina is a perfect example of the intricacies of neural circuit development. The developing retina exhibits a robust pattern of spontaneous activity, known as retinal waves. Retinal waves are necessary for proper development of the neural connections in early parts of the visual pathway. Recent research on this topic establishes that specific spatiotemporal properties of waves instruct specific aspects of visual map formation. In addition, retinal waves have recently found roles in cell differentiation, cell migration, and synapse formation. Thus, understanding the underlying mechanisms of the spatiotemporal properties of waves and exploring new ways in which waves could influence developing neural circuits will contribute to our understanding the role of spontaneous activity in developmental processes of the nervous system.

In mice during postnatal days 1-9, retinal waves are generated by cholinergic starburst amacrine cells (SACs), which are excitatory retinal interneurons at this stage. Starburst amacrine cells exhibit slow afterhyperpolarizations that are thought to set a refractory period and thus the periodicity and frequency of waves. Using an array of electrophysiological methods such as patch-clamp and multi-electrode array recordings, and calcium imaging, we showed that the 2-pore potassium channel TREK1 underlies SACs slow afterhyperpolarization and thus wave frequency. First, we found that the SACs afterhyperpolarization is physiologically and pharmacologically consistent with a slow potassium current generated by a 2-pore potassium channel. Second, gene expression analysis of SACs revealed the expression of TREK1. Lastly, either silencing the putative TREK1-activated signaling pathways or knocking out TREK1 increases the frequency of retinal waves. Our work provides an example of how molecular

mechanisms generate specific spatiotemporal properties of waves, which are important for the development of the visual system.

In addition to instructing the wiring of retinal inputs to the visual centers of the brain, retinal waves influence developmental aspects within the retina. Prior to the onset of vision, which happens after cessation of waves, the retina relies on intrinsically photosensitive retinal ganglion cells (ipRGCs) for light detection. We explored the influence of spontaneous retinal waves on the ipRGC-dependent light response of the developing retina. We combined patch-clamp recordings, calcium imaging, multi-electrode array recordings, and tracer coupling, among other methods to determine interactions between cholinergic waves and ipRGC circuits. First, we found that ipRGCs form gap junction connections with other retinal neurons, including other ipRGCs. Second, blocking cholinergic waves induces ipRGCs to form more gap junction connections. Third, blocking waves dramatically increases the number of light-responsive cells. Fourth, waves evoke dopamine release in the developing retina. Lastly, blocking dopamine signaling increases the number of light-responsive cells, similar to blocking waves. We concluded that retinal waves evoke dopamine release that act on ipRGC to down regulate their gap junction coupling. Thus, retinal waves modulate ipRGC gap junction coupling via dopaminergic signaling to regulate the overall light response of the developing retina.

To further explore the properties of the light responses of developing ipRGCs, we characterized their light-evoked calcium transients. There are 5 different types of ipRGCs identified in adult mice, and 3 physiological types in developing mice. Pooling data from a large population of ipRGCs we analyzed amplitude, latency, and response decay of ipRGC light responses. We found that although amplitude and latency exhibited a large variation across cells, they could not be used to classify cells into different subtypes of ipRGCs. In contrast, response decay showed multimodal distributions and thus potential as a classifier for developing ipRGC types. This work contributes to our understanding of light-sensing in the developing retina.

Dedicado a esos amigos que aparecieron en el camino y fueron mi familia en alma,
a mis maestros y mentores por creer en mi,
a mi familia que de alguna u otra manera fueron motivación,
a todo aquel que ha sido parte de este viaje,
y en especial a Yeruth y Gustavo por su paciencia e insipiración.
Sin todos ustedes esto no hubiese sido… gracias

Table of contents

List of Figures

Acknowledgements

Chapter I, in full, is a reprint of the material that appears in:

David A. Arroyo and Marla B. Feller. Spatiotemporal features of retinal waves instruct the wiring of the visual circuitry, Frontiers in Neural Circuits, July 2016.

The dissertation author is the primary author of this article.

Chapter II, in full, is a reprint of the material that appears in:

Kevin J. Ford, David A. Arroyo, Jeremy N. Kay, Eric E. Lloyd, Robert M. Bryan Jr., Joshua R. Sanes and Marla B. Feller. A role for TREK1 in generating the slow afterhyperpolarization in developing starburst amacrine cells, May 2013.

The dissertation author is a co-author of this article, it is included with permission from all authors.

Chapter III, in full, is a reprint of the material that appears in:

David A. Arroyo, Lowry A. Kirkby and Marla B. Feller. Retinal waves modulate an intra-retinal circuit of intrinsically photosensitive retinal ganglion cells. The Journal of Neuroscience, June 2016.

The dissertation author is the primary author of this article.

Chapter IV is original work in preparation. The dissertation author is the primary author.

I. Spatiotemporal features of retinal waves instruct the wiring of the visual circuitry

Abstract

Coordinated spontaneous activity is present in different sensory systems during early stages of development. This activity is thought to play a critical role in the development of sensory representations before the maturation of sensory experience. In the visual system, the mechanisms by which spatiotemporal properties of retinal spontaneous activity, called retinal waves, drive developmental events has been well studied. Recent advancements in pharmacological, genetic, and optogenetic manipulations have provided further understanding of the contribution of specific spatiotemporal properties of retinal waves to eye-specific segregation and retinotopic refinement of retinofugal projections. Here we review some of the recent progress in understanding the role of retinal waves in the early stages of visual system development, prior to the maturation of vision.

Introduction

The cellular and molecular mechanisms underlying the spatiotemporal properties of retinal waves are well understood (Blankenship and Feller, 2010; Kerschensteiner, 2013). There are three developmental stages of waves mediated by different forms of neurotransmission; stage 1 waves are mediated by a combination of gap junctions and cholinergic circuits (Bansal et al., 2000), stage 2 waves are cholinergic (Feller et al., 1996), and stage 3 waves are glutamatergic (Wong et al., 2000). All three stages generate waves with different spatiotemporal properties (Maccione et al., 2014), as determined *in vitro*. Waves are characterized by their speed, frequency, covered area (size), within-burst spiking frequency, intra-retina distance-dependent correlations, and inter-eye correlations. More recently it has been established that the spatiotemporal properties of stage 2 retinal waves are preserved *in vivo* and are synaptically propagated to central visual targets (Colonnese and Khazipov, 2010;Ackman et al., 2012).

It is widely accepted that retinal waves are critical for the refinement of visual maps in retinofugal targets. Retinal projections to the superior colliculus (SC) and the dorsal lateral geniculate nucleus (dLGN) are retinotopically organized and segregate into eye-specific regions in a manner dependent on retinal activity (Figures 1, 2A; Wong, 1999; Bansal et al., 2000; Huberman et al., 2008). A classic debate in this field has been whether retinal waves are permissive or instructive for driving these developmental processes (Crair, 1999; Chalupa, 2009; Feller, 2009;Maccione et al., 2014). If waves are permissive, it implies that a minimum level of activity is required for some other instructive process to drive segregation, such as gene regulation. If waves are instructive, it implies that information about the target map is contained within the pattern of action potential firing during retinal waves. However, manipulations that alter the pattern of retinal waves also change their overall firing levels, making it difficult to differentiate between instructive and permissive roles. Here we review recent efforts that have used novel manipulations, in both mouse and ferret, to restrict perturbations of specific spatiotemporal properties of waves and thus advance the understanding of their contribution to the development of the visual circuitry.

Inter-Eye Competition Instructs Eye-Specific Segregation

Inter-eye competition generated by spontaneous retinal waves was hypothesized to be instructive for eye-specific segregation of retinofugal projections (Butts et al., 2007). During retinal waves, individual retinal ganglion cells (RGCs) fire short bursts of action potentials that propagate to neighboring RGCs within a well defined region and are separated by 1–2 min of silence—hence the firing within retinotopically identified regions of the retina have stronger intra-retinal correlation than inter-retinal correlations. One of the unexpected findings of *in vivo* calcium imaging used to record activity of RGC terminals projecting to the SC was that activity of the two eyes is more correlated than would be expected by chance (Ackman et al., 2012). However, this correlation is weak and most waves occur independently.

The *β2KO* mouse is a classic model for studying the role of retinal waves in visual system development. This mouse model lacks the β2 subunit of the nicotinic acetylcholine receptor (β2-nAChR), which is required for cholinergic waves. This mouse has significantly impaired eye-specific segregation and retinotopic refinement of retinal projects to the dLGN of the thalamus and the SC. Unfortunately, there are several conflicting descriptions of β2KO retinal activity *in vit*ro, with different spatiotemporal properties reported based on recording conditions such as temperature and media used (McLaughlin et al., 2003; Sun et al., 2008;Kirkby and Feller, 2013). In contrast, sensitivity to temperature is not observed in waves of wild type (WT) mice (Stafford et al., 2009). Recent*in vivo* imaging of RGC axon terminals in the SC of *β2KO* revealed waves to be infrequent but dramatically larger and faster than waves in WT mice, and were described by the authors as "flashes" (Burbridge et al., 2014). Importantly, depolarizations induced by RGCs in *β2KO* mice were not sufficient to entrain postsynaptic SC neurons, which exhibited an activity pattern different from that of RGC axons. Hence *β2KO* have strong long-range intra-retinal correlations but weak and infrequent activity. Moreover, when flashes occur, they are likely to be correlated between the two eyes, indicating stronger inter-retinal correlations than those observed in WT (Burbridge et al., 2014).

Though these studies are consistent with the hypothesis that a lack of correlated activity between opposing retinas is important for eye-specific segregation (Figure 2B), they do not rule out the possibility that impaired map refinement in *β2KO* mice is due to an overall reduction in retinal activity. Recent studies have separated out the contributions of an overall decrease in retinal activity, the increase in inter-retinal correlations, and the disruption of the slowly propagating waves that drive local intra-retinal correlations. First, the frequency of waves is increased in the *β2KO*via intraocular injection of CP-cAMP (Burbridge et al., 2014), a manipulation known to increase the frequency of retinal waves *in vitro*(Stellwagen et al., 1999; Stellwagen and Shatz, 2002). Increasing wave frequency and thus overall wave activity improves eye-specific segregation in *β2KO*. Second, both correlated and anticorrelated inter-retinal activity were induced using optogenetic manipulations (Zhang et al., 2011). In these studies, correlated stimulation of the two retinas induced impaired eye-specific segregation while anticorrelated stimulation permitted eye-specific segregation and even partially rescued it in *β2KO* mice. These results were complemented by studies based on a transgenic mouse in which β2-nAChR subunits are knocked out exclusively from the retina starting early in development (*Rx-β2cKO*mice). In these mice local intra-retinal correlation properties of neighboring RGCs were largely maintained, but RGCs fired at low levels. This decrease in activity resulted in impaired eye

specific segregation (Xu et al., 2015). Together, these studies strongly implicate that large-scale asynchronous activity between opposite eyes instructs eye-specific segregation while the local intra-retinal correlations induced by slowly propagating activity do not (Figures 2B,C).

Ferrets provide an interesting comparison to mice for assessing whether retinal waves are instructive for eye-specific segregation. Like mice, significant disruption of stage 2 cholinergic retinal waves disrupts eye-specific segregation of retinogeniculate afferents (Huberman et al., 2008). In contrast to mice, ipsilateral and contralateral retinal afferents of ferrets project to distinct cellular laminae in the dLGN, which may indicate differences in the mechanisms underlying visual map refinement between the two species. Using an immunotoxin to ablate starburst amacrine cells, a key component for generating Stage 2 retinal waves,Speer et al. (2014) were able to disrupt both local and global features of retinal waves while maintaining eye-specific segregation, similar to a previous study (Huberman et al., 2003). In contrast to mice, they found that large scale firing and the overall level of activity were not instructive, instead, the amount of uncorrelated firing exhibited by RGCs during the inter-wave periods was detrimental to eye-specific segregation.

A new insight into how waves influence eye-specific segregation in ferrets was achieved using an enucleated ferret model (Failor et al., 2015). Monocular enucleation results in expanded ipsilateral projections in the dLGN. Pharmacologically blocking waves in the remaining eye reduces this expansion and causes abnormal fragmentation of the ipsilateral laminae. To a lesser degree, blocking waves also induces fragmentation of contralateral projections in monocularly enucleated animals. This study suggests that intra-retinal activity itself plays a role in the development of eye-specific segregation that is independent of inter-eye competition. Furthermore, single-unit spike recordings from dLGN cells showed that blocking waves in monocularly enucleated animals causes abnormal enlargement and misalignment of receptive fields, thereby matching functional connectivity of the retino-geniculate projections with the observed anatomical phenotypes.

Together, these studies indicate that in ferrets intra-retinal correlations may be more critical for targeting axons to the correct layers and may also influence eye-specific segregation, in contrast with the observations in mice (Figures 2B,D).

Local Intra-Retinal Correlations Instruct Retinotopy

In contrast to eye-specific segregation, local intra-retinal correlations induced by propagating activity are thought to be the primary feature instructing retinotopic refinement. During locally propagating activity, nearby RGCs are more correlated than distant RGCs and therefore information about retinotopy is contained within the retinal wave firing pattern (Eglen et al., 2003). The process of retinotopic refinement has been studied primarily in retinocollicular projections, though recent progress in understanding the role of waves in retinotopic refinement of retinogeniculate projections has also been made.

Several of the mouse models described above have also identified key features of retinal waves that instruct retinotopic refinement. For example, restoring the overall level of retinal activity in β2KO mice using optogenetics or intraocular injections of CP-cAMP rescued impairments in

eye-specific segregation, but not retinotopy (Zhang et al., 2011;Burbridge et al., 2014; Figure 2D), suggesting that local intra-retinal correlations rather than overall retinal activity instruct retinotopy. One of the most striking mouse models lacks β2-nAChR in the nasal and temporal retina but expression is maintained along the central dorso-ventral strip (*Retβ2-cKO*), which serves as an internal control (Burbridge et al., 2014). *In vivo* calcium imaging of retinocollicular axon terminals confirmed that these mice exhibit locally propagating waves in the central retina while waves are absent in the nasal and temporal portions of the retina. Retinocollicular projections emerging from temporal or nasal retina were diffuse, indicating a lack of retinotopic refinement, while projections emerging from central retina were normal. This finding indicates that local intra-retinal activity patterns play a central role in establishing retinotopy (Figure 2C).

The *Rx-β2cKO* retina discussed earlier exhibits lower overall activity, smaller waves with high local correlations, more variable inter-wave intervals, and lower wave amplitude as measured with calcium imaging.*Rx-β2cKO* mice have disrupted eye-specific segregation and normal retinotopy in the monocular zones, indicating that the restricted local propagation of waves is sufficient for retinotopic refinement. Interestingly, retinotopy of the binocular zones was largely impaired, indicating interdependence between eye-specific segregation and retinotopy in the binocular zone (Xu et al., 2015). A careful comparison of waves spatiotemporal patterns in various knockout models is discussed in this study.

The role of waves in the retinotopic refinement of retinogeniculate projections in ferrets has also seen recent advancements. Intraocular blockade of inhibition to enhance glutamatergic stage 3 retinal waves led to abnormally early retinotopic refinement of retinogeniculate projections, as measured anatomically and functionally (Davis et al., 2015). Based on *in vitro* experiments, blockade of inhibition increases the frequency of glutamatergic waves while maintaining local correlations (Kerschensteiner and Wong, 2008; Firl et al., 2013). These findings are rather surprising since it suggests that increased spontaneous activity prior to visual experience could potentially compensate for lack of visual experience.

It is important to note that retinal waves work in concert with molecular cues for establishing retinotopic maps (Pfeiffenberger et al., 2006; Cang et al., 2008; Ackman and Crair, 2014; Assali et al., 2014). Though recent progress in this field is too vast to review here, we want to make note of a recent study that implicates a role for retinal waves in establishing heterogeneity in visual map organization not only across animals but also across the two colliculi of a single animal. The study makes a strong case that spontaneous activity and molecular cues interact stochastically to form well-defined yet variable retinotopic maps (Owens et al., 2015).
In summary, the evidence suggests that in mice, overall activity levels and inter-eye competition are determinant for eye-specific segregation while local intra-retinal correlations determine retinotopy, with some interdependence of the two in the binocular zones of central retinal targets. In ferrets, there is additional evidence that local intra-retinal correlations also influence eye-specific segregation.

Emerging Roles of Retinal Waves in the Development of the Visual System

Most of the research on how retinal waves influence visual system development has been focused on retinofugal projections. However, there is also an interest in understanding whether retinal waves drive other aspects of visual system development. Recent studies have elucidated emerging roles for retinal waves in the development of visual circuits. In one study it was found that disrupting retinal waves increased cortical neurogenesis in the primary visual cortex while enhancing waves decreased neurogenesis (Bonetti and Surace, 2010). Another study found that eliminating the input of retinal waves to the SC resulted in migration and connectivity deficits in inhibitory interneurons of the dLGN (Golding et al., 2014). It has also been shown that elimination of retinal inputs to central targets accelerates the cortical innervation of the dLGN, yet synapse maturation was unaffected (Seabrook et al., 2013). In addition, computational models have implicated slow features of retinal waves in the establishment of complex cells in primary visual cortex (Dähne et al., 2014), and in the establishment of initial biases in orientation maps in primary visual cortex (Hagihara et al., 2015). These discoveries suggest a broad involvement of developmental spontaneous activity in cell signaling processes that mediate development, differentiation, integration, and connectivity of neural circuits.

The refinement of strategies to precisely control neural activity *in vivo*, as well as a deeper understanding of the molecular mechanisms linking retinal waves to various developmental processes will continue to provide insights onto the various roles of spontaneous activity patterns in circuit development.

References

Ackman, J. B., Burbridge, T. J., and Crair, M. C. (2012). Retinal waves coordinate patterned activity throughout the developing visual system. *Nature* 490, 219–225. doi: 10.1038/nature11529

Ackman, J. B., and Crair, M. C. (2014). Role of emergent neural activity in visual map development. *Curr. Opin. Neurobiol.* 24, 166–175. doi: 10.1016/j.conb.2013.11.011

Assali, A., Gaspar, P., and Rebsam, A. (2014). Activity dependent mechanisms of visual map formation–from retinal waves to molecular regulators. *Semin. Cell Dev. Biol.* 35, 136–146. doi: 10.1016/j.semcdb.2014.08.008

Bansal, A., Singer, J. H., Hwang, B. J., Xu, W., Beaudet, A., and Feller, M. B. (2000). Mice lacking specific nicotinic acetylcholine receptor subunits exhibit dramatically altered spontaneous activity patterns and reveal a limited role for retinal waves in forming ON and OFF circuits in the inner retina. *J. Neurosci.* 20, 7672–7681.

Blankenship, A. G., and Feller, M. B. (2010). Mechanisms underlying spontaneous patterned activity in developing neural circuits. *Nat. Rev. Neurosci.* 11, 18–29. doi: 10.1038/nrn2759

Bonetti, C., and Surace, E. M. (2010). Mouse embryonic retina delivers information controlling cortical neurogenesis. *PLoS One* 5:e15211. doi: 10.1371/journal.pone.0015211

Burbridge, T. J., Xu, H.-P., Ackman, J. B., Ge, X., Zhang, Y., Ye, M.-J., et al. (2014). Visual circuit development requires patterned activity mediated by retinal acetylcholine receptors.*Neuron* 84, 1049–1064. doi: 10.1016/j.neuron.2014.10.051

Butts, D. A., Kanold, P. O., and Shatz, C. J. (2007). A burst-based "Hebbian" learning rule at retinogeniculate synapses links retinal waves to activity-dependent refinement. *PLoS Biol.*5:e61. doi: 10.1371/journal.pbio.0050061

Cang, J., Wang, L., Stryker, M. P., and Feldheim, D. A. (2008). Roles of ephrin-as and structured activity in the development of functional maps in the superior colliculus. *J. Neurosci.* 28, 11015–11023. doi: 10.1523/JNEUROSCI.2478-08.2008

Chalupa, L. M. (2009). Retinal waves are unlikely to instruct the formation of eye-specific retinogeniculate projections. *Neural Dev.* 4:25. doi: 10.1186/1749-8104-4-25

Colonnese, M. T., and Khazipov, R. (2010). "Slow activity transients" in infant rat visual cortex: a spreading synchronous oscillation patterned by retinal waves. *J. Neurosci.* 30, 4325–4337. doi: 10.1523/JNEUROSCI.4995-09.2010

Crair, M. C. (1999). Neuronal activity during development: permissive or instructive? *Curr. Opin. Neurobiol.* 9, 88–93. doi: 10.1016/s0959-4388(99)80011-7

Dähne, S., Wilbert, N., and Wiskott, L. (2014). Slow feature analysis on retinal waves leads to V1 complex cells. *PLoS Comput. Biol.* 10:e1003564. doi: 10.1371/journal.pcbi.1003564

Davis, Z. W., Chapman, B., and Cheng, H.-J. (2015). Increasing spontaneous retinal activity before eye opening accelerates the development of geniculate receptive fields. *J. Neurosci.* 35, 14612–14623. doi: 10.1523/JNEUROSCI.1365-15.2015

Eglen, S. J., Demas, J., and Wong, R. O. L. (2003). Mapping by waves. Patterned spontaneous activity regulates retinotopic map refinement. *Neuron* 40, 1053–1055. doi: 10.1016/S0896-6273(03)00808-0

Failor, S., Chapman, B., and Cheng, H.-J. (2015). Retinal waves regulate afferent terminal targeting in the early visual pathway. *Proc. Natl. Acad. Sci. U S A* 112, E2957–E2966. doi: 10.1073/pnas.1506458112

Feller, M. B. (2009). Retinal waves are likely to instruct the formation of eye-specific retinogeniculate projections. *Neural Dev.* 4:24. doi: 10.1186/1749-8104-4-24

Feller, M. B. M., Wellis, D. P. D., Stellwagen, D. D., Werblin, F. S. F., and Shatz, C. J. C. (1996). Requirement for cholinergic synaptic transmission in the propagation of spontaneous retinal waves. *Science* 272, 1182–1187. doi: 10.1126/science.272.5265.1182

Firl, A., Sack, G. S., Newman, Z. L., Tani, H., and Feller, M. B. (2013). Extrasynaptic glutamate and inhibitory neurotransmission modulate ganglion cell participation during glutamatergic retinal waves. *J. Neurophysiol.* 109, 1969–1978. doi: 10.1152/jn.00039.2013

Golding, B., Pouchelon, G., Bellone, C., Murthy, S., Di Nardo, A. A., Govindan, S., et al. (2014). Retinal input directs the recruitment of inhibitory interneurons into thalamic visual circuits.*Neuron* 81, 1057–1069. doi: 10.1016/j.neuron.2014.01.032

Hagihara, K. M., Murakami, T., Yoshida, T., Tagawa, Y., and Ohki, K. (2015). Neuronal activity is not required for the initial formation and maturation of visual selectivity. *Nat. Neurosci.* 18, 1780–1788. doi: 10.1038/nn.4155

Huberman, A. D., Feller, M. B., and Chapman, B. (2008). Mechanisms underlying development of visual maps and receptive fields. *Annu. Rev. Neurosci.* 31, 479–509. doi: 10.1146/annurev.neuro.31.060407.125533

Huberman, A. D., Wang, G.-Y., Liets, L. C., Collins, O. A., Chapman, B., and Chalupa, L. M. (2003). Eye-specific retinogeniculate segregation independent of normal neuronal activity.*Science* 300, 994–998. doi: 10.1126/science.1080694

Kerschensteiner, D. (2013). Spontaneous network activity and synaptic development.*Neuroscientist* 20, 272–290. doi: 10.1177/1073858413510044

Kerschensteiner, D., and Wong, R. O. L. (2008). A precisely timed asynchronous pattern of ON and OFF retinal ganglion cell activity during propagation of retinal waves. *Neuron* 58, 851–858. doi: 10.1016/j.neuron.2008.04.025

Kirkby, L. A., and Feller, M. B. (2013). Intrinsically photosensitive ganglion cells contribute to plasticity in retinal wave circuits. *Proc. Natl. Acad. Sci. U S A* 110, 12090–12095. doi: 10.1073/pnas.1222150110

Maccione, A., Hennig, M. H., Gandolfo, M., Muthmann, O., van Coppenhagen, J., Eglen, S. J., et al. (2014). Following the ontogeny of retinal waves: pan-retinal recordings of population dynamics in the neonatal mouse. *J. Physiol.* 592, 1545–1563. doi: 10.1113/jphysiol.2013.262840

McLaughlin, T., Torborg, C. L., Feller, M. B., and O'Leary, D. D. M. (2003). Retinotopic map refinement requires spontaneous retinal waves during a brief critical period of development.*Neuron* 40, 1147–1160. doi: 10.1016/s0896-6273(03)00790-6

Owens, M. T., Feldheim, D. A., Stryker, M. P., and Triplett, J. W. (2015). Stochastic interaction between neural activity and molecular cues in the formation of topographic maps. *Neuron* 87, 1261–1273. doi: 10.1016/j.neuron.2015.08.030

Pfeiffenberger, C., Yamada, J., and Feldheim, D. A. (2006). Ephrin-As and patterned retinal activity act together in the development of topographic maps in the primary visual system. *J. Neurosci.* 26, 12873–12884. doi: 10.1523/JNEUROSCI.3595-06.2006

Seabrook, T. A., El-Danaf, R. N., Krahe, T. E., Fox, M. A., and Guido, W. (2013). Retinal input regulates the timing of corticogeniculate innervation. *J. Neurosci.* 33, 10085–10097. doi: 10.1523/JNEUROSCI.5271-12.2013

Speer, C. M., Sun, C., Liets, L. C., Stafford, B. K., Chapman, B., and Cheng, H.-J. (2014). Eye-specific retinogeniculate segregation proceeds normally following disruption of patterned spontaneous retinal activity. *Neural Dev.* 9:25. doi: 10.1186/1749-8104-9-25

Stafford, B. K., Sher, A., Litke, A. M., and Feldheim, D. A. (2009). Spatial-temporal patterns of retinal waves underlying activity-dependent refinement of retinofugal projections. *Neuron* 64, 200–212. doi: 10.1016/j.neuron.2009.09.021

Stellwagen, D., and Shatz, C. J. (2002). An instructive role for retinal waves in the development of retinogeniculate connectivity. *Neuron* 33, 357–367. doi: 10.1016/s0896-6273(02)00577-9

Stellwagen, D., Shatz, C. J., and Feller, M. B. (1999). Dynamics of retinal waves are controlled by cyclic AMP. *Neuron* 24, 673–685. doi: 10.1016/s0896-6273(00)81121-6

Sun, C., Warland, D. K., Ballesteros, J. M., van der List, D., and Chalupa, L. M. (2008). Retinal waves in mice lacking the β2 subunit of the nicotinic acetylcholine receptor. *Proc. Natl. Acad. Sci. U S A* 105, 13638–13643. doi: 10.1073/pnas.0807178105

Wong, R. O. L. (1999). Retinal waves and visual system development. *Annu. Rev. Neurosci.* 22, 29–47. doi: 10.1146/annurev.neuro.22.1.29

Wong, W. T., Myhr, K. L., Miller, E. D., and Wong, R. O. (2000). Developmental changes in the neurotransmitter regulation of correlated spontaneous retinal activity. *J. Neurosci.* 20, 351–360.

Xu, H.-P., Burbridge, T. J., Chen, M.-G., Ge, X., Zhang, Y., Zhou, Z. J., et al. (2015). Spatial pattern of spontaneous retinal waves instructs retinotopic map refinement more than activity frequency. *Dev. Neurobiol.* 75, 621–640. doi: 10.1002/dneu.22288

Xu, H.-P., Furman, M., Mineur, Y. S., Chen, H., King, S. L., Zenisek, D., et al. (2011). An instructive role for patterned spontaneous retinal activity in mouse visual map development.*Neuron* 70, 1115–1127. doi: 10.1016/j.neuron.2011.04.028

Zhang, J., Ackman, J. B., Xu, H.-P., and Crair, M. C. (2011). Visual map development depends on the temporal pattern of binocular activity in mice. *Nat. Neurosci.* 15, 298–307. doi: 10.1038/nn.3007

Figure 1: Spontaneous retinal waves mediate eye-specific segregation and retinotopic refinement of retinofugal projections.
The axons of retinal ganglion cells (RGCs) target the dorsal lateral geniculate nucleus (dLGN) of the thalamus and the superior colliculus (SC). RGC projections from opposite eyes are segregated into ipsilateral and contralateral regions (black/gray oppositions). RGC projections from each retina are retinotopically organized (colored regions). Note that for simplicity we have depicted retinotopic maps only for one eye. Retinotopic maps and eye-specific segregations form for both eyes.

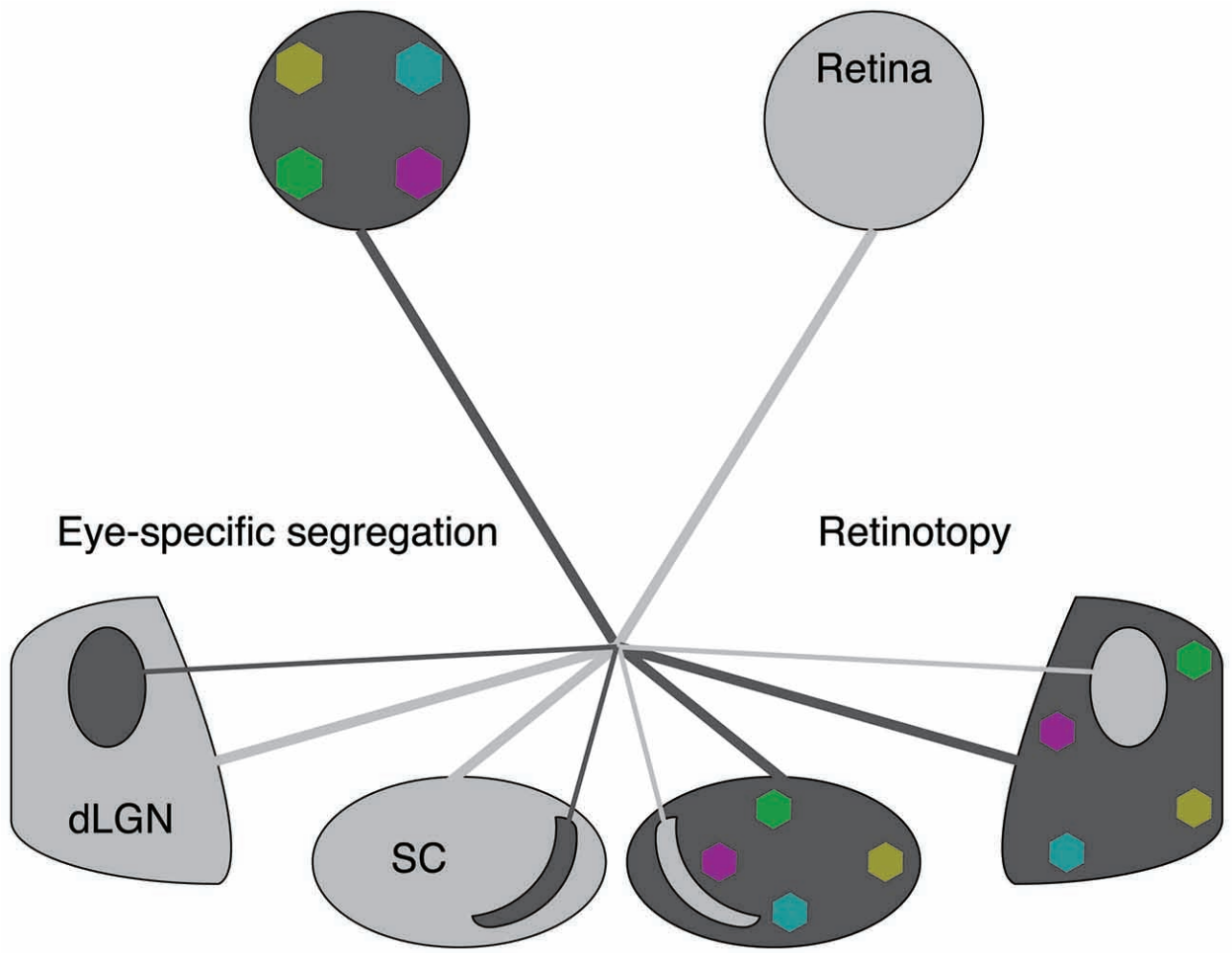
Retina
Eye-specific segregation
Retinotopy
dLGN
SC

Figure 2: Distinct spatiotemporal patterns of retinal waves instruct different features of retinofugal projections in mice.
(A–D). Top: schematic of retinal wave firing patterns. Dots are representative of RGCs with larger dots indicating elevated firing rates during a single retinal wave. Bottom: schematic of retinogeniculate wiring using same code as Figure 1—colored hexagons represent retinotopy while gray/black regions represent eye-specific segregation. (A) Under normal conditions, RGCs exhibit high local correlations while activity of the two retinas is minimally correlated. This pattern of activity supports both eye-specific segregation and retinotopic maps in both the dLGN and SC. (B) High correlations between retinal waves of opposite retinas induced by optogenetic stimulation is detrimental to eye-specific segregation while retinotopic maps are unaffected (Zhang et al., 2011). (C) Disruption of local correlations either by an increase in uncorrelated firing or by abnormally elevated correlations between distant RGCs (global correlations), such as that observed in β2KO and Retβ2-cKO mice, is detrimental to retinotopic map formation. Local correlations are sufficient for normal retinotopic maps in Retβ2-cKO, Rxβ2-cKO and β2(TG) (Xu et al., 2011, 2015; Burbridge et al., 2014). (D) High global correlations paired with high inter-retina correlations such as that observed in the β2KO mouse, is detrimental to both eye-specific segregation and retinotopic maps (Xu et al., 2011; Burbridge et al., 2014).

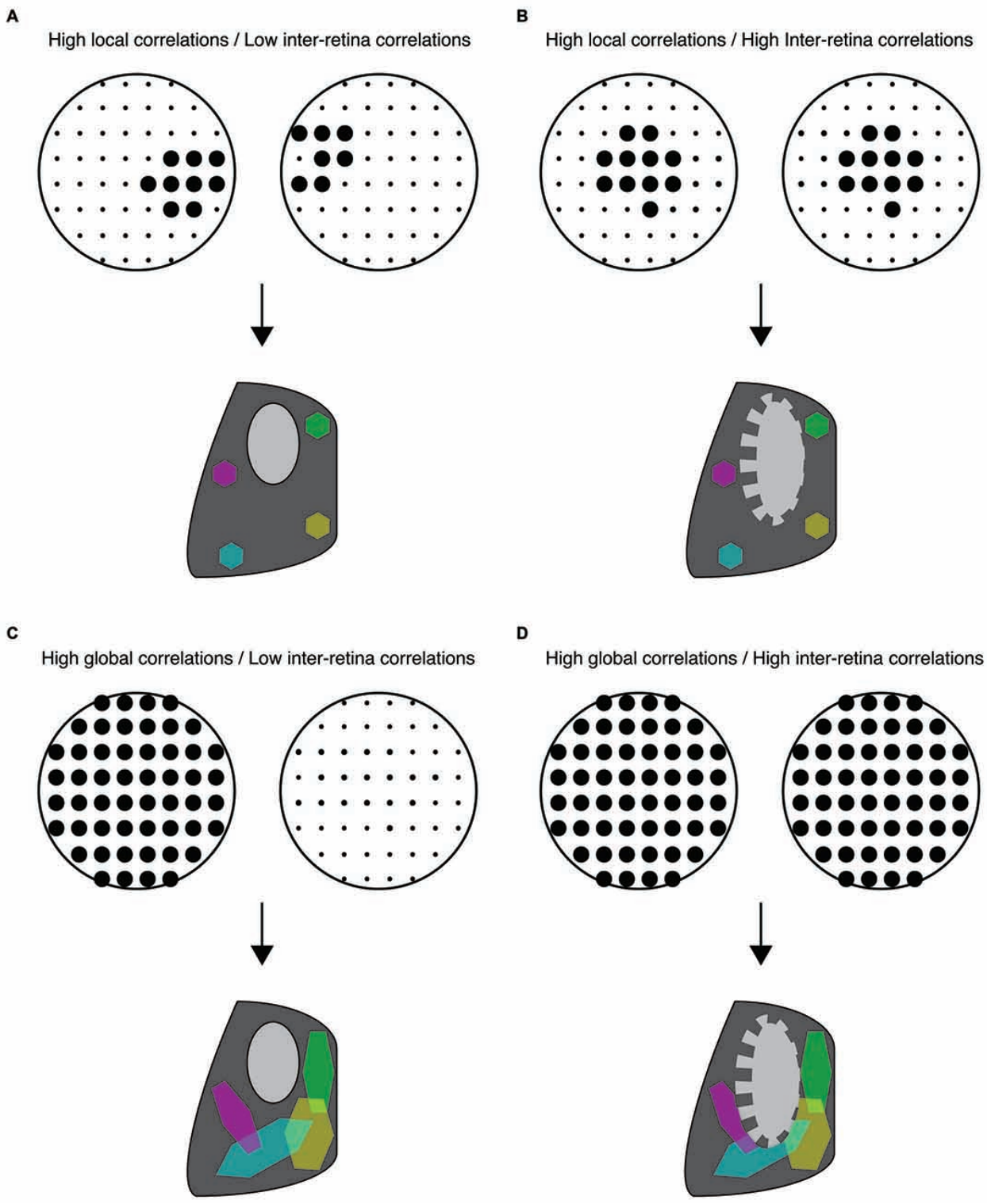
A
High local correlations / Low inter-retina correlations
B
High local correlations / High Inter-retina correlations
C
High global correlations / Low inter-retina correlations
D
High global correlations / High inter-retina correlations

II. A role for TREK1 in generating the slow afterhyperpolarization in developing starburst amacrine cells

Abstract

Slow afterhyperpolarizations (sAHPs) play an important role in establishing the firing pattern of neurons that in turn influence network activity. sAHPs are mediated by calcium-activated potassium channels. However, the molecular identity of these channels and the mechanism linking calcium entry to their activation are still unknown. Here we present several lines of evidence suggesting that the sAHPs in developing starburst amacrine cells (SACs) are mediated by two-pore potassium channels. First, we use whole cell and perforated patch voltage clamp recordings to characterize the sAHP conductance under different pharmacological conditions. We find that this conductance was calcium dependent, reversed at E_K, blocked by barium, insensitive to apamin and TEA, and activated by arachidonic acid. In addition, pharmacological inhibition of calcium-activated phosphodiesterase reduced the sAHP. Second, we performed gene profiling on isolated SACs and found that they showed strong preferential expression of the two-pore channel gene*kcnk2* that encodes TREK1. Third, we demonstrated that TREK1 knockout animals exhibited an altered frequency of retinal waves, a frequency that is set by the sAHPs in SACs. With these results, we propose a model in which depolarization-induced decreases in cAMP lead to disinhibition of the two-pore potassium channels and in which the kinetics of this biochemical pathway dictate the slow activation and deactivation of the sAHP conductance. Our model offers a novel pathway for the activation of a conductance that is physiologically important.

Introduction

Several types of neurons throughout the central and peripheral nervous system exhibit prolonged hyperpolarizations following bursts of action potentials (Hirst et al. 1985; Lancaster and Nicoll 1987; Schwindt et al. 1988). These slow afterhyperpolarizations (sAHPs) underlie oscillatory burst firing in cholinergic striatal neurons and gonadotropin-releasing hormone neurons (Goldberg et al. 2009; Lee et al. 2010), and they give rise to spike frequency adaptation in the principal cells of the cortex, hippocampus, and amygdala (Faber and Sah 2002; Lancaster and Adams 1986; Lorenzon and Foehring 1992). During development, retinal interneurons called starburst amacrine cells (SACs) exhibit sAHPs (Ford et al. 2012; Zheng et al. 2006). These sAHPs play an important functional role within the developing retina by setting the frequency of spontaneous retinal waves, which play an instructive role in the eye-specific and retinotopic organization of retinofugal projections (Ford et al. 2012; Godfrey and Swindale 2007; Hennig et al. 2009; Zheng et al. 2006).

Despite the prevalence and functional importance of sAHPs, the channels that give rise to them are unknown. It is generally accepted that sAHPs are mediated by potassium channels that are activated upon calcium influx through a variety of voltage-gated calcium channels (Sah and Faber 2002). No specific antagonists of sAHPs have been found, but several intracellular signaling pathways modulate the sAHP, including PKA, PKC, and PIP2 pathways (Lancaster et al. 2006; Lancaster and Nicoll 1987; Sah and Isaacson 1995; Villalobos et al. 2011; Vogalis et al. 2002). The slow kinetics of the sAHP have led to speculation that sAHP channels are not directly activated by calcium entry, but rather are indirectly opened by a signaling cascade, possibly involving phosphorylation of the channel (Abel et al. 2004). Implicated in this activation are the calcium-activated phosphatase calcineurin (Vogalis et al. 2004) and the calcium sensors hippocalcin (Tzingounis et al. 2007) and neurocalcin (Villalobos and Andrade 2010). However, the pathway leading from calcium entry to the channel's activation is still unknown.

Two-pore potassium (K2P) channels produce the hyperpolarized resting membrane potential in most neurons (Enyedi and Czirjak 2010), and they exhibit properties that are similar to those of channels underlying sAHPs. K2P channels are insensitive to most potassium channel antagonists but are modulated by second messenger cascades (Mathie 2007). Several K2P channel family members can be distinguished by their current rectification, modulation by protein kinases, and activation by heat, stretch, and lipids (Enyedi and Czirjak 2010; Lesage and Lazdunski 2000). While no family member is directly activated by calcium, their channel openings are gated by activation of calcium-dependent signaling cascades (Czirjak et al. 2004).

Here we combine perforated patch recordings with pharmacology in order to implicate a specific K2P channel, TREK1, in the generation of sAHPs in developing SACs. Second, we perform calcium imaging to investigate how modulating sAHP conductance affects circuit function. Last, we use multielectrode array recordings from mice lacking TREK1 to implicate this channel in the normal patterning of retinal waves.

Methods

All animal procedures were approved by the University of California, Berkeley, and the Baylor School of Medicine, and they conformed to the National Institutes of Health *Guide for the Care and Use of Laboratory Animals*, the Public Health Service Policy, and the Society for Neuroscience Policy on the Use of Animals in Neuroscience Research.

Animals. All experiments were performed on acutely isolated mouse retinas. Male and female C57Bl/6 mice obtained from Harlan were used for all wild-type (WT) recordings. mGluR2-GFP mice contained a transgene insertion of interleukin-2 receptor-fused GFP under control of the mGluR2 promoter (Watanabe et al. 1998). ChAT-Cre/TdTom mice were generated by crossing a mouse in which an IRES-Cre recombinase was knocked in downstream of the endogenous choline acetyl transferase gene (Ivanova et al. 2010) with a separate tdTomato driver line [B6.129S6-ChAT$^{tm1(cre)lowl}$/J × B6.129S6-Gt(ROSA)26Sor$^{tm9(CAG-tdTomato)Hze}$/J, Jackson Labs]. TREK1−/− mice (Namiranian et al. 2010) were used for assessing the role of TREK1 (gene name KCNK2) in retinal waves. Age-matched non-littermate C57BL/6 WT mice were used as controls. Genotypes were determined by genomic PCR using primer sequences described previously (Namiranian et al. 2010).

Whole mount retinal preparation. P4-P7 mice were anesthetized with isoflurane and decapitated. Retinas were isolated in cold artificial cerebrospinal fluid (ACSF) (in mM: 119 NaCl, 26.2 $NaHCO_3$, 11 glucose, 2.5 KCl, 1 K_2HPO_4, 2.5 $CaCl_2$, 1.3 $MgCl_2$) and mounted ganglion cell side up on filter paper. Retinas were incubated at room temperature in oxygenated ACSF until transfer to the recording chamber, where they were continuously superfused with oxygenated ACSF at 30–34°C.

Electrophysiology. Perforated patch and whole cell recordings were performed on whole mount retinas from mice aged P4-P7. The inner limiting membrane was removed using a glass recording pipette, and SACs were identified using fluorescence and targeted using a Sutter micromanipulator. Voltage clamp recordings were sampled at 2.5 kHz and filtered at 1 kHz. Current clamp recordings were sampled at 5 kHz and filtered at 2 kHz. Analysis was performed using custom MATLAB (Mathworks) scripts. All reported voltages were corrected for liquid junction potential. Statistical significance was accessed using paired *t*-tests.

Perforated patch voltage and current clamp recordings were performed in the presence of DHβE (4 μM) and gabazine (5 μM) to block nAChR and GABA-A receptor-mediated synaptic conductances, and in the presence of tolbutamide (100 μM) to block an ATP-sensitive potassium conductance that develops during prolonged recordings (see Fig. 2). During recordings of conductance (Fig. 1*E*) and current-voltage relationships (Fig. 1, *C* and *D*), TTX (200 nM), 4-aminopyridine (4-AP) (1 mM), tetraethylammonium chloride (TEA) (1 mM), and cesium chloride (2 mM) were included in the bath solution to block voltage-activated conductances. A gluconate-based perforated patch internal solution (in mM: 122 K gluconate, 20 HEPES, 0.5 EGTA, 2 NaCl, pH 7.2, liquid junction potential: 14 mV) was frontfilled into electrodes and then backfilled with internal solution containing 750 μg/ml amphotericin B made fresh hourly. Seals were formed and then access resistance was monitored continuously. Recordings were performed when access resistance was stable and less than 5% of the input resistance of the cell (typically,

R_a = 30–80 MΩ, R_{in} = 1–2 GΩ). While access resistance prevented efficient voltage clamp of voltage-gated calcium and potassium currents during depolarizing steps, the small current (~5 pA) underlying the sAHP is unlikely to induce errors in voltage clamp during measurement of the reversal potential. Furthermore, maximum amplitudes and kinetics of the slow AHP were not correlated with the access resistance.

Whole cell recordings from SACs were made using potassium phosphate based internal solution (in mM: 110 KH_2PO_4, 6 $MgCl_2$, 1 EGTA, 4 adenosine 5′-triphosphate magnesium salt, 0.3 guanosine 5′-triphosphate trisodium salt, 10 HEPES, and 10 phosphocreatine disodium salt, pH 7.2, liquid junction potential: 14 mV).

Calcium imaging. Retinas from mice aged postnatal day (P)2-P6 were bulk loaded with the calcium indicator Oregon Green Bapta-1 AM (OGB-1 AM) using the multicell bolus loading technique (Blankenship et al. 2009; Stosiek et al. 2003). Epifluorescence imaging and analysis were performed as described earlier (Blankenship et al. 2009). Significance was assessed using paired *t*-tests.

Multi-electrode array recordings. TREK1−/− and WT mice were dissected and placed ganglion cell side down onto a 60-electrode array (Multi-Channel Systems). The array electrodes were 10 μm in diameter and were arranged in an 8 × 8 grid (minus 4 corners) with 100-μm interelectrode spacing. The retina was held in place on the array with a weighted piece of dialysis membrane and was superfused continuously with oxygenated ACSF. The voltage trace on each electrode was sampled at 20 kHz and stored for offline analysis. The traces were then pass filtered between 120 and 2,000 Hz. Spikes that crossed a threshold of three times the root mean square of the noise on each electrode were sorted according to the two principal components of their voltage waveforms. A valley seeking algorithm was then used to sort spike clusters into individual units. To verify that each unit identified by this algorithm corresponded to a single cell, we inspected units manually. Furthermore, units that lacked a refractory period in their autocorrelation function were considered contaminated by other neurons and were excluded from the analysis. The mean spike rate, r, was calculated by dividing the total number of spikes for each unit by the recording duration. Units whose mean spike rate was <1/10 of the mean firing rate of all cells were excluded from additional analysis to reduce contamination from low spiking cells. After this cut, 20–45 units remained. Using the sorted spikes, waves were defined as events where the average firing rate increased over a selected threshold (values varied from 0.3 to 2.1 SD above the mean) and were separated by more than 10 s. The threshold was adjusted for each retina such that the number of defined waves was consistent with the number of waves identified by eye in the raster plots. Interwave intervals were pooled, and TREK−/− and WT waves were compared using a two-tailed *t*-test with a 99% confidence interval.

Microarray analysis. A database of gene expression in 13 retinal neuron subtypes was generated using Affymetrix Mouse Genome 430 2.0 microarrays as described (Kay et al. 2011, 2012). The data was collected at P6, a time of strong retinal wave activity. To determine the expression profile of K2P family channels, we began by identifying Affymetrix probesets corresponding to each of the 13 genes in the mouse Kcnk gene family, which encode the K2P channels (Talley et al. 2003). This was done by searching the Affymetrix NetAffx online database and curating probesets by hand, using the Ensembl mouse genome viewer. To ensure completeness, we

identified all probesets present on the 430 2.0 arrays that represent Kcnk family genes; some genes were represented on the array as multiple independent sequences, whereas others were represented by only one sequence. Next we queried our microarray database to determine the expression values of each of the Kcnk gene sequences across the 13 cell types. Probesets that were not expressed in any of the cell types were excluded from further analysis, which left 16 probesets (corresponding to the 13 Kcnk genes). Finally, we used a hierarchical clustering algorithm (dChip microarray data analysis software) to generate a heat map showing expression of these 16 sequences (see Fig. 3*B*). Sequences that have similar expression patterns are clustered together. Because preliminary analysis suggested that Kcnk2, which encodes TREK1, was specifically expressed in SACs, we included in the clustering analysis two known SAC-specific genes, encoding the vesicular acetylcholine transporter and choline acetyltransferase.

The Affymetrix probesets used for clustering (and the genes to which they correspond) were: 1455896_a_at (Kcnk1); 1448690_at (Kcnk1); 1449158_at (Kcnk2); 1445929_at (Kcnk2); 1425341_at (Kcnk3); 1421419_at (Kcnk4); 1421852_at (Kcnk5); 1435342_at (Kcnk6); 1425437_a_at (Kcnk7); 1445309_at (Kcnk9); 1431613_a_at (Kcnk10); 1441280_at (Kcnk12); 1447645_x_at (Kcnk13); 1424125_at (Kcnk13); 1447972_at (Kcnk15); 1429913_at (Kcnk16); 1440070_at (Chat, encoding choline acetyltransferase); 1422203_at (Slc18a3, encoding vesicular acetylcholine transporter). Cell type abbreviations in Fig. 3*B* are described in Kay et al. 2012.

Results

Slow AHPs in SACs exhibit properties similar to those of K2P channels

Following spontaneous depolarization during waves or evoked depolarization via current injection, SACs in developing mouse retina exhibit sAHPs (Fig. 1*A*) (Ford et al. 2012; Zheng et al. 2006). To determine the current underlying these sAHPs, we performed perforated patch voltage clamp recordings of SACs. We blocked synaptic input with cholinergic and GABAergic antagonists (4 μM dihydro-β-erthryoidine + 5 μM gabazine) to isolate the cell-intrinsic conductances. At this stage of development, glutamatergic inputs are immature and do not shape spontaneous activity patterns (Bansal et al. 2000). We found that, as previously described, depolarizing steps (of 500-ms duration from −64 mV to −14 mV) evoked a slow outward current at −64 mV (Fig. 1*B*) (Ford et al. 2012). This current has a slow rise and decay similar to sAHPs measured in current clamp (Fig. 1*B*). Thus, henceforth we refer to this current as I_{sAHP}.

Several lines of evidence indicate that I_{sAHP} is mediated by potassium channels and that it requires calcium entry for activation. First, channel activation was associated with an increase in conductance (Fig. 1*E*, $n = 3$). This implies the opening of channels rather than the activation of a transporter, a potential alternative source of the slow outward current (Pulver and Griffith 2010). Second, I_{sAHP} reversed at the reversal potential for potassium (E_K, Fig. 1*C*). At physiological external potassium concentration (4.5 mM), the current exhibited outward rectification. Third, as external potassium increased, the reversal potential for I_{sAHP} shifted, consistent with the Nernst equation prediction for a potassium conductance (Fig. 1*D*). Fourth,I_{sAHP} was reversibly blocked when calcium was removed from the bath solution (Fig. 1*F*, $n = 4$). Thus, our data indicate that I_{sAHP} is mediated by a calcium-activated potassium channel.

To further characterize this channel, we conducted pharmacological experiments. Since calcium-activated potassium channels include the BK and SK families (Sah 1996), we investigated their involvement. BK channels mediate rapid repolarization during action potentials, while SK channels underlie the medium length afterhyperpolarization that follows individual action potentials. We blocked BK channels (Yellen 1984), as well as other voltage-gated channels, with 1 mM TEA and found that the amplitude of $I_{sAHP}$was unaffected (Fig. 1*F*, $n = 5$). We blocked SK channels with its specific antagonist, apamin (Sah and Faber 2002), and found that the amplitude ofI_{sAHP} was again unaffected (Fig. 1*F*, $n = 5$). Hence, neither BK nor SK channels contribute to the generation of I_{sAHP}.

We next tested the involvement of ATP-dependent potassium channels (K_{atp}). These channels are activated by depolarization, contribute to a slow afterhyperpolarization in hippocampal pyramidal cells (Tanner et al. 2011), and are thought to be activated by a decrease in the cell's ATP levels. We found these channels in the SACs. After gaining whole cell access to a SAC, we observed a rapidly developing conductance that produced a dramatic drop in input resistance (Fig. 2*A*). This conductance reversed at E_K (data not shown), indicating the opening of potassium channels. Subsequent depolarizing steps activated a transient outward tail current (Fig. 2, *A* and *B*). Both this transient tail current and the whole cell-activated conductance were blocked by the K_{atp} channel antagonist tolbutamide (100 μM; R_{in} for control = 0.33 ± 0.15 GΩ and for tolbutamide = 1.74 ± 0.22 GΩ; $P = 0.0004$, $n = 5$, Fig. 2*B*), indicating that these currents

are mediated by K_{atp} channels. To determine if these channels mediate I_{sAHP}, we blocked with tolbutamide while using the perforated patch configuration and found that I_{sAHP} did not change (Fig. 2*C*, $n = 5$). Thus, K_{atp} channels in SACs are activated by the reduction of intracellular ATP caused by intracellular dialysis during whole cell recordings. However, when the intracellular milieu is left intact, these channels do not contribute to the sAHPs.

To determine if K2P channels mediate I_{sAHP}, we first approached the family as a whole. The K2P family consists of 13 members, including the TWIK, TASK, TREK, TALK, THIK, and TRESK subfamilies (Talley et al. 2003). These subfamilies are insensitive to several potassium channel antagonists, including TEA, 4-AP, and cesium (Lesage 2003). Consistent with this, a combination of 1 mM TEA, 1 mM 4-AP, and 2 mM cesium did not block theI_{sAHP} in SACs ($n = 4$, data not shown, see METHODS). However, I_{sAHP} was blocked by barium (2 mM, $n = 7$, Fig. 3*A*), a blocker of the K2P channel subfamilies TASK, TREK, TWIK, and TRESK (Deng et al. 2009). These data, along with our finding that I_{sAHP} is outwardly rectifying (Fig. 1*C*), suggest thatI_{sAHP} in SACs is mediated by one of the K2P subfamilies, which include TREK, TASK, and TRESK channels.

To distinguish between these subfamilies, we first conducted a microarray analysis of mRNA isolated from SACs (Kay et al. 2011, 2012). We found that*kcnk2*, the mRNA that encodes the K2P channel TREK1, is highly expressed in SACs during the first postnatal week (Fig. 3*B*). In fact, within the subset of cell types analyzed, it is specifically expressed only in SACs. Moreover, it is expressed with a degree of specificity that is similar to that seen for other markers of SACs, such as choline acetyl transferase and Megf10 (Kay et al. 2012). These results suggest that TREK1 channels likely mediate the slow potassium conductance underlying sAHPs.

We next conducted pharmacological experiments to ask whether other K2P subfamilies might also contribute to the sAHP. TRESK channels as well as TASK-3 and TASK-9 channels are inhibited by extract derived from sanshool chili peppers (Bautista et al. 2008). Bath application of 0.02% sanshool extract did not block I_{sAHP} or increase the input resistance (Fig. 3*A*, $n = 4$), indicating that SACs do not express these K2P channel types. TREK and TRAAK channels exhibit potentiated currents with arachidonic acid (AA) (Lesage and Lazdunski 2000). Bath application of 10 μM AA led to a significant increase in the holding current at −60 mV and a corresponding decrease in the input resistance (in control, -1.0 ± 2.5 pA, 1.52 ± 0.24 GΩ; in AA, 10.0 ± 3.6 pA, 1.12 ± 0.23 GΩ; $P = 0.0059$ for holding current at −64 mV,$P = 0.0117$ for input resistance, $n = 7$). Moreover, I_{sAHP} was increased in amplitude (Fig. 3A, $n = 7$). Thus, our results support the hypothesis that I_{sAHP}in SACs is mediated by TREK, but not TASK or TRESK channels.

However, I_{sAHP} requires calcium influx for activation, while TREK channels are not activated by changes in intracellular calcium (Fink et al. 1996). How might these channels be activated to generate the sAHP in SACs? Previously, we along with others showed that I_{sAHP} is inhibited by the elevation of cAMP with forskolin (Ford et al. 2012; Zheng et al. 2006). Recently, TREK1 was shown to be activated by decreases in cAMP following the activation of metabotropic GABA receptors (Sandoz et al. 2012). Thus, we hypothesize that calcium influx into SACs activates calcium-activated phosphodiesterases (PDEs) leading to a decrease in cAMP level that then activates the TREK1 channels. We tested if PDE-1C, the calcium-activated

phosphodiesterase that is expressed in SACs (Santone et al. 2006), plays a role in generating I_{sAHP}. We applied 8-methoxymethyl-3-isobutyl-1-methyl xanthine (MMPX; 100 μM), a specific PDE-1C inhibitor, and found that it inhibited I_{sAHP} (Fig. 3*A*, $n = 8$). Although at this concentration, MMPX may inhibit multiple PDEs, it exhibited specificity in pancreatic β-cells (Tian et al. 2012). Also, in a previous study based on imaging of PKA activity, we found that high concentrations of MMPX did not lead to a tonic increase in basal cAMP levels in retinal neurons as observed in the presence of the broad spectrum inhibitor IBMX (Dunn et al. 2009). In addition, these data are consistent with previous studies showing forskolin, an adenylate cyclase activator, decreases I_{sAHP} (Ford et al. 2012;Zheng et al. 2006). Together, our findings indicate that I_{sAHP} may be generated by activation of TREK channels via a calcium-dependent decrease in cAMP.

Changing the kinetics of sAHPs alters the frequency of retinal waves

To determine the effect of sAHPs on network function in the developing retina, we used calcium imaging to investigate how changing sAHPs altered retinal waves (Ford et al. 2012). The timing of spontaneous retinal waves is critical for normal visual system development. We know that SACs control wave timing, but the mechanism is unclear. The sAHPs are well positioned to regulate the frequency of spontaneous retinal waves by generating a refractory period following the depolarization caused by a wave. If sAHPs really do set wave frequency, then blocking them should increase the frequency of waves. To test this hypothesis, we manipulated sAHPs via the cAMP-PDE pathway described above. We used MMPX to block calcium-dependent PDE activity, increasing cAMP levels and thereby inhibiting sAHPs. As predicted, this increased the frequency of waves, as we have previously shown using the broad spectrum PDE blocker IBMX and direct elevation of cAMP levels using forskolin (Ford et al. 2012) (Fig. 4, *A* and *B*, $P = 0.001$). By contrast, potassium channel antagonists, cesium and tolbutamide, that had no effect on I_{sAHP}, also failed to influence the interwave interval (Fig. 4*B*, $P = 0.42$ and $P = 0.29$ for cesium and tolbutamide, respectively). These results support the notion that sAHP currents in SACs, and the calcium-regulated cAMP pathway that regulates them, are critical for controlling the timing of retinal waves. Thus, sAHPs appear to play an important role in the control of circuit function in the retina.

TREK1 knockout mice exhibit altered retinal waves

Our molecular data suggest that the key channel mediating sAHPs in SACs is TREK1. If so, then loss of TREK1 function should also increase the frequency of waves. We were not able to import mice to use calcium imaging, so to investigate the functional role of TREK1 in retinal waves, we conducted multi-electrode array (MEA) recordings in P1-P3 WT and TREK1−/− mice (Namiranian et al. 2010). MEA recordings and calcium imaging led to the same results in terms of assaying the frequency of waves (Torborg and Feller 2005). Compared with WT animals, TREK1−/− mice exhibited interwave intervals that were approximately one-half the length (WT = 85.23 ± 15.96 s, TREK1−/− = 45.41 ± 15.51 s, *t*-test $P < 0.001$, Fig. 5), similar in scale to the effect of inhibiting the sAHP with MMPX (Fig. 4). Thus, TREK1 plays an important role in setting the pace for retinal waves. These data are consistent with the idea that TREK1 is a major contributor to the sAHP in SACs.

Discussion

We have demonstrated that sAHPs in developing SACs are mediated by a potassium channel that shows pharmacological and rectification properties consistent with the K2P channel, TREK1. TREK1 is highly and specifically expressed in SACs. The channel underlying sAHPs is inhibited by tonically elevating cAMP and is blocked by preventing the calcium-dependent degradation of cAMP by PDEs, consistent with TREK1. In addition, we have shown that altering sAHPs pharmacologically and in mice lacking TREK1 changes the frequency of retinal waves, indicating a functional role for TREK1 in circuit function. Below, we discuss the role of the K2P channel TREK1 in generating I_{sAHP}, and we propose a model for its activation by the regulation of cAMP levels.

TREK1 as a candidate I_{sAHP} channel

It has become increasingly evident that K2P channels play a role in generating slow currents. Metabotropic GABAB receptors use cAMP-dependent disinhibition of TREK2 channels to generate second-long hyperpolarizations (Deng et al. 2009; Sandoz et al. 2012). Similarly, serotonin activates TWIK-1 via a decrease in cAMP (Deng et al. 2007) or inhibits TASK-1 channels via a G alpha q pathway (Talley et al. 2000) to alter neuronal excitability. Similarly, metabotropic glutamate receptors activate phospholipase C and inhibit TREK and TASK channels, generating slow depolarizations in neurons (Chemin et al. 2003). Thus, the slow modulation of second messengers, including cAMP and IP3, seems to be read out by K2P channels so they can generate slow hyperpolarizations and depolarizations.

In agreement, our results implicate the K2P channel TREK1 in the generation of I_{sAHP} in retinal SACs using several lines of evidence. First, during development, SACs are enriched for *kcnk2* transcripts, the mRNA that encodes the TREK1 channel (Fig. 3*B*). Second, I_{sAHP} was insensitive to a variety of K-channel antagonists that are also known not to block K2P channels. In particular, TEA (1 mM), 4-AP (1 mM), cesium (2 mM), apamin (1 μM), and tolbutamide (100 μM) do not inhibit I_{sAHP}.(Figs. 1 and 2). Thus, we can rule out the involvement of voltage-gated, A-type, SK, BK, or ATP-dependent potassium channels and I_h. Third, the I_{sAHP} was blocked by 2 mM barium, a blocker of the K2P channel subfamilies TASK, TREK, TWIK, and TRESK (Fig. 3*A*). Fourth, application of the fatty acid AA increased I_{sAHP} (Fig. 3*A*), consistent with the observation that some K2P channels are activated by manipulating pressure, pH, and lipids (Enyedi and Czirjak 2010; Lesage and Lazdunski 2000). Fifth, at physiological potassium concentrations, I_{sAHP} was outwardly rectified (Fig. 1), consistent with the outward rectification of K2P channels (Goldstein et al. 2005). Furthermore, this outward rectification excludes the possibility that I_{sAHP} is mediated by inwardly rectified channels that are sensitive to barium, such as K_{atp}. Sixth, I_{sAHP} is inhibited by blockade of the calcium-dependent phosphodiesterase PDE1C (Fig. 3*A*), consistent with the known inhibition of TREK channels by PKA phosphorylation. Seventh, mice lacking TREK1 display an increase in wave frequency (Fig. 5), consistent with the frequency increase seen with decreased I_{sAHP} (Fig. 4).

A cAMP model for the activation of I_{sAHP}

A hallmark of both TREK channels and the channels underlying the sAHPs in other neurons is their regulation by intracellular signaling cascades. PKA phosphorylation inhibits TREK channels (Honore et al. 2002) and inhibits the channels underlying the sAHPs in hippocampal pyramidal neurons (Lancaster et al. 2006; Lancaster and Nicoll 1987; Sah and Isaacson 1995). In developing retinal SACs, forskolin, which elevates cAMP levels, inhibits I_{sAHP} (Ford et al. 2012), indicating that I_{sAHP} is sensitive to cAMP levels.

This finding could explain how TREK channels generate sAHPs in SACs even though I_{sAHP} requires calcium influx for activation while TREK channels are not activated by changes in intracellular calcium (Fink et al. 1996). The activation of I_{sAHP} occurs over several seconds, suggesting that channel opening following depolarization is mediated by a signaling cascade, rather than the direct activation of calcium. Calcium influx can activate adenylyl cyclases (ACs) and PDEs and thus can regulate levels of cAMP. Decreases in cAMP have been shown to activate TREK channels with the activation of metabotropic GABA (Deng et al. 2009; Sandoz et al. 2012) and glutamate receptors (Chemin et al. 2003; Lesage et al. 2000). Thus, calcium entry could regulate cAMP levels that would then control the TREK channel that produces I_{sAHP}.

We propose a model for this mechanism, although it is important to note that this study does not specifically address the mechanism underlying calcium activation of the conductance. During depolarization, calcium influx through voltage-gated calcium channels (Zheng et al. 2006) may activate calcium-dependent PDE1C and cause a decrease in cAMP. We note that other pathways may also contribute to this calcium-dependent decrease in cAMP. Some adenylate cyclases, including AC5, AC6, and AC9, are inhibited by intracellular calcium signaling (Halls and Cooper 2011). Of these, AC5 and AC9 are expressed within the retina early in development (Nicol et al. 2006), although their specific localization is unknown. The decrease in cAMP caused by these potential pathways and by calcium influx may lead to activation of the channel underlying the sAHP. The corresponding decrease in PKA activity would then produce a decrease in phosphorylation that disinhibits the channel. In support of this idea, TREK1 channels in neurons associate with PKA anchoring proteins (AKAPs) that allow for rapid regulation by PKA (Sandoz et al. 2006). Furthermore, I_{sAHP} in hippocampal CA1 neurons is modulated by both PKA and phosphatases (Pedarzani et al. 1998), suggesting that a balance between kinase and phosphatase activity actively regulates the channel phosphorylation state.

The role of I_{sAHP} in retinal waves

Retinal waves during the first postnatal week in mice critically depend on cholinergic transmission from SACs but not on other neurotransmitters (Bansal et al. 2000; Stacy et al. 2005; Wang et al. 2007). SACs are spontaneously active (Ford et al. 2012; Zheng et al. 2006), and stimulation of a single SAC is sufficient to initiate a wave (Ford et al. 2012). Thus, a network of SACs is both necessary and sufficient for generating retinal waves.

The intrinsic conductances in SACs dictate the spatio-temporal properties of retinal waves. During development of the visual system, the distinct spatio-temporal features convey information to target regions (Ackman et al. 2012;Bansal et al. 2000; Penn et al. 1994; Xu et al. 2011). Several computational models have been developed to investigate how the intrinsic properties of SACs give rise to the frequency, propagation speed, and spatial coverage of waves (Ford et al. 2012; Godfrey and Swindale 2007; Hennig et al. 2009). Each of these models relies on the spontaneous depolarization of SACs to initiate waves, the local excitatory connections to allow propagation, and a slow afterhyperpolarization to limit propagation of waves into recently active regions. Recent experimental evidence has indicated that decreasing the sAHP by elevating cAMP levels increases wave frequency (Ford et al. 2012;Zheng et al. 2006). In accordance, here we have shown that inhibiting calcium-activated PDE1C decreases I_{sAHP} and wave frequency. This is consistent with predictions from modeling studies (Ford et al. 2012; Godfrey and Swindale 2007; Hennig et al. 2009). Furthermore, we have shown that animals lacking TREK1 exhibit waves with double the frequency of wild-type waves. Thus, our data support a role for TREK1 in generating the sAHP in SACs that limits wave frequency.

Why are waves not more frequent than 2–3 waves per minute when the sAHP is blocked or reduced? The sAHP prevents the propagation of waves into recently active regions but is not the only mechanism that sets wave frequency. The frequency of retinal waves is determined by the spontaneous depolarization rate of SACs. In mice, SACs are spontaneously active only about once every 10 min when neurotransmitters are blocked (but see in rabbit Zheng et al. 2006; Ford et al. 2012). This slow intrinsic depolarization rate may set an upper limit to the wave frequency when the sAHP is reduced. Alternatively, a reduction in sAHP might be compensated for with additional cellular mechanisms. During initial whole cell recordings, we found a K_{atp}-mediated conductance following depolarizing voltage steps (Fig. 2). While this conductance was not activated during less invasive perforated patch recordings, a K_{atp}-mediated sAHP may occur when sAHP is inhibited and causes excessive depolarization that depletes energy levels.

Acknowledgements

We thank Prof. Diana Bautista for sanshool extract and many useful discussions. We thank Prof. Sam Wu and Cameron Cowan at Baylor Univ. for the generous use of multielectrode array. Present addresses: K. J. Ford: Dept. of Biochemistry and Biophysics, Univ. of California, San Francisco, San Francisco, CA; J. Kay: Depts. of Neurobiology and Ophthalmology, Duke Univ., Durham, NC.

RO1-EY-013528F31-NS-614663R01-EY-022073R01NS-046666R21-HL-098921 National Institutes of Health

References

Abel HJ, Lee JC, Callaway JC, Foehring RC. Relationships between intracellular calcium and afterhyperpolarizations in neocortical pyramidal neurons. J Neurophysiol 91: 324 –335, 2004.

Ackman JB, Burbridge TJ, Crair MC. Retinal waves coordinate patterned activity throughout the developing visual system. Nature 490: 219 –225, 2012.

Bansal A, Singer JH, Hwang BJ, Xu W, Beaudet A, Feller MB. Mice lacking specific nicotinic acetylcholine receptor subunits exhibit dramatically altered spontaneous activity patterns and reveal a limited role for retinal waves in forming ON and OFF circuits in the inner retina. J Neurosci 20: 7672–7681, 2000.

Bautista DM, Sigal YM, Milstein AD, Garrison JL, Zorn JA, Tsuruda PR, Nicoll RA, Julius D. Pungent agents from Szechuan peppers excite sensory neurons by inhibiting two-pore potassium channels. Nat Neurosci 11: 772–779, 2008.

Blankenship AG, Ford KJ, Johnson J, Seal RP, Edwards RH, Copenhagen DR, Feller MB. Synaptic and extrasynaptic factors governing glutamatergic retinal waves. Neuron 62: 230 – 241, 2009.

Chemin J, Girard C, Duprat F, Lesage F, Romey G, Lazdunski M. Mechanisms underlying excitatory effects of group I metabotropic glutamate receptors via inhibition of 2P domain K channels. EMBO J 22: 5403–5411, 2003.

Czirjak G, Toth ZE, Enyedi P. The two-pore domain K channel, TRESK, is activated by the cytoplasmic calcium signal through calcineurin. J Biol Chem 279: 18550 –18558, 2004.

Deng PY, Poudel SK, Rojanathammanee L, Porter JE, Lei S. Serotonin inhibits neuronal excitability by activating two-pore domain k channels in the entorhinal cortex. Mol Pharmacol 72: 208 –218, 2007.

Deng PY, Xiao Z, Yang C, Rojanathammanee L, Grisanti L, Watt J, Geiger JD, Liu R, Porter JE, Lei S. GABA(B) receptor activation inhibits neuronal excitability and spatial learning in the entorhinal cortex by activating TREK-2 K channels. Neuron 63: 230 –243, 2009.

Dunn TA, Storm DR, Feller MB. Calcium-dependent increases in protein kinase-A activity in mouse retinal ganglion cells are mediated by multiple adenylate cyclases. PLoS One 4: e7877, 2009.

Enyedi P, Czirjak G. Molecular background of leak K currents: two-pore domain potassium channels. Physiol Rev 90: 559 – 605, 2010.

Faber ES, Sah P. Physiological role of calcium-activated potassium currents in the rat lateral amygdala. J Neurosci 22: 1618 –1628, 2002.

Fink M, Duprat F, Lesage F, Reyes R, Romey G, Heurteaux C, Lazdunski M. Cloning, functional expression and brain localization of a novel unconventional outward rectifier K channel. EMBO J 15: 6854 – 6862, 1996.

Ford KJ, Felix AL, Feller MB. Cellular mechanisms underlying spatiotemporal features of cholinergic retinal waves. J Neurosci 32: 850 – 863, 2012.

Godfrey KB, Swindale NV. Retinal wave behavior through activity-dependent refractory periods. PLoS Comput Biol 3: e245, 2007.

Goldberg JA, Teagarden MA, Foehring RC, Wilson CJ. Nonequilibrium calcium dynamics regulate the autonomous firing pattern of rat striatal cholinergic interneurons. J Neurosci 29: 8396 – 8407, 2009.

Goldstein SA, Bayliss DA, Kim D, Lesage F, Plant LD, Rajan S. International union of pharmacology. LV. Nomenclature and molecular relationships of two-P potassium channels. Pharmacol Rev 57: 527–540, 2005.

Halls ML, Cooper DM. Regulation by Ca2-signaling pathways of adenylyl cyclases. Cold Spring Harb Perspect Biol 3: a004143, 2011.

Hennig MH, Adams C, Willshaw D, Sernagor E. Early-stage waves in the retinal network emerge close to a critical state transition between local and global functional connectivity. J Neurosci 29: 1077–1086, 2009.

Hirst GD, Johnson SM, van Helden DF. The slow calcium-dependent potassium current in a myenteric neurone of the guinea-pig ileum. J Physiol 361: 315–337, 1985.

Honore E, Maingret F, Lazdunski M, Patel AJ. An intracellular proton sensor commands lipid- and mechano-gating of the K() channel TREK-1. EMBO J 21: 2968 –2976, 2002.

Ivanova E, Hwang GS, Pan ZH. Characterization of transgenic mouse lines expressing Cre recombinase in the retina. Neuroscience 165: 233–243, 2010.

Kay JN, Chu MW, Sanes JR. MEGF10 and MEGF11 mediate homotypic interactions required for mosaic spacing of retinal neurons. Nature 483: 465– 469, 2012.

Kay JN, De la Huerta I, Kim IJ, Zhang Y, Yamagata M, Chu MW, Meister M, Sanes JR. Retinal ganglion cells with distinct directional preferences differ in molecular identity, structure, and central projections. J Neurosci 31: 7753–7762, 2011.

Lancaster B, Adams PR. Calcium-dependent current generating the afterhyperpolarization of hippocampal neurons. J Neurophysiol 55: 1268 –1282, 1986.

Lancaster B, Hu H, Gibb B, Storm JF. Kinetics of ion channel modulation by cAMP in rat hippocampal neurones. J Physiol 576: 403– 417, 2006.

Lancaster B, Nicoll RA. Properties of two calcium-activated hyperpolarizations in rat hippocampal neurones. J Physiol 389: 187–203, 1987.

Lee K, Duan W, Sneyd J, Herbison AE. Two slow calcium-activated afterhyperpolarization currents control burst firing dynamics in gonadotropin-releasing hormone neurons. J Neurosci 30: 6214 – 6224, 2010.

Lesage F. Pharmacology of neuronal background potassium channels. Neuropharmacology 44: 1–7, 2003.

Lesage F, Lazdunski M. Molecular and functional properties of two-poredomain potassium channels. Am J Physiol Renal Physiol 279: F793–F801, 2000.

Lesage F, Terrenoire C, Romey G, Lazdunski M. Human TREK2, a 2P domain mechano-sensitive K channel with multiple regulations by polyunsaturated fatty acids, lysophospholipids, and Gs, Gi, and Gq proteincoupled receptors. J Biol Chem 275: 28398 – 28405, 2000.

Lorenzon NM, Foehring RC. Relationship between repetitive firing and afterhyperpolarizations in human neocortical neurons. J Neurophysiol 67: 350 –363, 1992.

Mathie A. Neuronal two-pore-domain potassium channels and their regulation by G protein-coupled receptors. J Physiol 578: 377–385, 2007.

Namiranian K, Lloyd EE, Crossland RF, Marrelli SP, Taffet GE, Reddy AK, Hartley CJ, Bryan RM Jr. Cerebrovascular responses in mice deficient in the potassium channel, TREK-1. Am J Physiol Regul Integr Comp Physiol 299: R461–R469, 2010.

Nicol X, Bennis M, Ishikawa Y, Chan GC, Reperant J, Storm DR, Gaspar P. Role of the calcium modulated cyclases in the development of the retinal projections. Eur J Neurosci 24: 3401–3414, 2006.

Pedarzani P, Krause M, Haug T, Storm JF, Stuhmer W. Modulation of the Ca2-activated Kcurrent sIAHP by a phosphatase-kinase balance under basal conditions in rat CA1 pyramidal neurons. J Neurophysiol 79: 3252– 3256, 1998.

Penn AA, Wong RO, Shatz CJ. Neuronal coupling in the developing mammalian retina. J Neurosci 14: 3805–3815, 1994.

Pulver SR, Griffith LC. Spike integration and cellular memory in a rhythmic network from Na/K pump current dynamics. Nat Neurosci 13: 53–59, 2010.

Sah P. Ca2-activated K currents in neurones: types, physiological roles and modulation. Trends Neurosci 19: 150 –154, 1996.

Sah P, Faber ES. Channels underlying neuronal calcium-activated potassium currents. Prog Neurobiol 66: 345–353, 2002.

Sah P, Isaacson JS. Channels underlying the slow afterhyperpolarization in hippocampal pyramidal neurons: neurotransmitters modulate the open probability. Neuron 15: 435– 441, 1995.

Sandoz G, Levitz J, Kramer RH, Isacoff EY. Optical control of endogenous proteins with a photoswitchable conditional subunit reveals a role for TREK1 in GABA(B) signaling. Neuron 74: 1005–1014, 2012.

Sandoz G, Thummler S, Duprat F, Feliciangeli S, Vinh J, Escoubas P, Guy N, Lazdunski M, Lesage F. AKAP150, a switch to convert mechano-, pHand arachidonic acid-sensitive TREK K() channels into open leak channels. EMBO J 25: 5864 –5872, 2006.

Santone R, Giorgi M, Maccarone R, Basso M, Deplano S, Bisti S. Gene expression and protein localization of calmodulin-dependent phosphodiesterase in adult rat retina. J Neurosci Res 84: 1020 –1026, 2006.

Schwindt PC, Spain WJ, Foehring RC, Chubb MC, Crill WE. Slow conductances in neurons from cat sensorimotor cortex in vitro and their role in slow excitability changes. J Neurophysiol 59: 450 – 467, 1988.

Stacy RC, Demas J, Burgess RW, Sanes JR, Wong ROL. Disruption and recovery of patterned retinal activity in the absence of acetylcholine. J Neurosci 25: 9347–9357, 2005.

Stosiek C, Garaschuk O, Holthoff K, Konnerth A. In vivo two-photon calcium imaging of neuronal networks. Proc Natl Acad Sci USA 100: 7319 –7324, 2003.

Talley EM, Lei Q, Sirois JE, Bayliss DA. TASK-1, a two-pore domain K channel, is modulated by multiple neurotransmitters in motoneurons. Neuron 25: 399 – 410, 2000.

Talley EM, Sirois JE, Lei Q, Bayliss DA. Two-pore-domain (KCNK) potassium channels: dynamic roles in neuronal function. Neuroscientist 9: 46 –56, 2003.

Tanner GR, Lutas A, Martinez-Francois JR, Yellen G. Single KATP channel opening in response to action potential firing in mouse dentate granule neurons. J Neurosci 31: 8689 – 8696, 2011.

Tian G, Sa˚getorp J, Xu Y, Shuai H, Degerman E, Tengholm A. Role of phosphodiesterases in the shaping of sub-plasma membrane cAMP oscillations and pulsatile insulin secretion. J Cell Sci 125: 5084 –5095, 2012.

Torborg CL, Feller MB. Spontaneous patterned retinal activity and the refinement of retinal projections. Prog Neurobiol 76: 213–235, 2005.

Tzingounis AV, Kobayashi M, Takamatsu K, Nicoll RA. Hippocalcin gates the calcium activation of the slow afterhyperpolarization in hippocampal pyramidal cells. Neuron 53: 487– 493, 2007.

Villalobos C, Andrade R. Visinin-like neuronal calcium sensor proteins regulate the slow calcium-activated afterhyperpolarizing current in the rat cerebral cortex. J Neurosci 30: 14361–14365, 2010.

Villalobos C, Foehring RC, Lee JC, Andrade R. Essential role for phosphatidylinositol 4,5-bisphosphate in the expression, regulation, and gating of the slow afterhyperpolarization current in the cerebral cortex. J Neurosci 31: 18303–18312, 2011.

Vogalis F, Harvey JR, Furness JB. Suppression of a slow post-spike afterhyperpolarization by calcineurin inhibitors. Eur J Neurosci 19: 2650 – 2658, 2004.

Vogalis F, Harvey JR, Neylon CB, Furness JB. Regulation of K channels underlying the slow afterhyperpolarization in enteric afterhyperpolarizationgenerating myenteric neurons: role of calcium and phosphorylation. Clin Exp Pharmacol Physiol 29: 935–943, 2002.

Wang CT, Blankenship AG, Anishchenko A, Elstrott J, Fikhman M, Nakanishi S, Feller MB. GABA(A) receptor-mediated signaling alters the structure of spontaneous activity in the developing retina. J Neurosci 27: 9130 –9140, 2007.

Watanabe D, Inokawa H, Hashimoto K, Suzuki N, Kano M, Shigemoto R, Hirano T, Toyama K, Kaneko S, Yokoi M, Moriyoshi K, Suzuki M, Kobayashi K, Nagatsu T, Kreitman RJ, Pastan I, Nakanishi S. Ablation of cerebellar Golgi cells disrupts synaptic integration involving GABA inhibition and NMDA receptor activation in motor coordination. Cell 95: 17–27, 1998.

Xu HP, Furman M, Mineur YS, Chen H, King SL, Zenisek D, Zhou ZJ, Butts DA, Tian N, Picciotto MR, Crair MC. An instructive role for patterned spontaneous retinal activity in mouse visual map development. Neuron 70: 1115–1127, 2011.

Yellen G. Ionic permeation and blockade in Ca2-activated K channels of bovine chromaffin cells. J Gen Physiol 84: 157–186, 1984.

Zheng J, Lee S, Zhou ZJ. A transient network of intrinsically bursting starburst cells underlies the generation of retinal waves. Nat Neurosci 9: 363–371, 2006.

Figure 1: Slow afterhyperpolarization (sAHP) in starburst amacrine cells (SACs) is mediated by a two-pore potassium channel.

A: current clamp perforated patch recording of SAC shows sAHP evoked by 500-ms 100-pA current injection in presence of 5 μM gabazine and 8 μM dihydro-β-erthryoidine. *Inset* shows expanded version of initial spike (Scale: 10 mV, 100 ms). *B*: voltage clamp perforated patch recording of SAC shows I_{sAHP} evoked by 500-ms voltage step to −14 mV from a holding potential of −64 mV. Trace shows average from $n = 32$ cells with gray indicating ±SD. *C*, *left*: voltage protocol used to determine current voltage relationship of I_{sAHP}. Average I_{sAHP} is shown above for reference. A series of 50-ms voltage steps to different holding potentials was given before and at the peak of I_{sAHP}. Scale: 2 pA, 10 s. *C*,*right*, *inset*: example current traces from voltage steps before (*1*) and after (*2*) depolarizing step to activate I_{sAHP}. Scale: 10 pA, 10 ms. Graph shows average current voltage relationship at peak of I_{sAHP}. $N = 4$, means ± SD. *D*: reversal potential as a function of external potassium concentration. Dots represent individual cells; boxes indicate mean. Line is fit to prediction from Nernst equation for a potassium conductance. *E*: example conductance (*top*) and current (*bottom*) measurements taken from a baseline of −64 mV following a 500-ms voltage step to −14 mV. Conductance was determined from trains of 50-ms, 10-mV hyperpolarizing steps. *Inset*: voltage protocol used to determine conductance. *F*, *top*: average current evoked by 500-ms voltage step to −14 mV, as in *B–D*, in the presence (black) and absence (gray) of external calcium ($n = 4$), apamin (1 μM, $n = 5$), and TEA (1 mM, $n = 5$). *F*, *bottom*: peak amplitude of evoked currents for each cell before (Pre) and after (Post) application. Boxes represent the mean; error bars indicate SE. Scale: 2 pA, 10 s.

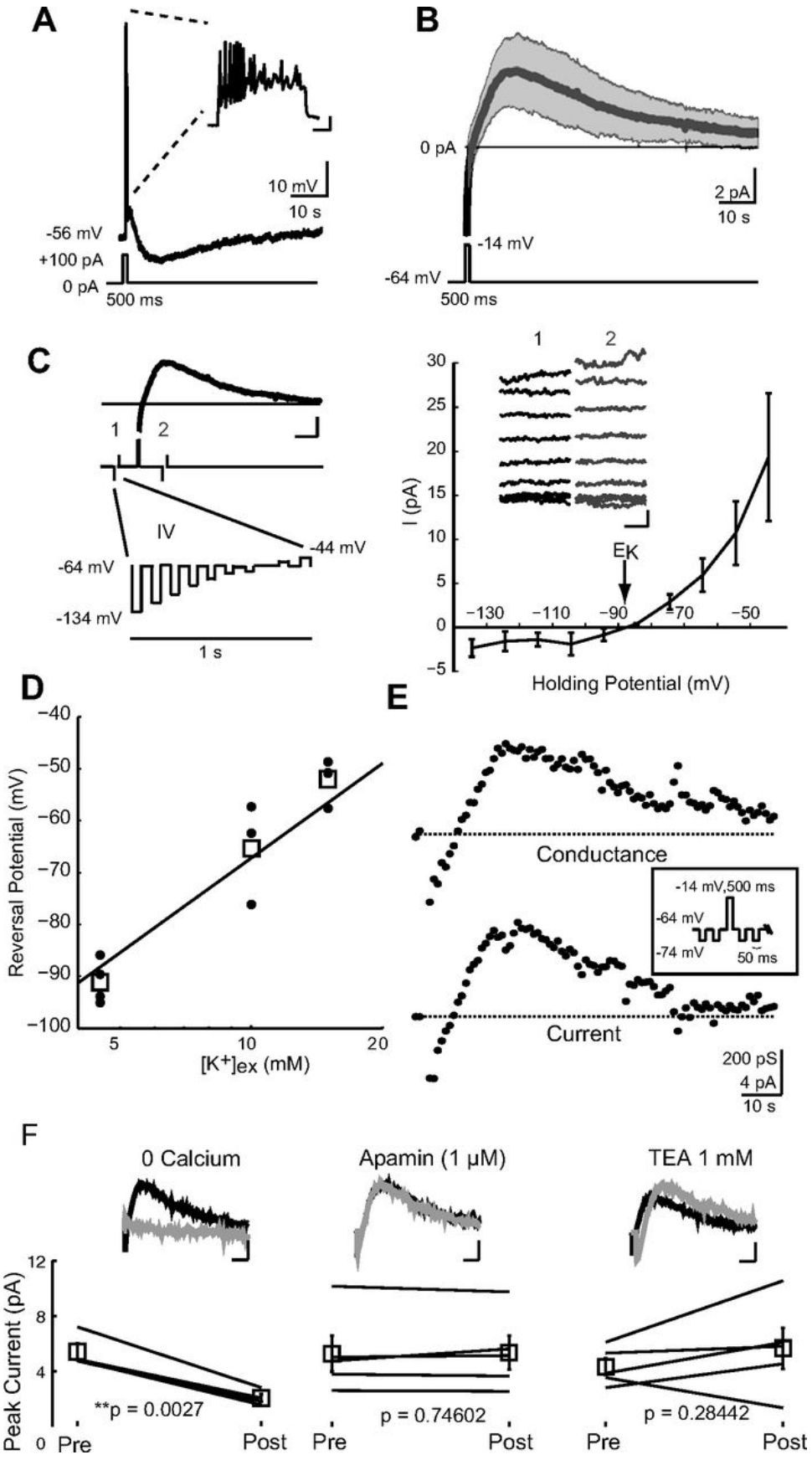
A
10 mV
10 s
-56 mV
+100 pA
0 pA
500 ms
B
0 pA
2 pA
10 s
-14 mV
-64 mV
500 ms
C
1
2
IV
-64 mV
-44 mV
-134 mV
1 s
1
2
I (pA)
EK
Holding Potential (mV)
D
Reversal Potential (mV)
[K+]ex (mM)
E
Conductance
-14 mV,500 ms
-64 mV
-74 mV
50 ms
Current
200 pS
4 pA
10 s
F
0 Calcium
Apamin (1 μM)
TEA 1 mM
Peak Current (pA)
**p = 0.0027
p = 0.74602
p = 0.28442
Pre
Post

Figure 2: Whole cell recordings from SACs reveal a K_{atp} conductance.

A: whole cell voltage clamp recording from SAC. Cell is voltage clamped at −64 mV. Arrows indicate 500-ms voltage step to −14 mV followed by return to −64 mV. Dashed lines indicate changes in holding current at −64 mV in control, tolbutamide (100 μM), and rinse. *B*: peak amplitude of transient outward current following 500-ms depolarizing voltage step in whole cell configuration in the absence and presence of tolbutamide application (n = 5). *C*, *left*: example current clamp perforated patch recordings of sAHPs evoked by 500-ms, 100-pA current injection before and during tolbutamide bath application. *C*, *middle*: example voltage clamp perforated patch recording of I_{sAHP} evoked by 500-ms step from −64 mV to −14 mV, before and during tolbutamide bath application. *C*, *right*: peak amplitude of I_{sAHP} following 500-ms depolarizing voltage step in perforated patch configuration before and during tolbutamide application (n = 5).

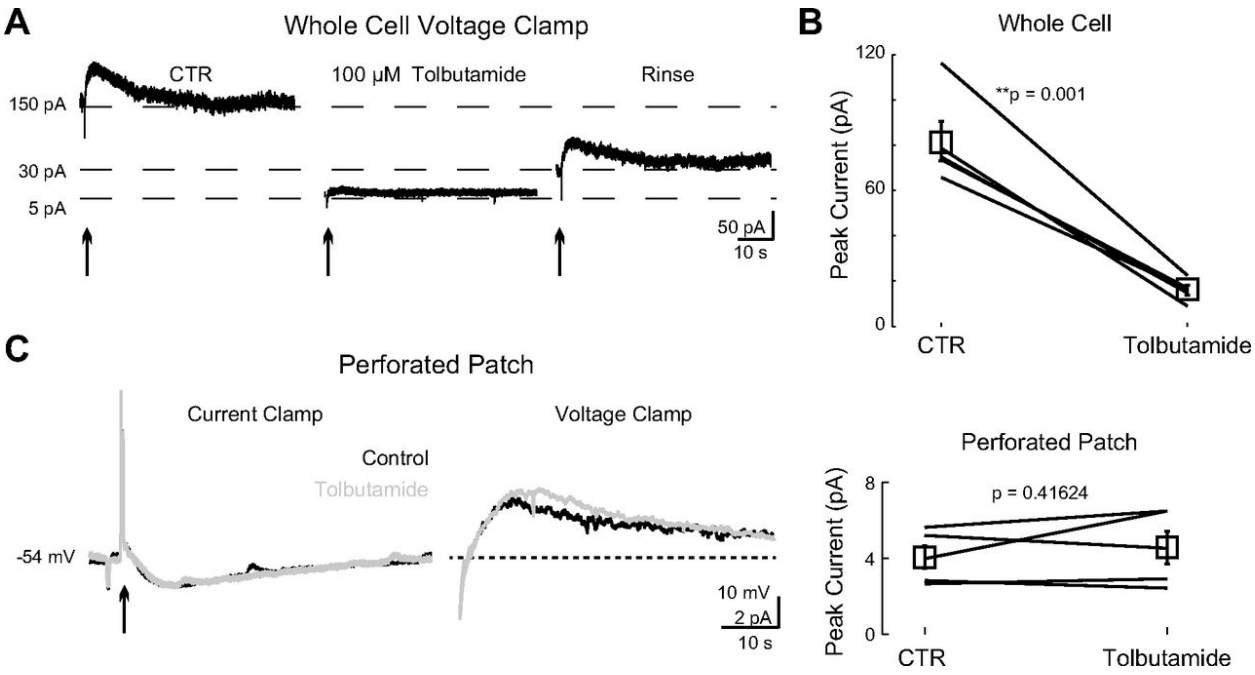
A
Whole Cell Voltage Clamp
CTR
100 µM Tolbutamide
Rinse
150 pA
30 pA
5 pA
50 pA
10 s
B
Whole Cell
**p = 0.001
Peak Current (pA)
120
60
0
CTR
Tolbutamide
C
Perforated Patch
Current Clamp
Voltage Clamp
Control
Tolbutamide
-54 mV
10 mV
2 pA
10 s
Perforated Patch
p = 0.41624
Peak Current (pA)
8
4
0
CTR
Tolbutamide

Figure 3: I_{sAHP} has the pharmacological characteristics of K2P channels.
A, *top*: peak amplitude of I_{sAHP} before (Pre) and during (Post) bath application of barium (2 mM as $BaCl_2$, $n = 7$), sanshool extract (0.02%, $n = 4$), arachidonic acid (10 μM, $n = 7$), or MMPX (100 μM, $n = 8$).*A*, *bottom*: average current evoked by 500-ms voltage step from −64 mV to −14 mV, in control (black) and during application of each drug (gray). Scale: 2 pA, 10 s. *B*: expression of the Kcnk gene family, which encodes K2P channels, was assessed in mouse retinal neurons using microarrays. Heatmap shows expression of the Kcnk genes across 13 different retinal neuron subtypes, which include subtypes of retinal ganglion cells (RGCs), amacrine cells (ACs), and bipolar cells (BCs). Color (red, high; blue, low; see bottom for scale) indicates gene expression level in each cell type relative to mean level for that gene. Unsupervised hierarchical clustering was used to determine the *x*-axis order in which the genes are listed, such that genes with similar expression patterns across the 13 cell types are found next to each other. All 13 members of the Kcnk family are represented at least once (some are represented twice because they appeared twice on the microarray). Expression of Kcnk2, the gene encoding TREK1, is specific to SACs, as shown both by the heatmap and by the fact that it clustered with two known SAC-specific genes, Chat and Vacht.

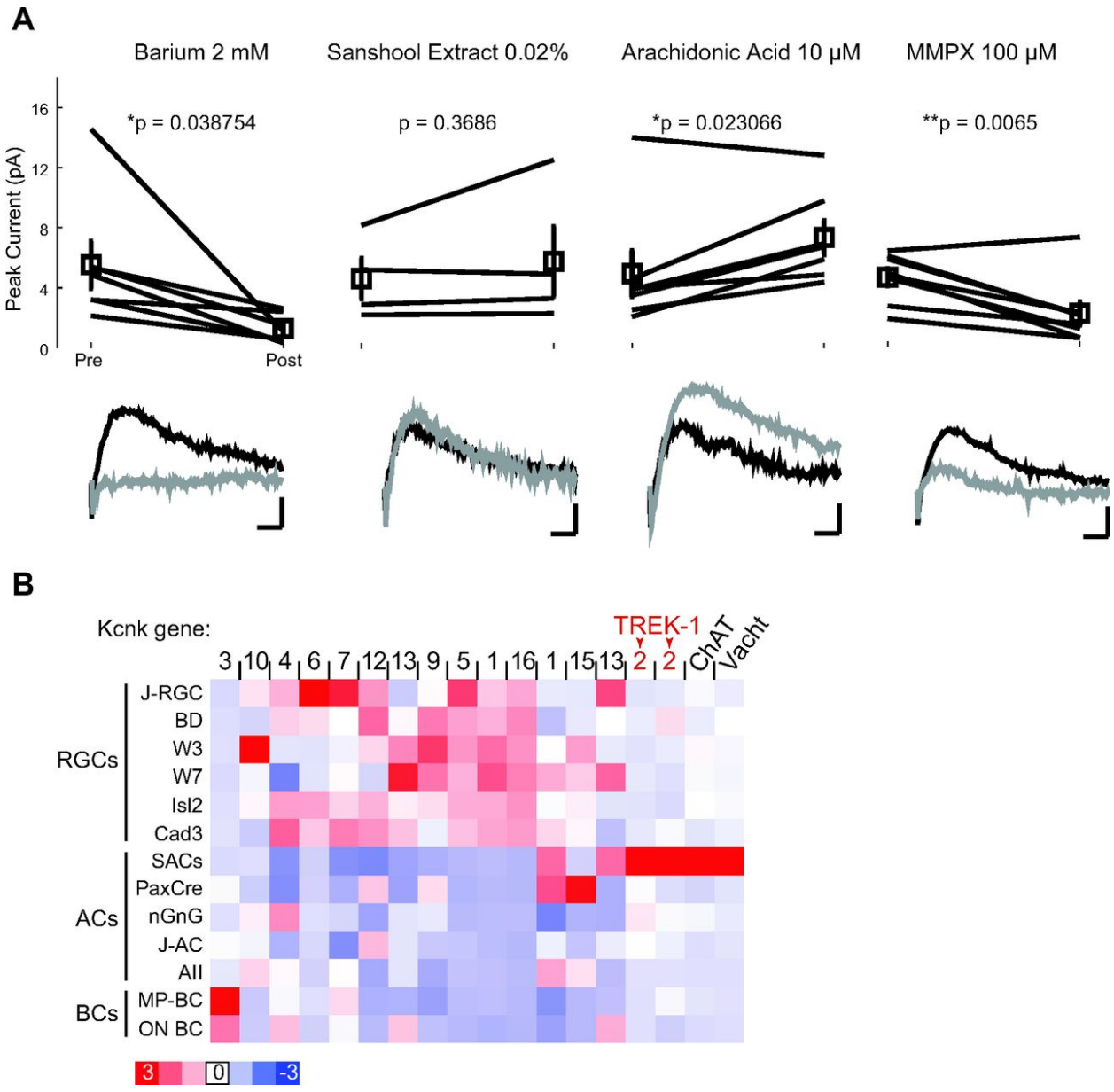
A
Barium 2 mM
Sanshool Extract 0.02%
Arachidonic Acid 10 µM
MMPX 100 µM
Peak Current (pA)
16
12
8
4
0
*p = 0.038754
p = 0.3686
*p = 0.023066
**p = 0.0065
Pre
Post
B
Kcnk gene:
TREK-1
3 10 4 6 7 12 13 9 5 1 16 1 15 13 2 2 ChAT Vacht
RGCs
J-RGC
BD
W3
W7
Isl2
Cad3
ACs
SACs
PaxCre
nGnG
J-AC
AII
BCs
MP-BC
ON BC
3
0
-3

Figure 4: Modulation of sAHP alters the frequency of spontaneous retinal waves.
A: calcium imaging of retinal waves. *A*, *left*: fluorescence image of a retina that is bolus loaded with OGB-1AM. Scale: 100 μm. *A*, *right*: pseudo-colored images show time progression of wave fronts. Each panel represents the activity during 4 consecutive 20-s time periods. Wave fronts are colored according to their location during the 20-s period, with darker colors occurring earlier in the period (see color scale). Black indicates the absence of a wave. *Top* shows a control retina, and *bottom* shows the same retina during application of 100 μM MMPX. *B*: mean interwave interval (relative to control) measured by calcium imaging in the presence of MMPX (100 μM), tolbutamide (100 μM), and cesium (2 mM as CsCl). Number of retinas per manipulation is shown on each bar. Means ± SD. **P* = 0.001.

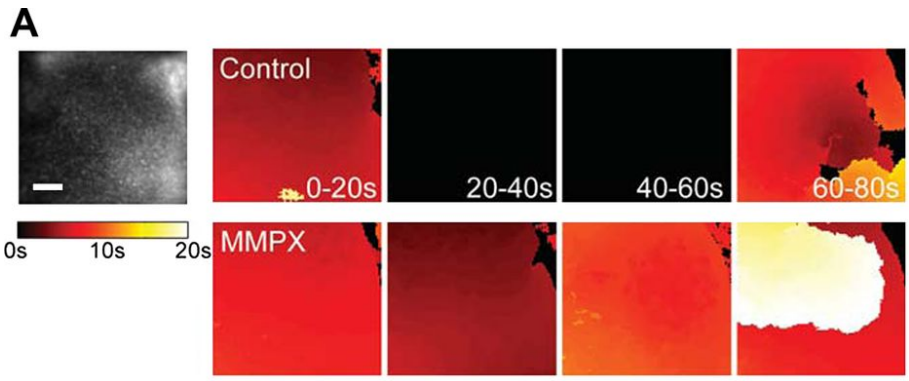
A
Control
0-20s
20-40s
40-60s
60-80s
0s
10s
20s
MMPX

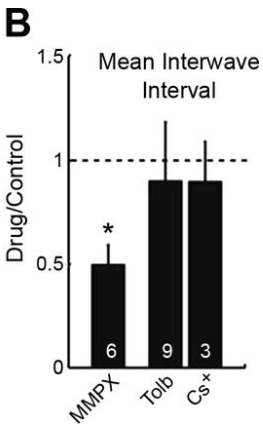
B
Mean Interwave Interval
Drug/Control
1.5
1
0.5
0
*
6
9
3
MMPX
Tolb
Cs+

Figure 5: TREK1−/− mice exhibit more frequent cholinergic retinal waves.
A: raster plots of single-unit spike trains over a 20-min period recorded from retinas of P1 WT (*top*) and TREK1−/− (*bottom*) mice. *B*: summary histograms show distribution of interwave intervals from WT (*top*,*n* = 4) and TREK1−/− (*bottom*, *n* = 4) retinas. *C*: average interwave intervals for WT (*n* = 52 waves from 4 retinas) and TREK1−/− (*n* = 83 waves from 4 retinas) mice. Error bars indicate SD; **P* < 0.001.

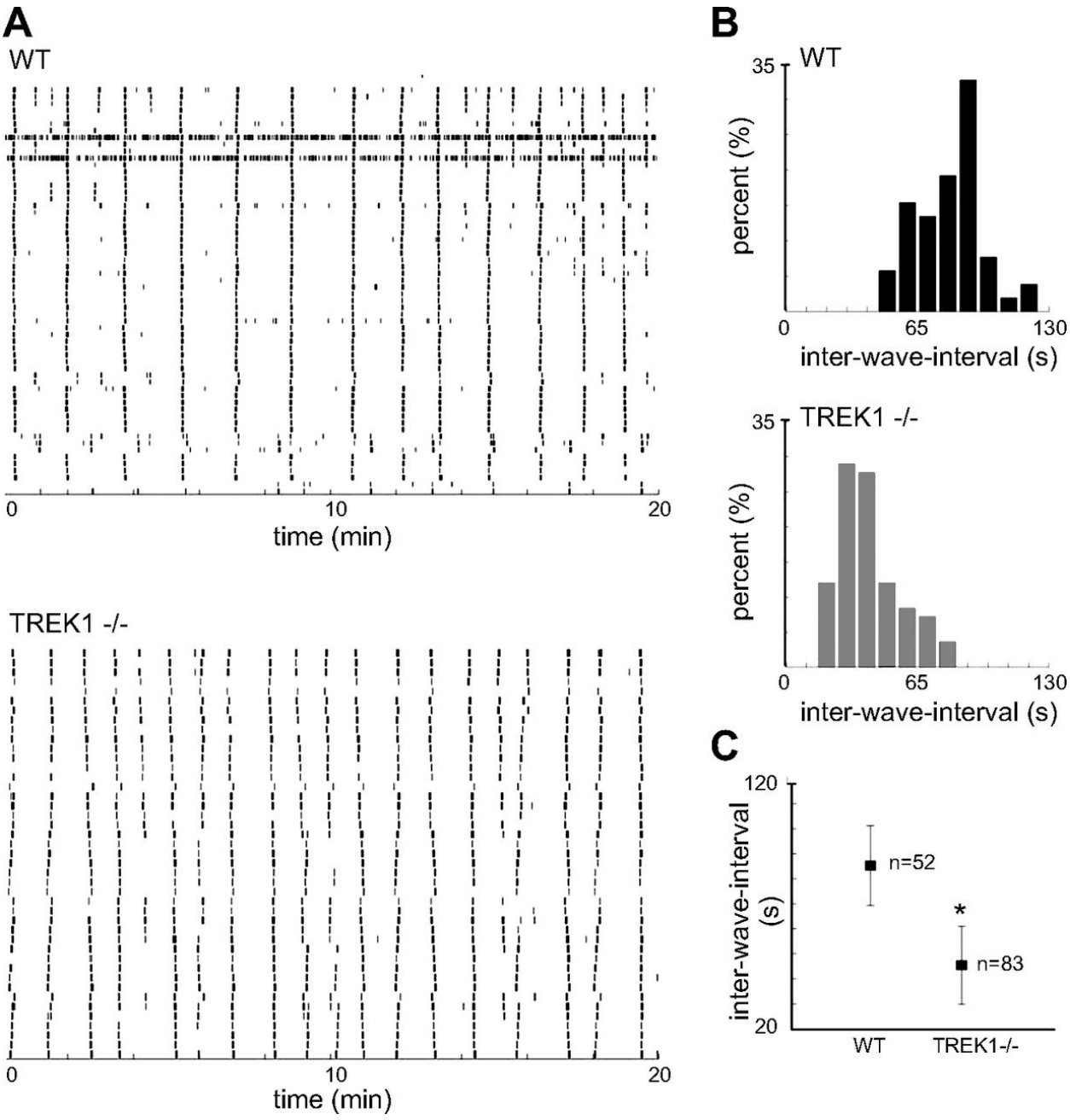
A
WT
0
10
20
time (min)
TREK1 -/-
0
10
20
time (min)
B
WT
35
percent (%)
0
65
130
inter-wave-interval (s)
TREK1 -/-
35
percent (%)
0
65
130
inter-wave-interval (s)
C
120
inter-wave-interval (s)
20
n=52
*
n=83
WT
TREK1-/-

III. Retinal waves modulate an intra-retinal circuit of intrinsically photosensitive retinal ganglion cells

Abstract

Before the maturation of rod and cone photoreceptors, the developing retina relies on light detection by intrinsically photosensitive retinal ganglion cells (ipRGCs) to drive early light-dependent behaviors. IpRGCs are output neurons of the retina, however they also form functional microcircuits within the retina itself. Whether ipRGC microcircuits exist during development and whether they influence early light detection remains unknown. Here, we investigate the neural circuit that underlies the ipRGC-driven light response in developing mice. We use a combination of calcium imaging, tracer coupling and electrophysiology experiments to show that ipRGCs form extensive gap junction networks that strongly contribute to the overall light response of the developing retina. Interestingly, we found that gap junction coupling was modulated by spontaneous retinal waves, such that acute blockade of these waves dramatically increased the extent of coupling and hence increased the number of light-responsive neurons. Moreover, using an optical sensor, we found that this wave-dependent modulation of coupling is driven by dopamine that is phasically released by retinal waves. Our results demonstrate that ipRGCs form gap junction microcircuits during development that are modulated by retinal waves; these circuits determine the extent of the light response and thus potentially impact the processing of early visual information and light-dependent developmental functions.

Significance

Light-dependent functions in early development are mediated by intrinsically photosensitive retinal ganglion cells (ipRGCs). Here we show that ipRGCs form an extensive gap junction network with other retinal neurons, including other ipRGCs, which shapes the retina's overall light response. Blocking cholinergic retinal waves, which are the primary source of neural activity before maturation of photoreceptors, increased the extent of ipRGC gap junction networks, thus increasing the number of light responsive cells. We determined that this modulation of ipRGC gap junction networks occurs via dopamine released by waves. These results demonstrate that retinal waves mediate dopaminergic modulation of gap junction networks to regulate pre-vision light responses.

Introduction

Across the developing nervous system, immature networks generate correlated spontaneous activity between neighboring groups of cells (reviewed in (Blankenship and Feller, 2010; H. C. Wang and Bergles, 2015; Wenner, 2012)). This phenomenon has been well studied in the retina, where prior to eye-opening, retinal waves are mediated by cholinergic signaling and propagate throughout the developing visual system (Ackman et al., 2012). Retinal waves are critical for establishing retinotopic and eye-specific maps in both the superior colliculus and lateral geniculate nucleus of the thalamus (reviewed in (Ackman and Crair, 2014; Huberman et al., 2008; Kirkby et al., 2013)).

The effect of waves on the development of early neural circuits within the retina is less well understood (Kerschensteiner, 2013). They are known to influence dendritic growth and synapse formation (Bansal et al., 2000; Lohmann et al., 2002; W. T. Wong and R. O. Wong, 2001) Additionally, they have been implicated in network plasticity of the developing retina, whereby in the absence of cholinergic retinal waves, "recovered waves" mediated by gap junctions emerge (Kirkby and Feller, 2013; Stacy et al., 2005; Stafford et al., 2009; Sun et al., 2008). These recovered waves propagate more rapidly than cholinergic waves, cover a larger area, and are modulated by dopaminergic signaling. We previously suggested that the gap junction networks underlying recovered waves are suppressed by cholinergic signaling (Kirkby and Feller, 2013), which highlights the dynamic interaction between these two different wave-generating circuits.

Interestingly, the circuits mediating recovered waves (Kirkby and Feller, 2013), and to some extent those of cholinergic waves (Renna et al., 2011), strongly interact with intrinsically photosensitive retinal ganglion cells (ipRGCs). In both cases, light stimulation of ipRGCs increases retinal wave activity, suggesting that intra-retinal microcircuits carry ipRGC inputs. IpRGCs express the photopigment melanopsin and contribute to non-image-forming functions of vision, such as entrainment of circadian rhythms (Berson et al., 2002; Hattar et al., 2003; Rollag et al., 2003). Being the first photoreceptor to mature, ipRGCs provide the first visual input to retinal circuits and their brain targets (Fahrenkrug et al., 2004; Schmidt et al., 2008; Sekaran et al., 2005; Tu et al., 2005). IpRGCs are output neurons of the retina, however there is growing evidence that they additionally form functional microcircuits within the retina (Müller et al., 2010; Reifler et al., 2015; Zhang et al., 2012; 2008). The contribution of intra-retinal ipRGC microcircuits to early light responses during development remains unknown.

Here we explore the neural circuits underlying the ipRGC-driven light responses of the developing retina and the mechanisms by which retinal waves regulate these circuits. We use both anatomical and physiological methods to demonstrate that ipRGCs are extensively gap junction coupled to each other during development, and that the extent of coupling increases in the absence of cholinergic waves. We show that this coupling is regulated by dopamine released during retinal waves. Moreover, we demonstrate that even in the presence of cholinergic waves, ipRGC gap junction networks propagate light-driven signals at both the single cell and whole retina level, thus strongly contributing to the overall light response of the developing retina.

Methods

Animals. All experiments were performed on mice aged postnatal day P4–P7 of either sex from C57BL/6 WT (Harlan Laboratories, Indianapolis) or Opn4-EGFP (P. Kofuji, Minnesota University, Minneapolis(Schmidt et al., 2008)) lines. Animal procedures were approved by the University of California, Berkeley Institutional Animal Care and Use Committees and conformed to the National Institutes of Health Guide for the Care and Use of Laboratory Animals, the Public Health Service Policy, and the Society for Neuroscience Policy on the Use of Animals in Neuroscience Research. Animals were anesthetized with isofluorane and decapitated, and the eyes were enucleated. Retinas were removed from eyecups in 95% O2–5% (vol/vol) CO2 bicarbonate buffered artificial cerebrospinal fluid (ACSF, in mM: 119 NaCl, 26.2 NaHCO3, 11 glucose, 2.5 KCl, 1 K2HPO4, 2.5 CaCl2, 1.3 MgCl2).

Whole-mount retinal preparations. Isolated retinas were mounted RGC-side up on filter paper. Retinas were dark adapted for at least 30 minutes at room temperature in oxygenated ACSF until transfer to the recording chamber, where they were continually superfused (1–2 ml/min) with oxygenated ACSF at 29–32°C.

Electrophysiology and neurobiotin fills. Retinas were visualized through a window cut in the filter paper with differential interference contrast optics on a ZEISS Axioskop 2 FS plus microscope under an ACHROPLAN 40x water-immersion objective. IpRGCs were identified by GFP signal in Opn4-EGFP mice under epifluorescent illumination, at 470/40 excitation filter and 525/50 emission filter. A hole was pierced in the inner limiting membrane of the retina using a glass recording pipette to access the RGC layer. RGCs were targeted under control of a micromanipulator (MP-225, Sutter Instruments). Recording pipettes were pulled with a tip resistance of 6–7 MΩ (for Neurobiotin) or 4–5 MΩ (for voltage clamp) and filled with internal solution (Neurobiotin fills, in mM: 116 K^+ D-Gluconate, 6 KCl, 2 NaCl, 20 HEPES, 0.5 EGTA, 4 ATP-Na_2, 0.3 GTP-Na_3, 10 phosphocreatine-Na_2, 0.05 Neurobiotin; Voltage clamp recordings, in mM: 110 $CsMeSO_4$, 2.8NaCl, 20 HEPES, 4 EGTA, 5 TEA-Cl, 4 ATP-Mg, 0.3 GTP-Na_3, 10 phosphocreatine-Na_2, 5 QX 314-Br; Cell-attached recordings, in mM: 150 NaCl) containing 0.02 mM Alexa-594. Data were acquired using pCLAMP 10.2 recording software and a Multiclamp 700B amplifier (Molecular Devices), sampled at 10 kHz and filtered between 160 and 2,000 Hz.

For tracer coupling experiments, Neurobiotin Tracer (Nb, 0.5%, SP-1120, Vector laboratories) was added to internal solution. Cells were voltage-clamped and pipettes were removed after a 5-minute diffusion of neurobiotin internal solution. Retinas were incubated for 25 minutes in the recording chamber after pipette removal. Cell morphology was assessed after pipette removal to confirm good cell health. Tissue was subsequently fixed and immunolabeled for neurobiotin and the marker of interest (e.g. GFP, Figure 2), and imaged on a confocal scanning microscope **(**Zeiss LSM 780 NLO AxioExaminer, Molecular Imaging Center at UC Berkeley). The depth series of optical slices (1 µm between slices) was acquired using a Zeiss 20x water-immersion objective. Cell counts were performed by hand on each optical slice, and stacks were reconstructed offline using ImageJ max intensity projections for figure presentation.

Whole-cell voltage-clamp recordings were obtained using glass microelectrodes of 4-5 MΩ (PC-10 pipette puller, Narishige). Holding voltage (V_h) for measuring photocurrents after correction

of the liquid junction potential (-13 mV) was -60 mV. Signals were acquired using pCLAMP 9 recording software and a Multiclamp 700A amplifier (Molecular Devices), sampled at 20 kHz and low-pass filtered at 2 kHz. Spikelets and spikes were defined as events with amplitudes 2 standard deviations above the mean and with spacing more than 5 ms apart using a custom MATLAB protocol. Traces were analyzed 200 ms at a time to avoid artifacts from slow transient currents. Irradiance-response curves were performed in cell-attached mode. Light was delivered using a tungsten halogen lamp together with an optical filter at 480±4 nm. Firing rates were measured in response to a 5 s pulse of full-field 480 nm illumination of increasing light intensity. Light intensity was adjusted using optical density (OD) filters. All firing rates were normalized to the maximal response at OD = 0 (no filter present), corresponding to an irradiance of approximately 2.4 x 10^{14} photons $s^{-1}cm^{-2}$.

Alexa dye injections. Retinas were visualized through a window cut in the filter paper with differential interference contrast optics, as described above. Injection pipettes were pulled with a tip resistance of 20-30 MΩ (Sutter Instruments) and back-filled with a 10mM solution (in 200mM KCl) of Alexa Fluor 594 hydrazide. Cells were impaled with the pipette and dye was injected with negative current of 0.1-0.9 nA, 200 ms long pulses at 2 Hz. Samples were fixed for immunoreactions 5 minutes after injection.

Immunoassays. Whole-mount retinas were removed from recording chamber and transferred to a 4% paraformaldehyde solution for 30 min at room temperature. Following fixation, retinas were washed in PBS for 20 min at room temperature and remounted onto a new piece of filter paper. They were incubated in blocking buffer (1.5% BSA, 0.2% Na-Azide, 0.2% Triton X-100) (3X 15 min) and then in primary immunoreaction solution. Concentrations of the different primary reactants in blocking buffer were 1:1000 goat (ABCAM) or rabbit (Invitrogen) anti-GFP (24h at 4ºC), 1:2500 rabbit anti-melanopsin (48h at 4ºC, Advanced Targeting Systems) and 1:1000 rabbit anti-TH (24h at 4ºC, ABCAM), 1:750 goat anti-Brn3a (Santa Cruz Biotechnology), 1:50 goat anti-Brn3b (Santa Cruz Biotechnology), 1:500 rabbit anti-GABA (Sigma-Aldrich). After primary reaction, retinas were washed in PBS (3X 15min), and then incubated for 3h at room temperature in 1:200 concentrations of secondary antibodies: donkey anti-rabbit or donkey anti-goat (Invitrogen). Neurobiotin was stained using a 1:800 streptavidin-594 (Invitrogen) solution in blocking buffer.

Calcium imaging and visual stimulation. Retinas were bulk loaded with the calcium indicator Oregon Green BAPTA-1 AM (OGB-1) using the multi-cell bolus loading technique and epifluorescent imaging described previously (Blankenship et al., 2009). Excitation light was filtered with a 470/40 optical filter and yielded approximately 3.4 x 10^{15} photons $s^{-1}cm^{-2}$ to maximally stimulate the ipRGC intrinsic light response. Time series images of 30 or 40 seconds were acquired at 2 Hz with a 225 ms exposure time using a 40X water immersion objective. Elliptical regions of interest were manually drawn around cells displaying increases in fluorescence within the first 7 seconds after imaging onset. Cells were classified as light responsive if they exhibited ΔF/F above threshold within 7 s of light onset in two consecutive trials spaced 10 minutes apart. Thresholds were determined for each experiment and ranged from ΔF/F = 1.2 - 5%).

Multi-electrode array recordings. Isolated pieces of retina were placed RGC-side down onto a

60-electrode commercial multi-electrode array (MEA) that was arranged in an 8X8 grid, excluding the four corners, with 10μm diameter electrodes at a 100μm inter-electrode spacing (Multi Channel Systems). The retina was held in place using a dialysis membrane weighted with a ring of platinum wire. The recording chamber was superfused with oxygenated ACSF and maintained between 30-34°C. Preparations were stimulated with unfiltered broad-band full-field light delivered by a tungsten halogen lamp with irradiance (in photons $s^{-1}cm^{-2}$) of $2.4x10^{12}$ at 480nm and $2.9x10^{13}$ at 600 nm. Raw data were filtered between 120 and 2000 Hz, and spikes were sorted offline to identify single units using Plexon Offline Sorter software. Spike-sorted data were analyzed in MATLAB (Mathworks). Units that showed an increase in firing rate following light onset were classified as light responsive. Cross-correlograms (CCGs) of light responsive units were calculated using MATLAB's cross-correlogram function. Cells were categorized as being coupled if their normalized CCG between +/- 2.5ms was 0.7 or lower than between 2.5-7.5ms.

High performance liquid chromatography (HPLC). Whole retinal eye cups were dissected from both eyes and flash frozen in liquid nitrogen. Liquid nitrogen vials were sent to the Vanderbilt Neurochemistry Core Laboratory for dopamine analysis using HPLC with electrochemical detection.

Fluorescence resonance energy transfer (FRET) imaging. D2 cell-based neurotransmitter fluorescent engineered reporters (CNiFERs) were kindly provided by D. Kleinfeld and P. Slesinger (UCSD) (Muller et al., 2014). CNiFERs were maintained in a humidified incubator at 37°C with 5% (v/v) CO_2 in growth media containing Dulbecco's Minimum Essential Medium (DMEM, containing 4.5g/L glucose, L-glutamine and Na pyruvate; Invitrogen) supplemented with 10% heat-inactivated Fetal Bovine Serum (Invitrogen). Cells were trypsinized (0.05%), triturated, and seeded into new flasks at a density ratio of 1:5 upon confluence (approximately every 2–3 days).

Imaging of CNiFERs was based on previous methods using ACh-CNiFERS described in (Ford et al., 2012). Before experiments, CNiFERs were removed from culture flasks using brief (30 second) application of trypsin (0.05%) and were concentrated in growth media. CNiFERs were deposited onto the inner limiting membrane (ILM) by using a micropipette to transfer solution on top of a filter-mounted retinal piece, mounted ganglion cell side up, and then allowing them to settle onto the surface. Clusters of 2–3 cells were imaged at the focal plane ~5–10μm above the ILM. We used 5-minute imaging windows since CNiFER cells migrated out of the imaging field of view over time periods longer than this. We performed simultaneous patch clamp recordings of RGCs ~50–200μm from the imaged CNiFERs. Fluorescence resonance energy transfer (FRET) images were acquired at 2 Hz using a 60X objective and an excitation wavelength of 435 nm. Individual FRET channel detection was accomplished by using a Dual-View image splitter (Optical Insights) with appropriate yellow and cyan channel filters. Background fluorescence was subtracted from both channels. FRET ratios were computed as background-corrected YFP/CFP fluorescence averaged over a region of interest around a single CNiFER.

We quantified the time lag between each FRET transient and the closest wave by measuring the time from the peak of each FRET increase to the trough of the closest wave-associated EPSC (Figure 5). We compared these results to time-shuffled data to assess the likelihood of our

observed temporal correlation occurring by chance. This involved first measuring the means and standard deviations of the wave and FRET rates from our dataset, then simulating recordings using the measured rates while assuming that the two events occurred independently of one another, and then calculating the time between each FRET transient and its closest wave.

Pharmacology. Di-hydro-β-erythroidine (DHβE, 8 μM), D-(-)-2Amino-5-phosphonopentanoic acid (D-AP5, 50 μM), 6,7-Dinitroquinoxaline-2,3-dione (DNQX, 20 μM), SR-95531 (Gabazine, 5μM), Strychnine (4 μM), Meclofenamic acid (MFA, 50 μM) and SCH23390 hydrochloride (SCH, 10 μM), Raclopride (8 μM), Tetrodotoxin (TTX, 1 mM) were added to perfusion media as stock solutions prepared in distilled water. QX 314 Bromide (5 mM) was added to the internal solution. Antagonists were purchased from Tocris Bioscience. The synaptic cocktail consisted of a mixture of Gabazine, Strychnine, D-AP5, DNQX, and, when specified, DHβE, at the above concentrations.

Results

Acutely blocking retinal waves increases the number of light responsive cells

We first characterized the impact of acutely blocking waves on the overall light response of the developing retina. To characterize the ipRGC-mediated light response, we simultaneously stimulated melanopsin in ipRGCs and the calcium indicator Oregon Green Bapta-1 (OGB-1) with epifluorescent light, as used in previous studies (Bramley et al., 2011; Sekaran et al., 2005; 2003). This led to a transient increase in fluorescence in a subset of neurons in the ganglion cell layer (Figures 1A and C) that corresponded to spiking activity (Figure 1B). There are multiple subtypes of ipRGCs (M1-M5) distinguished by their light sensitivity, morphology, molecular identity and projection targets in the brain (reviewed in (Schmidt et al., 2011)). At least three of these subtypes emerge early in development (Schmidt et al., 2008; Sexton et al., 2015; Tu et al., 2005). Our intensity of imaging light (3.4×10^{15} photons $s^{-1}cm^{-2}$ at 480 nm) should maximally activate all subtypes of ipRGCs at this age (Schmidt et al., 2008; Sexton et al., 2015; Tu et al., 2005). We then repeated these experiments after acutely blocking retinal waves with the nicotinic acetylcholine receptor (nAChR) antagonist di-hydro-β-erythroidine (DHβE, 8μM) for 60 minutes. Wave blockade produced a 2-fold increase in the number of cells that exhibited light-evoked calcium transients (Figures 1C and D; DHβE/control = 2.11 ± 0.88, n = 12 retinas), agreeing with our previous work that describes the emergence of a light-sensitive network in the absence of cholinergic signaling (Kirkby and Feller, 2013). This increase in light responses was insensitive to combined blockade of GABAergic, glutamatergic, glycinergic and cholinergic input, indicating that it was not due to a change in synaptic input from these neurotransmitters (Figure 1D, n = 6).

In a subset of experiments, we targeted light responsive neurons for intracellular dye injections and subsequently immunostained them for melanopsin (Figure 1E). In control conditions, the majority of neurons that exhibited light-evoked calcium transients were positive for melanopsin immunoreactivity (n = 12/13). In contrast, after cholinergic blockade, the majority of neurons that had gained a light response tested negative for melanopsin immunoreactivity (n = 1/5 positive), indicating that they themselves did not have a robust intrinsic light response but rather had inherited it through input from nearby ipRGCs. This high incidence of melanopsin expression among light responsive cells in control conditions is in contrast with previous reports suggesting that, at P4-P5, only 56% of light responsive cells are ipRGCs since 44% lose their light sensitivity in the presence of gap junction blockers (Sekaran et al., 2005). Our observed higher incidence of melanopsin-expressing ipRGCs could be attributed to two factors; first, our targeted injections were biased towards cells with larger somas, therefore it might favor particular subtype of ipRGCs with abundant melanopsin expression. Second, a subset of ipRGCs might require gap junction input to generate a robust light response thus losing their light response in the presence of gap junction blockers. This possibility is explored below.

Increase in the number of light responsive cells occurs via increased gap junction coupling

We hypothesized that the increased number of light responsive cells after wave blockade is due to modulation of ipRGC gap junction coupling. In adult retina, ipRGCs are tracer-coupled (Müller et al., 2010) and electrically coupled via gap junctions (Reifler et al., 2015) to wide-field

spiking GABAergic amacrine cells. However, during development, calcium imaging experiments suggest that there is gap junction coupling between ipRGCs and other neurons (Sekaran et al., 2005).

Thus we tested if gap junction coupling underlies the increased number of light responsive neurons in the absence of retinal waves using several approaches. We first performed tracer-coupling experiments. We filled GFP-expressing ipRGCs in the Opn4-EGFP mouse, which labels M1-M3 ipRGC subtypes (Schmidt et al., 2008), with the gap junction permeable tracer neurobiotin (Nb) using a patch pipette (6-7 MΩ tip resistance). After a 60 minute blockade of retinal waves with DHβE, we found that the number of neurons tracer-coupled to these ipRGCs increased significantly (Figure 2A and B, mean ± SD; control: tracer-coupled cells = 13.90 ± 5.65, n = 10 injected neurons; DHβE: tracer-coupled cells = 22.82 ± 9.26, n = 11). Additionally, we discovered that a subset of the coupled neurons expressed GFP (Figure 2A), and their number increased slightly but significantly after a 60 minute blockade of retinal waves (Figure 2B, control: GFP+ tracer-coupled cells = 4.33 ± 1.86, n = 6 cells; DHβE: GFP+ tracer-coupled cells = 6.73 ± 1.95, n = 11). Hence, our findings indicate that ipRGCs are coupled to other ipRGCs and to cells that do not express detectable GFP, which suggests that ipRGCs might propagate their light responses to neurons with low or non-existent melanopsin expression.

We characterized the spatial arrangement of GFP+ and GFP- coupled cells both prior to and after 60 min blockade of retinal waves. Though the overall distribution of coupled cells did not change with wave blockade (Figure 2D), we found that the distribution of somas of GFP- tracer-coupled cells was skewed toward inside of the dendritic field while the distribution of GFP+ tracer-coupled cells was skewed toward outside the dendritic field (Figure 2E, control and DHβE data grouped together).

We further explored the cell types comprising the gap junction networks of developing ipRGCs by conducting a series of co-labeling experiments in which the tracer-coupled cells were tested for molecular markers of retinal cell types. We found that Nb colocalized with the ganglion cell marker Brn3b, which predominantly labels the M2-M5 ipRGC subtypes, a subset of M1 ipRGCs as well as a variety of other RGCs (Chen et al., 2011; Jain et al., 2012), but rarely colocalized with Brn3a, which does not label ipRGCs (Jain et al., 2012) (Figure $2F_{i\text{-}ii}$ and G). The presence of Brn3b and not Brn3a in the tracer-coupled cells indicate that ipRGCs are preferentially coupled to other ipRGCs and avoid other retinal ganglion cells (RGCs). We found that tracer-coupled cells rarely colocalized with GABA (Figure $2F_{iii}$ and G), in contrast to the tracer-coupling pattern described for adult ipRGCs (Müller et al., 2010). Additionally, tracer-coupled cells did not co-localize with tyrosine hydroxylase (TH), which labels dopaminergic amacrine cells—a putative post-synaptic target of ipRGCs (Zhang et al., 2012; 2008)(Figure $2F_{iv}$ and G). It is important to note that we did not observe correlations between ipRGC morphologies and coupling patterns, hence we did not distinguish between ipRGC subtypes in our analyses (Figure 2F bottom). Our tracer-coupling observations show that ipRGCs are extensively tracer-coupled to other cells, including other ipRGCs, and that this coupling increases when cholinergic waves are blocked.

We next investigated if there is functional coupling of ipRGCs to other retinal neurons via gap junctions. For our first test, we determined if the depolarization of a single ipRGC (identified by their light-evoked calcium transient, see Figure 1) propagates to the post-junctional retinal

neurons. To isolate electrical signaling, we performed these experiments in a cocktail of synaptic blockers (see Methods). Indeed, we found that short depolarizing steps in ipRGCs evoked calcium transients in nearby, though not adjacent, cells, indicating gap junction coupling (Singer et al., 2001) (Figure 3A and B). After a 60 minute blockade of retinal waves with DHβE, we saw a significant increase in the number of post-junctional neurons (Figure 3C: control: number of cells with evoked calcium transient = 2.12 ± 1.13 n = 8; DHβE: number of cells with evoked calcium transient = 4.0 ± 1.22, n = 5). Under both experimental conditions, a subset of these post-junctional neurons exhibited light-evoked calcium transients. (Figure 3D; control: 5 of 17 cells; DHBE: 12 of 20 cells), which indicates that coupling occurs between both ipRGCs and non-ipRGCs and is consistent with the tracer-coupling results. The amplitudes of depolarization-evoked calcium transients were similar in control and DHβE (Figure 3E; $DF/F_{control}$ = 3.5 ± 2.3%; $DF/F_{DH\beta E}$ = 2.6 ± 1.2%), suggesting that the increase in coupled cells observed after blocking waves is dominated by formation of new connections or dramatic strengthening of pre-existing gap junction synapses.

For our second test of physiological coupling, we used multielectrode array (MEA) recordings to determine if light-evoked action potentials propagate via gap junctions. Similar to our calcium imaging results, we observed an increase in the number of light-responsive cells (seen as individual units after spike sorting) following DHβE application (DHβE/control = 1.39 ± 0.26, control/control = 1.10 ± 0.07, n = 8 retinas, data not shown; example raster plot in Figure 4A). The new light-responsive cells displayed lower peak firing rates than the original light-responsive cells but similar latency-to-peak (Figure 4B and C). Since ipRGC subtypes are classified in part by latency (Sexton et al., 2015; Tu et al., 2005), our observations suggest that these new light-responsive cells do not correspond to a distinct subtype of ipRGC, but rather are cells receiving input via gap junctions in the absence of an intrinsically-driven component. After DHβE application, the original light-responsive cells displayed no significant changes in light-evoked firing rates, latency-to-peak or irradiance-response curves, suggesting that DHβE does not alter the intrinsic light response properties of these ipRGCs (Figure 4C and D). To further confirm that the light-responsive cells are gap junction coupled, we computed cross-correlograms (CCGs) of light-responsive cells and found that several pairs displayed the characteristic double peak structure of direct electrical coupling (Brivanlou et al., 1998; DeVries, 1999), including cells that had gained a light response in DHβE (Figure 4E; 220 out of 816 possible pairs of light responsive units, n = 6 retinas). Furthermore, we observed direct coupling in CCGs of some pairs in control conditions, albeit with a broader distribution that is likely indicative of common input (Figure 4E; 54 pairs total, n = 6 retinas).

Taken together, our findings demonstrate that during development, ipRGCs are gap junction coupled to a variety of neurons, including other ipRGCs, and that the extent of this coupling increases in the absence of cholinergic wave-related signaling.

Cholinergic retinal waves regulate ipRGC coupling via dopamine release

How does blocking cholinergic waves increase the coupling of ipRGCs? In adult retina, the regulation of gap junction networks is mediated primarily by the neuromodulator dopamine (Bloomfield and Völgyi, 2009; Witkovsky et al., 2004), which is released from dopaminergic amacrine cells (DACs) upon ambient illumination (Zhang et al., 2007) and reaches ipRGCs,

activating their type-1 dopamine receptors (D1R) (Van Hook et al., 2012). Since this dopamine release is driven by photoreceptor activation (Zhang et al., 2007), it is unclear if dopamine is released early in development before the maturation of photoreceptors. Our previous study suggests that this is indeed the case because we found that gap junction networks in the developing retina are modulated by dopaminergic receptors (Kirkby and Feller, 2013). Thus we tested the hypothesis that retinal waves drive dopamine release, which in turn modulates ipRGC gap junction coupling during development.

First, we confirmed the presence of dopaminergic amacrine cells (DACs) (Yoshida et al., 2011) by immunostaining for TH between postnatal ages P4-P6 (Figure 5A, left). Second, we showed that dopamine is produced and metabolized during these ages using high performance liquid chromatography (HPLC) with electrochemical detection (Figure 5A, right). Third, we directly tested if cholinergic waves correlate with the diffuse release of dopamine by using a cell-based dopamine sensor (CNiFER) technique (Muller et al., 2014) previously used for ACh-sensing CNiFERs (Ford and Feller, 2012; Nguyen et al., 2010) (Figure 5B). We found that the sensor displayed transient FRET increases, indicating a diffuse release of dopamine (Figure 5C and D). Simultaneous voltage clamp recordings from nearby RGCs revealed that these FRET increases lagged wave-induced currents by 20–30 seconds (Figures 5C and E). This lag is due to a variety of factors. First, the sensor itself has relatively slow responses. Direct application of dopamine to the sensor leads to time-to-peak of the FRET increase of roughly 5-10 seconds, as previously reported (Muller et al., 2014) (see inset, Figure 5I). Second, the density of dopaminergic amacrine cells, which reside in the inner-nuclear layer, is very low, roughly 100 μm^{-2} (Figure 5A) which corresponds to 1-2 within our imaging field. Hence the dopamine likely needs to diffuse a long distance before reaching the sensor that resides on the surface of the inner-limiting membrane. In comparison, we used the ACh-CNiFER in the same location and in the presence of a high density of ACh-releasing interneurons, many of which reside in the ganglion cell layer, and we also saw long delays of roughly 10-15 seconds (Ford et al., 2012).

We evaluated the likelihood of the observed 20–30 sec correlation between a retinal wave and a FRET transient occurring and found that it was significantly higher than that expected by chance (see Methods, Figure 5E), suggesting that retinal waves induce the FRET transients. However not all waves were followed by a FRET transient (Figure 5D), and in these cases the prior wave was linked to a large FRET increase (Figure 5F). We could reproduce this phenomenon using consecutive puffs of high-potassium solution (K-puff) to the IPL (Figure 5G), indicating that it might be a limitation in the response dynamics of the CNiFER and not a lack of wave-evoked dopamine release. To determine the impact of retinal waves on dopamine release, we blocked cholinergic waves with DHβE and found that there was a dramatic decrease in the frequency of FRET transients (control: 0.64 ± 0.15 transients/min; DHβE: 0.12 ± 0.07 transients/min, $n = 10$, $p < 0.05$) and their amplitude (Figure 5H), corresponding to approximately a 10-fold decrease in dopamine concentration per transient (Figure 5I). Thus, we conclude that cholinergic waves induce diffuse release of dopamine, and that blocking them reduces this release.

To test if this dopamine signaling influences ipRGC gap junction coupling, we blocked D1Rs with the antagonist SCH 23390 (SCH, 10μM). Blocking D1Rs, which has no effect on cholinergic retinal waves (Kirkby and Feller, 2013), induced a 5-fold increase in the number of light-responsive neurons (Figure 6; SCH/control = 5.53 ± 2.68, $n = 8$ retinas). This increase was greater than that induced by blocking cholinergic waves (Figure 1), likely due to the residual

dopamine that is still present during wave blockade (Figure 5H). In contrast, blocking D2-type dopamine receptors (raclopride, 8 μM) or ionotropic glutamatergic receptors (DNQX, 20 μM), which are possible pathways for dopaminergic modulation (discussed below), did not change the number of light-responsive neurons (Figure 6B; raclopride/control = 0.87 ± 0.23, n = 4, DNQX/control = 0.99 ± 0.23, n = 6), indicating that alternate dopaminergic pathways and intra-retinal glutamatergic circuits of ipRGCs do not play a significant role in wave-driven dopaminergic modulation of ipRGC gap junctions. Our result of increased coupling in D1R antagonist agrees with several other studies showing that D1R antagonists increase coupling in retinal circuits via changes in gap junction phosphorylation (Bloomfield and Völgyi, 2009; Kothmann et al., 2009).

Together, these data describe a putative mechanism by which waves regulate the extent of ipRGC gap junction networks via dopamine release that modulates gap junction coupling.

Gap junction coupling of ipRGCs contributes to the overall light response of the developing retina

Our tracer coupling and physiology experiments (Figures 2 and 3) indicate that ipRGC gap junction coupling is robust in the presence of cholinergic waves, which corresponds to a condition of high dopamine release. This leads to the question: does gap junction coupling of ipRGCs influence the light response in normal conditions, when wave-driven dopamine release diminishes gap junction connectivity? To address this, we investigated how gap junction coupling contributes to the light response of ipRGCs.

We conducted whole-cell voltage clamp recordings of ipRGCs in response to blue light (λ = 450-490nm, intensity = 3.4 x 10^{15} photons $s^{-1}cm^{-2}$), which maximally stimulates all ipRGC subtypes (Berson et al., 2002; Do and Yau, 2010). Superimposed on the slow photocurrents that are characteristic of ipRGCs (Do and Yau, 2010), we detected small, inward, transient currents resembling spikelets (Figure 7A-B, n = 10 cells). Spikelets are transient depolarizations that originate in prejunctional neurons, travel through gap junctions and via the dendrites to the soma of the postjunctional cell. They have been demonstrated to represent a physiological trademark of gap junction coupling between several different classes of neurons (Landisman and Connors, 2005; Pereda, 2014; Valiante et al., 1995) including the retina (Trenholm et al., 2013a; 2013b). These ipRGC spikelets were blocked by the sodium channel blocker tetrodotoxin (TTX, 1μM) and exhibited shorter inter-spike intervals than light-evoked action potentials, suggesting that they originate from the spiking of multiple pre-junctional cells (Figure 7A-C, n = 7). It is important to note that the inter-spike intervals of action potentials during light responses are too long to be accounted for by action potential refractory periods so refractory period was not used to compare action potentials and spikelets. Therefore further study will be required to directly test that spikelets emerge from multiple ipRGCs. Importantly, spikelets were recorded using intracellular solutions that contain the sodium channel blocker QX 314 (5 mM), indicating that they are not generated by spikes in the voltage-clamped neuron but rather in the pre-junctional ipRGCs.

Since gap junctions act as low pass filters, we might expect that action potentials originating in pre-junctional neurons contribute only a small depolarization to a post-junctional neuron

(Trenholm et al., 2013a). However, the slow photocurrents associated with activation of melanopsin should be less filtered as they pass through gap junctions. Thus we tested how gap junction coupling contributes to ipRGC light responses by blocking gap junctions to effectively eliminate inputs from pre-junctional ipRGCs during light stimulation. We compared photocurrents in the absence and presence of the gap junction blocker meclofenamic acid (MFA, 50μM, Figure 7D), and found that photocurrents recorded in MFA exhibited significantly smaller amplitudes than those recorded in control (ACSF: peak amplitude = 49.56 ±16.29 pA, n = 11 cells; MFA: peak amplitude = 18.96 ±9.06 pA, n = 12 cells; Figure 7D and E). Compared to control, MFA did not cause a significant difference in the input resistance of ipRGCs, as previously described for this age (Schmidt et al., 2008). There still remains the possibility that MFA is impacting unclamped conductances that are contributing to photocurrents, however given that some cells exhibited control-like photocurrent amplitudes in MFA while others exhibited a significant decrease, we conclude that the primary effect of MFA was to block gap junction coupling. These results indicate that ipRGC photocurrents are readily transmitted through gap junctions. Therefore, the light response of an ipRGC integrates an intrinsic photocurrent with an extrinsic component from pre-junctional ipRGCs.

To characterize the impact of ipRGC gap junction networks on the overall light response of the developing retina, we used calcium imaging to quantify the number of light-responsive cells after blocking gap junctions. Application of MFA led to a marked reduction in the number of light-responsive cells (Figure 8A-C; control/control ratio = 1.06 ± 0.17, n = 11 retinas; MFA/control = 0.25 ± 0.14, n = 9). Importantly, several cells that maintained their light response did not exhibit a decreased response amplitude (Figure 8D, n = 5 retinas, 101 cells), thus the loss of light-evoked calcium transients cannot be explained by an off-target effect of MFA on the intrinsic light response or on voltage-gated calcium channels that underlie the calcium transient (Bramley et al., 2011; Vessey et al., 2004). Note that these data cannot be directly compared to amplitude of photocurrents described above (Figure 7) since there are not within-cell comparisons of the effect of MFA on photocurrent amplitudes. In fact, there were many ipRGCs that exhibited strong photocurrents in the presence of MFA (Figure 7E). Together these data indicate that during development ipRGC gap junction networks provide a significant contribution to both the single-cell and the whole-retina light response.

Discussion

In this study we demonstrate that cholinergic retinal waves regulate the early light response of the developing retina by modulating ipRGC gap junction networks. First, we show that acutely blocking cholinergic waves produces a marked increase in the number of light-responsive cells due to an increase in ipRGC gap junction coupling. Second, we provide evidence for a putative mechanism in which waves drive phasic release of dopamine that in turn regulates the extent of ipRGC gap junction coupling. Third, we demonstrate that ipRGC gap junction networks are active in the presence of cholinergic waves and contribute to the photocurrents of individual cells and to the overall light response of the developing retina. These findings directly demonstrate that ipRGCs connect to other neurons within the retina during development and that they do this via gap junctions rather than chemical synapses, consistent with a previous study (Sekaran et al., 2005). Furthermore they provide insight into mechanisms of activity-dependent modulation of gap junction networks.

IpRGC gap junction networks are regulated by cholinergic waves

Previous studies have demonstrated that in the absence of cholinergic waves, an alternative wave-generating circuit that depends on gap junctions emerges (Anishchenko and Feller, 2009; Kirkby and Feller, 2013; Stacy et al., 2005; Stafford et al., 2009; Sun et al., 2008). Here we have provided mechanistic insight into this network plasticity. First, we have demonstrated that ipRGCs are tracer coupled and electrically coupled to other ipRGCs and to non-ipRGCs (Figures 2-4). Such an intra-retinal microcircuit offers a pathway by which a projection neuron can feed back and affect the retinal network. This type of circuit has been shown in adult retina, with a growing body of literature indicating that ipRGCs not only signal to downstream brain targets but also exert widespread intra-retinal influence (Joo et al., 2013; Müller et al., 2010; Reifler et al., 2015; Zhang et al., 2012; 2008). Second, we have shown that blocking cholinergic waves during development increases the extent of both tracer and electrical coupling from ipRGCs to other retinal neurons, implying that waves suppress ipRGC gap junction networks. Hence, the regulation of gap junction networks by cholinergic retinal waves determines the extent and reach of ipRGC-dependent light responses within the retina.

Wave-evoked dopamine release modulates ipRGC gap junctions

We previously hypothesized that high dopamine signaling may function to suppress gap junction networks during cholinergic waves (Kirkby and Feller, 2013). Here we show that dopamine is indeed released during waves, thus providing mechanistic insight into this network plasticity (Figure 5). Similar to the effect of blocking waves, blocking dopaminergic signaling through D1Rs, but not D2Rs, also increases the number of light responsive-cells (Figures 6). These results suggest that D1R signaling suppresses ipRGC gap junction coupling. Thus we propose a putative mechanism where spontaneous cholinergic waves evoke dopamine release that reduces ipRGC gap junction coupling.

Although dopamine is released episodically, we speculate that it provides a tonic modulation of gap junctions. This is consistent with our observation that it takes 60 minutes of wave blockade for gap junction coupling to increase. Though D1 receptors are low affinity and therefore only

respond to high concentrations of dopamine (Dreyer et al., 2010), the resulting second messenger cascade and resulting phosphorylation of connexins are likely to integrate this signal. Studies conducted in heterologous expression systems indicate that PKA modulation of gap junctions occurs on the time scale of several minutes (H. Y. Wang et al., 2015), i.e. several waves.

The model emerging from the present study is that retinal waves suppress the spread of light-evoked intra-retinal signals from ipRGCs by activating dopaminergic amacrine cells to stimulate release of dopamine, which, acting via D1 receptors, reduces the gap junctional coupling of ipRGCs. This finding is consistent with a previous circuit model proposed for the "recovered waves" observed in a knockout mouse lacking the β2-subunit of nAChRs (Kirkby and Feller, 2013, Figure 6). Recovered waves are mediated by gap junction coupling, their frequency is increased by light stimulation, increased by D1 receptor antagonists and reduced by D2 receptor antagonists. In the proposed circuit model for recovered waves, there is an increase in ipRGC coupling to a yet to be identified neuron (pictured as an amacrine cell in Figure 6 of that study) which in turn increases coupling to other RGCs in a manner dependent on the balance of opposing effects of D1 and D2 receptors (Kothmann et al., 2009). In the presence of waves there is high dopamine release. This favors activation of D1 receptors, which are of low affinity and more sensitive to phasic changes in DA levels, thus suppressing gap junction conductance. In the absence of waves there is low dopamine. This favors activation of D2 receptors, which are of high affinity and more sensitive to tonic DA levels, thus increasing gap junction conductance.

The data presented here is consistent with this model. First, in response to wave blockade, we observed an increase in coupling to a small–soma cells in the ganglion cell layer, which are likely to be an amacrine cell type, in a manner dependent on activation of D1 receptors. However, we did not observe a sensitivity of coupling to D2 receptor antagonists. Furthermore, we did not see the occurrence of recovered waves. Hence, prolonged blockade of retinal waves such as that in the β2-nAChR knockout mouse might be necessary for the up-regulation of the D2R in this intervening amacrine cell to mediate the recovered waves.

How waves stimulate dopamine release remains to be elucidated. Two possibilities are that DACs are directly depolarized by nAChR activation, or that they are indirectly activated via ipRGCs that form glutamatergic synapses with DACs (Zhang et al., 2012; 2008). Our findings are inconsistent with the latter, since blocking glutamatergic transmission did not increase the number of light-responsive cells (Figure 6B), thus indicating that the extent of ipRGC gap junction coupling is not modulated by glutamatergic-dependent release of dopamine. Elucidating the mechanisms that mediate the interplay between chemical and electrical neural networks will require future studies that explore how signaling pathways activated by D1Rs produce changes in gap junctional conductance (O'Brien, 2014; Pereda, 2014).

Gap junction networks shape the light response of the retina in the presence of wave-evoked dopamine release

This study and previous studies have indicated that gap junctions are suppressed during retinal waves (Akrouh and Kerschensteiner, 2013; Stacy et al., 2005). However we find that even in the presence of waves, ipRGC gap junction networks continue to shape the light response of the retina. Our results indicate that ipRGCs in the developing retina form a syncytium that ensures

the depolarization of one ipRGC will contribute to the depolarization of neighboring ipRGCs (Figure 3). These findings are consistent with previous studies of developing ipRGCs where it was demonstrated that gap junction blockers decreased cell capacitance (Schmidt et al., 2008) and the number of light responsive cells in the adult (Sekaran et al., 2003) and during development (Sekaran et al., 2005). Indeed, previous studies estimated that at P4-P5 only 56% of light responsive cells were ipRGCs since the rest lost their light response in the presence of the gap junction blocker carbenoxolone (CBX) (Sekaran et al., 2005). Subsequent studies demonstrated that CBX has off-target effects that blocks light-evoked $[Ca^{2+}]_i$ rise in isolated ipRGCs (Bramley et al., 2011), though the concentrations of carbenoxolone used in the developing retina (10 μM) appeared to show weaker off-target effects. Furthermore, multielectrode array recordings of ipRGC activity in the first postnatal week indicated that 100 μM CBX did not decrease the correlated firing between ipRGCs indicating that either the coupling was not directly between ipRGCs or that CBX was not impacting functional coupling (Tu et al., 2005). Here we found that the gap junction blocker MFA does not affect the amplitude of light-evoked calcium transients in a subset of ipRGCs, indicating that MFA might not interfere with ipRGC calcium influx (Figure 8).

Since gap junctions act as a low pass filter, the contribution of light-evoked currents from neighboring ipRGCs is likely dominated by the slow depolarization evoked by photoactivation of conductances rather than the small fast depolarizations induced by spikelets (Figure 7). Indeed, blocking gap junction networks significantly decreases both the photocurrent amplitudes of ipRGCs and the overall number of light sensitive cells in the retina (Figure 7-8). This scenario sharply contrasts with the function of coupling recently described for direction selective ganglion cells (Trenholm et al., 2013b; 2013a). For those cells, gap junction coupling combines with local synaptic input to generate correlated dendritic spikes that contribute to direction coding (Trenholm et al., 2014). However for ipRGCs, coupling of photocurrents leads to more efficient detection and propagation of light information (Figure 7 and 8), and thus might hold implications for pre-vision light-dependent developmental functions such as the development of retinal vasculature (Rao et al., 2013) and of light avoidance behaviors that are thought to contribute to pup survival (Delwig et al., 2012; Johnson et al., 2010).

In summary, our results show that during development, ipRGCs form extensive gap junction microcircuits that shape the early retinal light response. Retinal waves exert a far-reaching, neuromodulatory influence on these circuits via dopaminergic modulation of gap junctions, thus potentially impacting the processing of early visual input. It is likely that this type of wave-dependent, dopaminergic modulation also impacts the development and fine-tuning of other gap junction networks in the immature retina.

References

Ackman, J.B., Burbridge, T.J., Crair, M.C., 2012. Retinal waves coordinate patterned activity throughout the developing visual system. Nature 490, 219–225. doi:10.1038/nature11529

Ackman, J.B., Crair, M.C., 2014. Role of emergent neural activity in visual map development. Curr. Opin. Neurobiol. 24, 166–175. doi:10.1016/j.conb.2013.11.011

Akrouh, A., Kerschensteiner, D., 2013. Intersecting circuits generate precisely patterned retinal waves. Neuron 79, 322–334. doi:10.1016/j.neuron.2013.05.012

Anishchenko, A., Feller, M.B., 2009. Go with the flow -- but only in one direction. Neuron 64, 152–154. doi:10.1016/j.neuron.2009.10.009

Bansal, A., Singer, J.H., Hwang, B.J., Xu, W., Beaudet, A., Feller, M.B., 2000. Mice lacking specific nicotinic acetylcholine receptor subunits exhibit dramatically altered spontaneous activity patterns and reveal a limited role for retinal waves in forming ON and OFF circuits in the inner retina. J. Neurosci. 20, 7672–7681.

Berson, D.M., Dunn, F.A., Takao, M., 2002. Phototransduction by retinal ganglion cells that set the circadian clock. Science 295, 1070–1073. doi:10.1126/science.1067262

Blankenship, A.G., Feller, M.B., 2010. Mechanisms underlying spontaneous patterned activity in developing neural circuits. Nat. Rev. Neurosci. 11, 18–29. Epub 2009 Dec 2. doi:10.1038/nrn2759

Blankenship, A.G., Ford, K.J., Johnson, J., Seal, R.P., Edwards, R.H., Copenhagen, D.R., Feller, M.B., 2009. Synaptic and extrasynaptic factors governing glutamatergic retinal waves. Neuron 62, 230–241. doi:10.1016/j.neuron.2009.03.015

Bloomfield, S.A., Völgyi, B.E.L., 2009. The diverse functional roles and regulation of neuronal gap junctions in the retina. Nat. Rev. Neurosci. 10, 495–506. doi:10.1038/nrn2636

Bramley, J.R., Wiles, E.M., Sollars, P.J., Pickard, G.E., 2011. Carbenoxolone blocks the light-evoked rise in intracellular calcium in isolated melanopsin ganglion cell photoreceptors. PLoS ONE 6, e22721. doi:10.1371/journal.pone.0022721

Brivanlou, I.H., Warland, D.K., Meister, M., 1998. Mechanisms of concerted firing among retinal ganglion cells. Neuron 20, 527–539.

Chen, S.-K., Badea, T.C., Hattar, S., 2011. Photoentrainment and pupillary light reflex are mediated by distinct populations of ipRGCs. Nature 476, 92–95. doi:10.1038/nature10206

Delwig, A., Logan, A.M., Copenhagen, D.R., Ahn, A.H., 2012. Light evokes melanopsin-dependent vocalization and neural activation associated with aversive experience in neonatal mice. PLoS ONE 7, e43787–e43787. doi:10.1371/journal.pone.0043787

DeVries, S.H., 1999. Correlated firing in rabbit retinal ganglion cells. J. Neurophysiol. 81, 908–920.

Do, M.T.H., Yau, K.W., 2010. Intrinsically Photosensitive Retinal Ganglion Cells. Physiological Reviews 90, 1547–1581. doi:10.1152/physrev.00013.2010

Dreyer, J.K., Herrik, K.F., Berg, R.W., Hounsgaard, J.D., 2010. Influence of phasic and tonic dopamine release on receptor activation. J. Neurosci. 30, 14273–14283. doi:10.1523/JNEUROSCI.1894-10.2010

Fahrenkrug, J., Nielsen, H.S., Hannibal, J., 2004. Expression of melanopsin during development of the rat retina. Neuroreport 15, 781–784.

Ford, K.J., Feller, M.B., 2012. Assembly and disassembly of a retinal cholinergic network. Vis. Neurosci. 29, 61–71. doi:10.1017/S0952523811000216

Ford, K.J., Félix, A.L., Feller, M.B., 2012. Cellular mechanisms underlying spatiotemporal

features of cholinergic retinal waves. J. Neurosci. 32, 850–863. doi:10.1523/JNEUROSCI.5309-12.2012

Hattar, S., Lucas, R.J., Mrosovsky, N., Thompson, S., Douglas, R.H., Hankins, M.W., Lem, J., Biel, M., Hofmann, F., Foster, R.G., Yau, K.W., 2003. Melanopsin and rod-cone photoreceptive systems account for all major accessory visual functions in mice. Nature 424, 76–81. doi:10.1038/nature01761

Huberman, A.D., Feller, M.B., Chapman, B., 2008. Mechanisms Underlying Development of Visual Maps and Receptive Fields. Annu. Rev. Neurosci. 31, 479–509. doi:10.1146/annurev.neuro.31.060407.125533

Jain, V., Ravindran, E., Dhingra, N.K., 2012. Differential expression of Brn3 transcription factors in intrinsically photosensitive retinal ganglion cells in mouse. J. Comp. Neurol. 520, 742–755. doi:10.1002/cne.22765

Johnson, J., Wu, V., Donovan, M., Majumdar, S., Rentería, R.C., Porco, T., Van Gelder, R.N., Copenhagen, D.R., 2010. Melanopsin-dependent light avoidance in neonatal mice. Proc. Natl. Acad. Sci. U.S.A. 107, 17374–17378. doi:10.1073/pnas.1008533107

Joo, H.R., Peterson, B.B., Dacey, D.M., Hattar, S., Chen, S.-K., 2013. Recurrent axon collaterals of intrinsically photosensitive retinal ganglion cells. Vis. Neurosci. 30, 175–182. doi:10.1017/S0952523813000199

Kerschensteiner, D., 2013. Spontaneous Network Activity and Synaptic Development. Neuroscientist 20, 272–290. doi:10.1177/1073858413510044

Kirkby, L.A., Feller, M.B., 2013. Intrinsically photosensitive ganglion cells contribute to plasticity in retinal wave circuits. Proc. Natl. Acad. Sci. U.S.A. 110, 12090–12095. doi:10.1073/pnas.1222150110

Kirkby, L.A., Sack, G.S., Firl, A., Feller, M.B., 2013. A role for correlated spontaneous activity in the assembly of neural circuits. Neuron 80, 1129–1144. doi:10.1016/j.neuron.2013.10.030

Kothmann, W.W., Massey, S.C., O'Brien, J., 2009. Dopamine-stimulated dephosphorylation of connexin 36 mediates AII amacrine cell uncoupling. J. Neurosci. 29, 14903–14911. doi:10.1523/JNEUROSCI.3436-09.2009

Landisman, C.E., Connors, B.W., 2005. Long-term modulation of electrical synapses in the mammalian thalamus. Science (New York, NY).

Lohmann, C., Myhr, K.L., Wong, R.O.L., 2002. Transmitter-evoked local calcium release stabilizes developing dendrites. Nature 418, 177–181. doi:10.1038/nature00850

Muller, A., Joseph, V., Slesinger, P.A., Kleinfeld, D., 2014. Cell-based reporters reveal in vivo dynamics of dopamine and norepinephrine release in murine cortex. Nature methods 11, 1245–1252. doi:10.1038/nmeth.3151

Müller, L.P. de S., Do, M.T.H., Yau, K.-W., He, S., Baldridge, W.H., 2010. Tracer coupling of intrinsically photosensitive retinal ganglion cells to amacrine cells in the mouse retina. J. Comp. Neurol. 518, 4813–4824. doi:10.1002/cne.22490

Nguyen, Q.T., Schroeder, L.F., Mank, M., Muller, A., Taylor, P., Griesbeck, O., Kleinfeld, D., 2010. An in vivo biosensor for neurotransmitter release and in situ receptor activity. Nat. Neurosci. 13, 127–132. doi:10.1038/nn.2469

O'Brien, J., 2014. The ever-changing electrical synapse. Curr. Opin. Neurobiol. 29C, 64–72. doi:10.1016/j.conb.2014.05.011

Pereda, A.E., 2014. Electrical synapses and their functional interactions with chemical synapses. Nat. Rev. Neurosci. 15, 250–263. doi:10.1038/nrn3708

Rao, S., Chun, C., Fan, J., Kofron, J.M., Yang, M.B., Hegde, R.S., Ferrara, N., Copenhagen,

D.R., Lang, R.A., 2013. A direct and melanopsin-dependent fetal light response regulates mouse eye development. Nature 494, 243–246. doi:10.1038/nature11823

Reifler, A.N., Chervenak, A.P., Dolikian, M.E., Benenati, B.A., Li, B.Y., Wachter, R.D., Lynch, A.M., Demertzis, Z.D., Meyers, B.S., Abufarha, F.S., Jaeckel, E.R., Flannery, M.P., Wong, K.Y., 2015. All Spiking, Sustained ON Displaced Amacrine Cells Receive Gap-Junction Input from Melanopsin Ganglion Cells. Curr. Biol. 25, 2763–2773. doi:10.1016/j.cub.2015.09.018

Renna, J.M., Weng, S., Berson, D.M., 2011. Light acts through melanopsin to alter retinal waves and segregation of retinogeniculate afferents. Nat. Neurosci. 14, 827–829. doi:10.1038/nn.2845

Rollag, M.D., Berson, D.M., Provencio, I., 2003. Melanopsin, ganglion-cell photoreceptors, and mammalian photoentrainment. Journal of biological rhythms 18, 227–234.

Schmidt, T.M., Chen, S.-K., Hattar, S., 2011. Intrinsically photosensitive retinal ganglion cells: many subtypes, diverse functions. Trends Neurosci. 34, 572–580. doi:10.1016/j.tins.2011.07.001

Schmidt, T.M., Taniguchi, K., Kofuji, P., 2008. Intrinsic and extrinsic light responses in melanopsin-expressing ganglion cells during mouse development. J. Neurophysiol. 100, 371–384. doi:10.1152/jn.00062.2008

Sekaran, S., Foster, R.G., Lucas, R.J., Hankins, M.W., 2003. Calcium Imaging Reveals a Network of Intrinsically Light-Sensitive Inner-Retinal Neurons. Current Biology 13, 1290–1298. doi:10.1016/S0960-9822(03)00510-4

Sekaran, S., Lupi, D., Jones, S.L., Sheely, C.J., Hattar, S., Yau, K.W., Lucas, R.J., Foster, R.G., Hankins, M.W., 2005. Melanopsin-dependent photoreception provides earliest light detection in the mammalian retina. Current Biology 15, 1099–1107. doi:10.1016/j.cub.2005.05.053

Sexton, T.J., Bleckert, A., Turner, M.H., Van Gelder, R.N., 2015. Type I intrinsically photosensitive retinal ganglion cells of early post-natal development correspond to the M4 subtype. Neural Dev 10, 17. doi:10.1186/s13064-015-0042-x

Singer, J.H., Mirotznik, R.R., Feller, M.B., 2001. Potentiation of L-type calcium channels reveals nonsynaptic mechanisms that correlate spontaneous activity in the developing mammalian retina. J. Neurosci. 21, 8514–22.

Stacy, R.C., Demas, J., Burgess, R.W., Sanes, J.R., Wong, R.O.L., 2005. Disruption and Recovery of Patterned Retinal Activity in the Absence of Acetylcholine. J. Neurosci. 25, 9347–57.

Stafford, B.K., Sher, A., Litke, A.M., Feldheim, D.A., 2009. Spatial-Temporal Patterns of Retinal Waves Underlying Activity-Dependent Refinement of Retinofugal Projections. Neuron 64, 200.

Sun, C., Warland, D.K., Ballesteros, J.M., van der List, D., Chalupa, L.M., 2008. Retinal waves in mice lacking the β2 subunit of the nicotinic acetylcholine receptor. Proc. Natl. Acad. Sci. U.S.A. 105, 13638.

Trenholm, S., McLaughlin, A.J., Schwab, D.J., Awatramani, G.B., 2013a. Dynamic Tuning of Electrical and Chemical Synaptic Transmission in a Network of Motion Coding Retinal Neurons. J. Neurosci. 33, 14927–14938. doi:10.1523/JNEUROSCI.0808-13.2013

Trenholm, S., McLaughlin, A.J., Schwab, D.J., Turner, M.H., Smith, R.G., Rieke, F., Awatramani, G.B., 2014. Nonlinear dendritic integration of electrical and chemical synaptic inputs drives fine-scale correlations. Nat. Neurosci. 17, 1759–1766. doi:10.1038/nn.3851

Trenholm, S., Schwab, D.J., Balasubramanian, V., Awatramani, G.B., 2013b. Lag normalization in an electrically coupled neural network. Nat. Neurosci. 16, 154–156. doi:10.1038/nn.3308

Tu, D.C., Zhang, D., Demas, J., Slutsky, E.B., Provencio, I., Holy, T.E., Van Gelder, R.N., 2005. Physiologic diversity and development of intrinsically photosensitive retinal ganglion cells. Neuron 48, 987–999. doi:10.1016/j.neuron.2005.09.031

Valiante, T.A., Perez Velazquez, J.L., Jahromi, S.S., Carlen, P.L., 1995. Coupling potentials in CA1 neurons during calcium-free-induced field burst activity. J. Neurosci. 15, 6946–6956.

Van Hook, M.J., Wong, K.Y., Berson, D.M., 2012. Dopaminergic modulation of ganglion-cell photoreceptors in rat. Eur J Neurosci 35, 507–518. doi:10.1111/j.1460-9568.2011.07975.x

Vessey, J.P., Lalonde, M.R., Mizan, H.A., Welch, N.C., Kelly, M.E., Barnes, S., 2004. Carbenoxolone inhibition of voltage-gated Ca channels and synaptic transmission in the retina. J. Neurophysiol. 92, 1252–1256.

Wang, H.C., Bergles, D.E., 2015. Spontaneous activity in the developing auditory system. Cell Tissue Res. 361, 65–75. doi:10.1007/s00441-014-2007-5

Wang, H.Y., Lin, Y.-P., Mitchell, C.K., Ram, S., O'Brien, J., 2015. Two-color fluorescent analysis of connexin 36 turnover: relationship to functional plasticity. J. Cell. Sci. 128, 3888–3897. doi:10.1242/jcs.162586

Wenner, P., 2012. Motor Development: Activity Matters After All. Current Biology 22, R47–R48. doi:10.1016/j.cub.2011.12.008

Witkovsky, P., Veisenberger, E., Haycock, J.W., Akopian, A., Garcia-Espana, A., Meller, E., 2004. Activity-dependent phosphorylation of tyrosine hydroxylase in dopaminergic neurons of the rat retina. J. Neurosci. 24, 4242–4249. doi:10.1523/JNEUROSCI.5436-03.2004

Wong, W.T., Wong, R.O., 2001. Changing specificity of neurotransmitter regulation of rapid dendritic remodeling during synaptogenesis. Nat. Neurosci. 4, 351–2.

Yoshida, M., Feng, L., Grimbert, F., Rangarajan, K.V., Buggele, W., Copenhagen, D.R., Cang, J., Liu, X., 2011. Overexpression of neurotrophin-3 stimulates a second wave of dopaminergic amacrine cell genesis after birth in the mouse retina. J. Neurosci. 31, 12663–12673. doi:10.1523/JNEUROSCI.1100-11.2011

Zhang, D.-Q., Belenky, M.A., Sollars, P.J., Pickard, G.E., McMahon, D.G., 2012. Melanopsin mediates retrograde visual signaling in the retina. PLoS ONE 7, e42647. doi:10.1371/journal.pone.0042647

Zhang, D.-Q., Wong, K.Y., Sollars, P.J., Berson, D.M., Pickard, G.E., McMahon, D.G., 2008. Intraretinal signaling by ganglion cell photoreceptors to dopaminergic amacrine neurons. Proc. Natl. Acad. Sci. U.S.A. 105, 14181–14186. doi:10.1073/pnas.0803893105

Zhang, D.-Q., Zhou, T.-R., McMahon, D.G., 2007. Functional heterogeneity of retinal dopaminergic neurons underlying their multiple roles in vision. J. Neurosci. 27, 692–699. doi:10.1523/JNEUROSCI.4478-06.2007

Acknowledgments

We thank all members of the Feller laboratory for their comments on this manuscript. We thank Andrew Huberman and Rana El-Danaf (UCSD) for their assistance with the dye injection experiments; David Kleinfeld and Paul Slesinger (UCSD) for providing CNiFERs; and Raymond Johnson (Vanderbilt Neurochemistry Core) for performing HPLC dopamine analysis. This work was supported by the National Institute of Health grants R01EY013528, P30EY003176 (M.B.F.) and F31EY024842 (D.A.A.), and the National Science Foundation Graduate Research Fellowship Program (L.A.K. and D.A.A.).

Figure 1: Blocking retinal waves increases the number of light responsive neurons.
A. Left: Fluorescent image of a retina loaded with OGB-1 (average of 30 sequential images, baseline); Middle/Right: Heat maps of maximal ΔF/F during the first 7s of light stimulation in ACSF (control, middle) and after 60 min exposure to the nAChR antagonist DHβE (8μM, right). Numbers indicate example light-responsive cells shown in **C**. **B.** Simultaneous calcium imaging and cell-attached recording from a light-responsive cell indicate that calcium imaging signal corresponds to an increase in firing rate. Top: Cell-attached recording shows cell's response to light stimulation (indicated by blue bar). Middle: Firing rate of the same cell. Bottom: Fractional change of OGB-1 fluorescence (ΔF/F) in of the cell. **C.** Time course of ΔF/F for the 10 cells of the ganglion cell layer indicated in **A** in response to light stimulation by the excitation light used for imaging. Traces of each of the 10 cells are shown in control (left) and after 60 min exposure to DHβE. **D.** Number of light-responsive cells after a manipulation given as a fraction of the number of light-responsive cells before the manipulation for three conditions: 60 min in ACSF (control/control); 60 min exposure to DHβE (DHβE/control); after DHβE application, 10 min exposure to a cocktail containing DHβE (8 μM), glutamate receptor antagonists DNQX (20 μM) and AP5 (50 μM), GABA-A receptor antagonist gabazine (5 μM), and glycine receptor antagonist strychnine (4 μM) (synaptic block/control). Lines connect data points from the same retina. Dashed red line indicates the mean of control/control. Error bars represent S.D. around the mean. $*p < 0.05$ compared to ratio of 1, one-tailed student's t-test. **E.** Pseudo-colored images of light-responsive cells identified using calcium imaging, injected with the fluorescent molecule Alexa-594 (magenta), and stained with an anti-melanopsin antibody (green). Left: Example cell in control conditions where 12/13 light-responsive cells were positive for melanopsin. Right: Example cell that gained light response after DHβE exposure where 1/5 cells were positive for melanopsin.

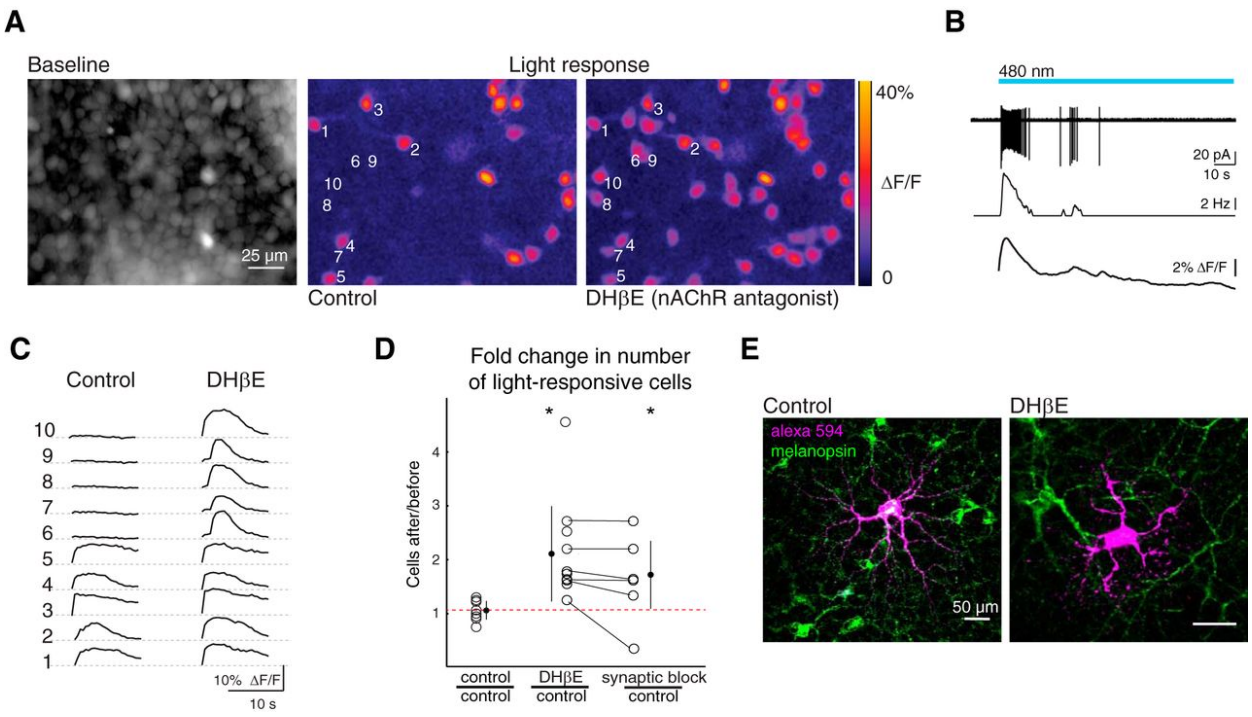
A
Baseline
Light response
25 µm
40%
ΔF/F
0
Control
DHβE (nAChR antagonist)
B
480 nm
20 pA
10 s
2 Hz
2% ΔF/F
C
Control
DHβE
10% ΔF/F
10 s
D
Fold change in number of light-responsive cells
Cells after/before
control
control
DHβE
control
synaptic block
control
E
Control
DHβE
alexa 594
melanopsin
50 µm

Figure 2: ipRGCs form intra-retinal tracer-coupled networks.
A. Fluorescent image of neurobiotin-filled ipRGC targeted in Opn4-EGFP mouse, stained with a fluorescent streptavidin conjugate (left top), and immunostained for GFP (left bottom). Arrows indicate cells with coincident Nb and anti-GFP signals. Inset shows enlargement of one of the cells with coincident signals (yellow box) for the different color channels. Merged neurobiotin (Nb, magenta) and anti-GFP (green) images (right) show coincident Nb and anti-GFP signals (Nb + GFP), pseudocolored white for visualization. **B**. Fluorescent image of neurobiotin-filled ipRGC targeted in Opn4-EGFP mouse after 60 min exposure to DHβE (8 μM). Details as in part A. **C.** Total number of coupled cells (Nb) and coupled GFP+ cells (Nb + GFP) in control (ACSF) and after blocking retinal waves (DHβE, 60 min). Lines connect data points from the same Nb-filled ipRGC. Error bars represent S.D. around the mean. $*p < 0.05$, two-tailed student's t-test ($Nb_{control}$ vs. $Nb_{DH\beta E}$, $Nb+GFP_{control}$ vs. $NB+GFP_{DH\beta E}$). **D**. Histogram distribution of distances of all Nb positive cells to the soma of injected cell in control (top) and after 60 minute exposure to DHβE (bottom). **E**. Histogram distribution of distances of all Nb positive cells to the soma of the injected cell that were either GFP- (top) or GFP+ (bottom). Note coupled cells in absence and presence of DHβE were included. **F.** Top: Fluorescent images of neurobiotin-filled ipRGCs (magenta) co-labeled (green) with antibodies against either Brn3b (i), Brn3a (ii), GABA (iii), or tyrosine hydroxylase (TH, iv). White indicates cells with coincident signals (Nb + marker). Bottom: Morphological reconstructions of cells (top) fixed to the same scale (scale bar = 30 μm). **G.** Number of Nb + marker-labeled cells as a percentage of the total number of Nb-labeled cells, for the markers in **C**. Error bars represent S.D. around the mean.

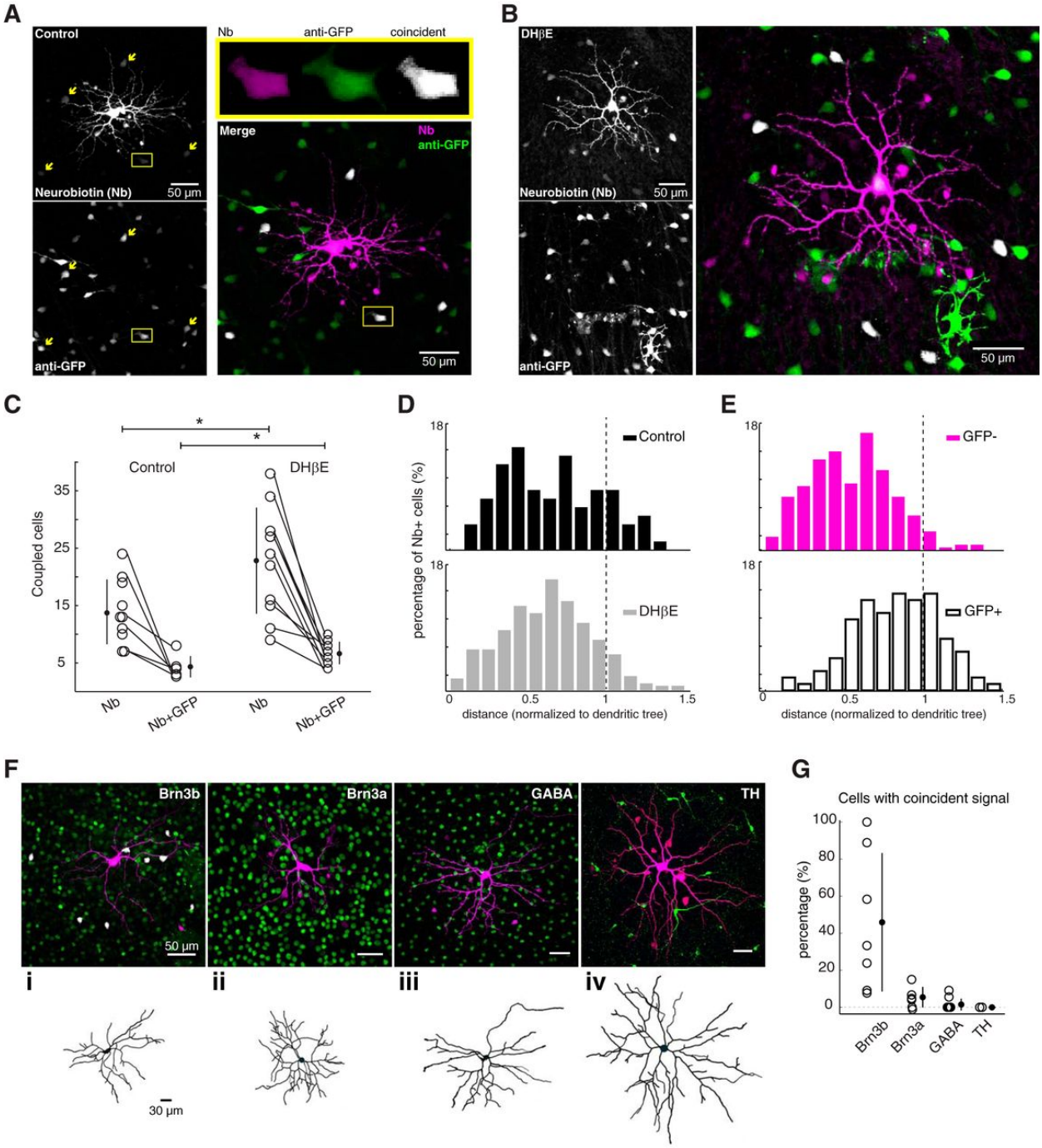
A
Control
Neurobiotin (Nb)
50 µm
anti-GFP
Nb
anti-GFP
coincident
Merge
Nb
anti-GFP
50 µm
B
DHβE
Neurobiotin (Nb)
50 µm
anti-GFP
50 µm
C
Control
DHβE
Coupled cells
35
25
15
5
Nb
Nb+GFP
Nb
Nb+GFP
D
Control
DHβE
percentage of Nb+ cells (%)
18
18
0
0.5
1
1.5
distance (normalized to dendritic tree)
E
GFP-
GFP+
18
18
0
0.5
1
1.5
distance (normalized to dendritic tree)
F
Brn3b
Brn3a
GABA
TH
50 µm
i
ii
iii
iv
30 µm
G
Cells with coincident signal
percentage (%)
100
80
60
40
20
0
Brn3b
Brn3a
GABA
TH

Figure 3: ipRGCs form functional intra-retinal gap junction networks.
A. Left: DIC image shows recording electrode targeting an ipRGC identified by light stimulation as in Figure 1. Right: Fluorescent image of same retina loaded with calcium indicator OGB-1. Cells indicated with blue and red dots correspond to traces shown in **B**. Recordings were conducted in DNQX, DHβE, DNQX, AP5, gabazine, and strychnine to isolate electrical synapses. **B.** Top: Voltage clamp protocol for simultaneous imaging and whole-cell voltage clamp: 500 ms voltage steps from -60 to 0 mV were injected into the recorded ipRGC (indicated by *). Bottom: Traces from cells indicated in **A** that either displayed responses (blue) or failed to display responses (red) when the voltage-clamped ipRGC (*) was depolarized. Blue line indicates excitation light for calcium imaging. **C.** Number of cells in which both voltage steps evoked calcium transients for separated control and DHβE (60 min) groups. $*p < 0.05$, two-tailed student's t-test. **D.** Percentage of cells with voltage-clamp-evoked responses that also showed light-evoked calcium transients for control and DHβE. **E.** Amplitudes (DF/F) of the calcium transients evoked by depolarizing steps for separated control and DHβE groups.
All error bars represent S.D. around the mean.

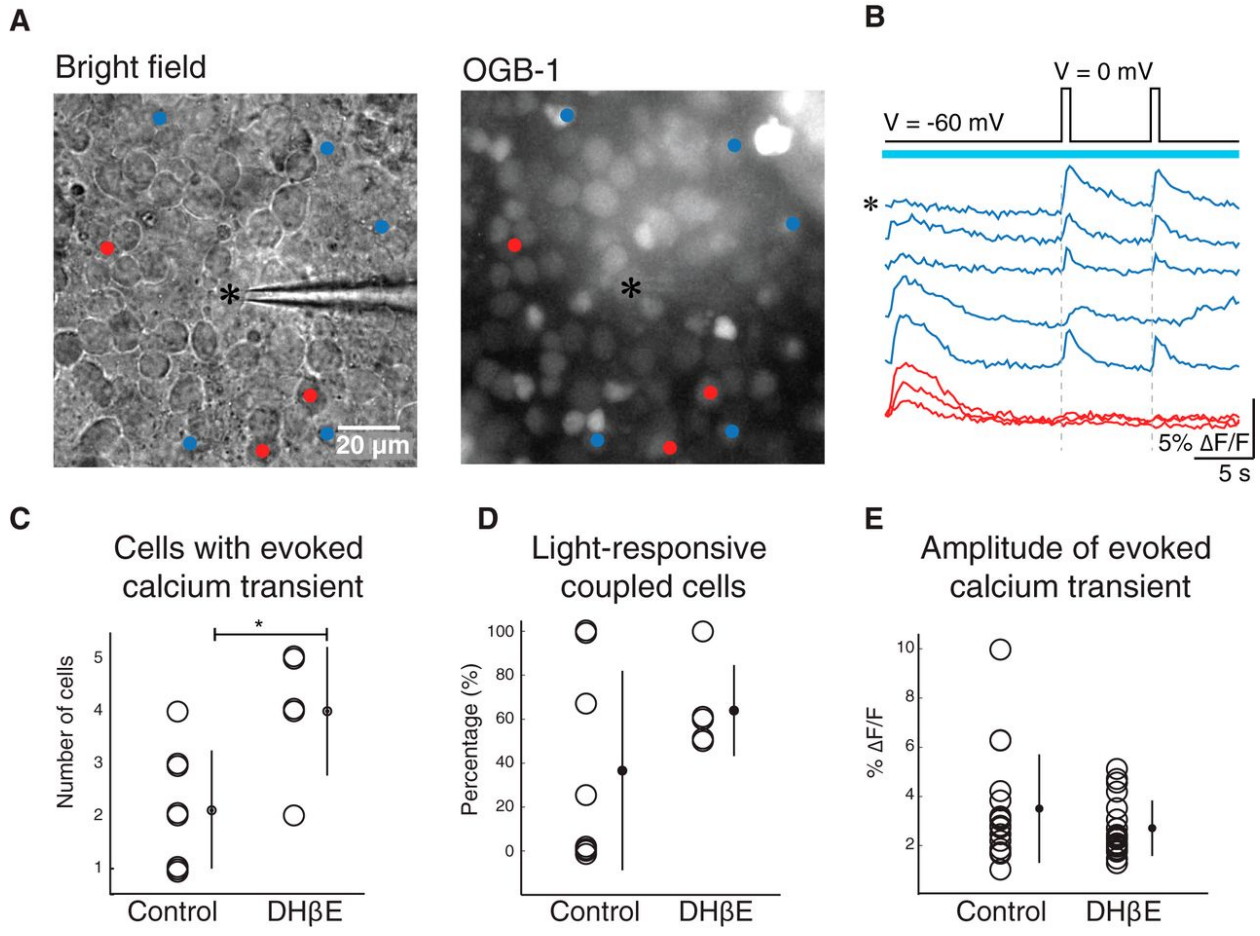
A
Bright field
OGB-1
20 µm
B
V = 0 mV
V = -60 mV
5% ΔF/F
5 s
C
Cells with evoked calcium transient
Number of cells
Control
DHβE
D
Light-responsive coupled cells
Percentage (%)
Control
DHβE
E
Amplitude of evoked calcium transient
% ΔF/F
Control
DHβE

Figure 4: Spiking activity of ipRGCs indicates gap junction coupling before and after blocking retinal waves.
A. Raster plots show spike times of units isolated using MEA recordings following light stimulation in ACSF (control, left) and DHβE (right). **B.** Example of single unit spike train (bottom) and instantaneous firing rate (top) during light stimulation in control. Red points mark beginning and end of light-evoked activity, blue point marks peak firing rate. The two other depicted bursts of activity (one before and one during light stimulation) correspond to retinal waves. **C.** Cumulative probability distributions of the light response parameters of peak firing rate and latency-to-peak firing rate before (control, black) and after cholinergic block (DHβE, original (red) and new (blue) light responsive cells). **D.** Irradiance-response curves of GFP-expressing ipRGCs in Opn4-EGFP mouse line in ACSF (control, gray) and DHβE (black). Error bars represent S.D. around the mean. **E.** Top: Raster plots show spike times of sample light-responsive units (their locations on the MEA are indicated in diagram on right) in ACSF (control, left) and DHβE (middle). Bottom: Cross correlograms (CCGs) for pairs of the units shown in raster plot for control and DHβE.
All blue bars represent 480 nm light stimulation.

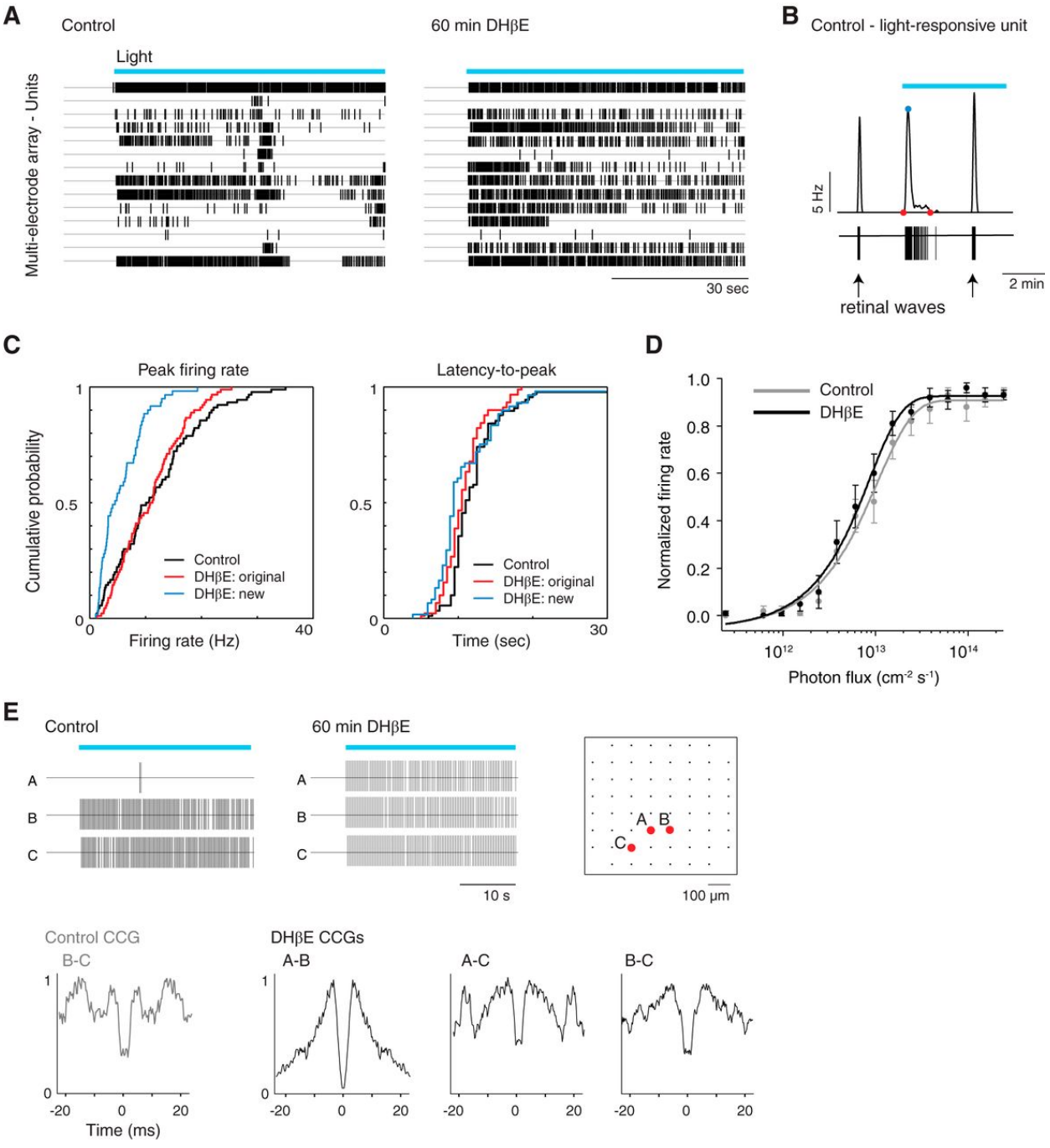
A
Control
60 min DHβE
Light
Multi-electrode array - Units
30 sec
B
Control - light-responsive unit
5 Hz
2 min
retinal waves
C
Peak firing rate
Latency-to-peak
Cumulative probability
Control
DHβE: original
DHβE: new
Firing rate (Hz)
Time (sec)
D
Control
DHβE
Normalized firing rate
Photon flux (cm-2 s-1)
E
Control
60 min DHβE
A
B
C
10 s
A'
B'
100 µm
Control CCG
B-C
DHβE CCGs
A-B
A-C
B-C
Time (ms)

Figure 5: Retinal waves stimulate diffuse dopamine release.
A. Left: Fluorescent image of dopaminergic amacrine cells labeled by anti-TH in a P4 whole mount retina. Right: Concentrations of dopamine (DA) and its primary metabolite DOPAC in P4–P6 retinas detected using HPLC. Each data point corresponds to a different retina. **B.** Left: Schematic of CNiFER experimental setup: CNiFER cell deposited on surface of inner limiting membrane and simultaneous patch-clamp recording from nearby RGC (refer to Methods. TN-XXL: calcium-dependent FRET sensor; D2R: type-2 dopamine receptor). Right: Fluorescent and DIC images of CNiFERs on surface of whole mount retina. **C.** Example traces of CNiFER imaging and simultaneous voltage-clamp recording from an RGC showing three consecutive FRET events: FRET ratio (black, YFP/CFP); current trace (gray) from nearby RGC. Large EPSCs in RGC trace are associated with retinal waves (arrows). **D.** Example traces of CNiFER imaging and simultaneous voltage-clamp recording from an RGC where retinal wave is not associated with a FRET event. Details as in **C**. **E.** Times of a transient FRET increase after the closest wave-associated EPSC for observed data (black) and for time shuffled data (red, see Methods). **F.** Magnitude of a FRET response when subsequent wave is (as in **C**) vs. is not (as in **D**) associated with a FRET event. When the FRET event is absent for a wave, the FRET event evoked by the previous wave is large in magnitude. $*p < 0.05$, two-tailed student's t-test. **G.** Example FRET traces of CNiFER responses from four different cells in the same field of view to a 0.5 s puff of high-potassium solution (K puff) applied to the inner nuclear layer to stimulate dopaminergic amacrine cells. Response to the second K puff is not detected if the first FRET increase is greater than approximately 10%. **H.** FRET increases of transient events recorded in ACSF (control) and DHβE. $*p < 0.05$, two-tailed student's t-test. **I.** Dose-response curve of DA-CNiFERs deposited on the inner limiting membrane surface to nearby DA puffs of known concentration. Inset shows example responses. Gray region denotes range of magnitudes of spontaneous FRET increases observed in our recordings.
All error bars represent S.D. around the mean.

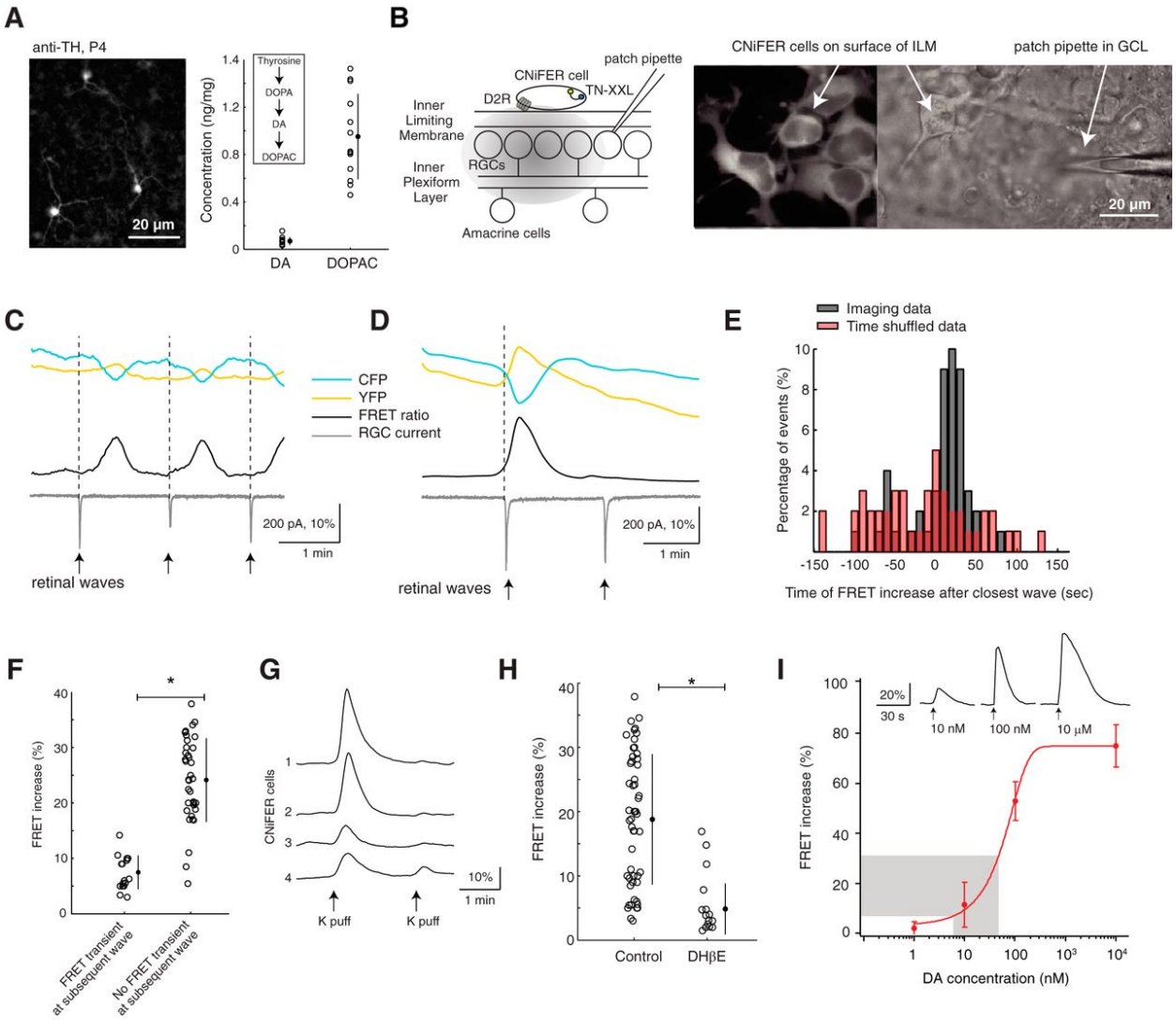
A
anti-TH, P4
20 µm
Concentration (ng/mg)
Thyrosine
DOPA
DA
DOPAC
DA
DOPAC
B
patch pipette
CNiFER cell
TN-XXL
D2R
Inner Limiting Membrane
RGCs
Inner Plexiform Layer
Amacrine cells
CNiFER cells on surface of ILM
patch pipette in GCL
20 µm
C
CFP
YFP
FRET ratio
RGC current
200 pA, 10%
1 min
retinal waves
D
200 pA, 10%
1 min
retinal waves
E
Imaging data
Time shuffled data
Percentage of events (%)
Time of FRET increase after closest wave (sec)
F
FRET increase (%)
FRET transient at subsequent wave
No FRET transient at subsequent wave
G
CNiFER cells
K puff
K puff
10%
1 min
H
FRET increase (%)
Control
DHβE
I
20%
30 s
10 nM
100 nM
10 µM
FRET increase (%)
DA concentration (nM)

Figure 6: Reduced dopamine signaling increases the number of light responsive neurons.
A. Left: Fluorescent image of a retina loaded with OGB-1 (average of 30 sequential images); Middle/Right: Heat maps of maximal ΔF/F during the first 7s of light stimulation in control conditions (middle) and after 30 min bath application of the D1R antagonist SCH23390 (SCH, 10μM, right). **B.** Number of light-responsive cells after a manipulation given as a fraction of the number of light-responsive cells before the manipulation for eight conditions: 60 min in ACSF (control/control); 60 min exposure to DHβE (DHβE/control); 30 min exposure to SCH (SCH/control) and 20 min washout of SCH (wash/control); 30 min exposure to D2R antagonist raclopride (8 μM, raclopride/control) and 20 min washout of raclopride (wash/control); 60 min exposure to DNQX (20 μM, DNQX/control) and 20 min washout of DNQX (wash/control). Lines connect data points from the same retina. Dashed red line indicates the mean of control/control. Error bars represent S.D. around the mean. $*p < 0.05$, $**p < 0.01$ compared to ratio of 1, one-tailed student's t-test.

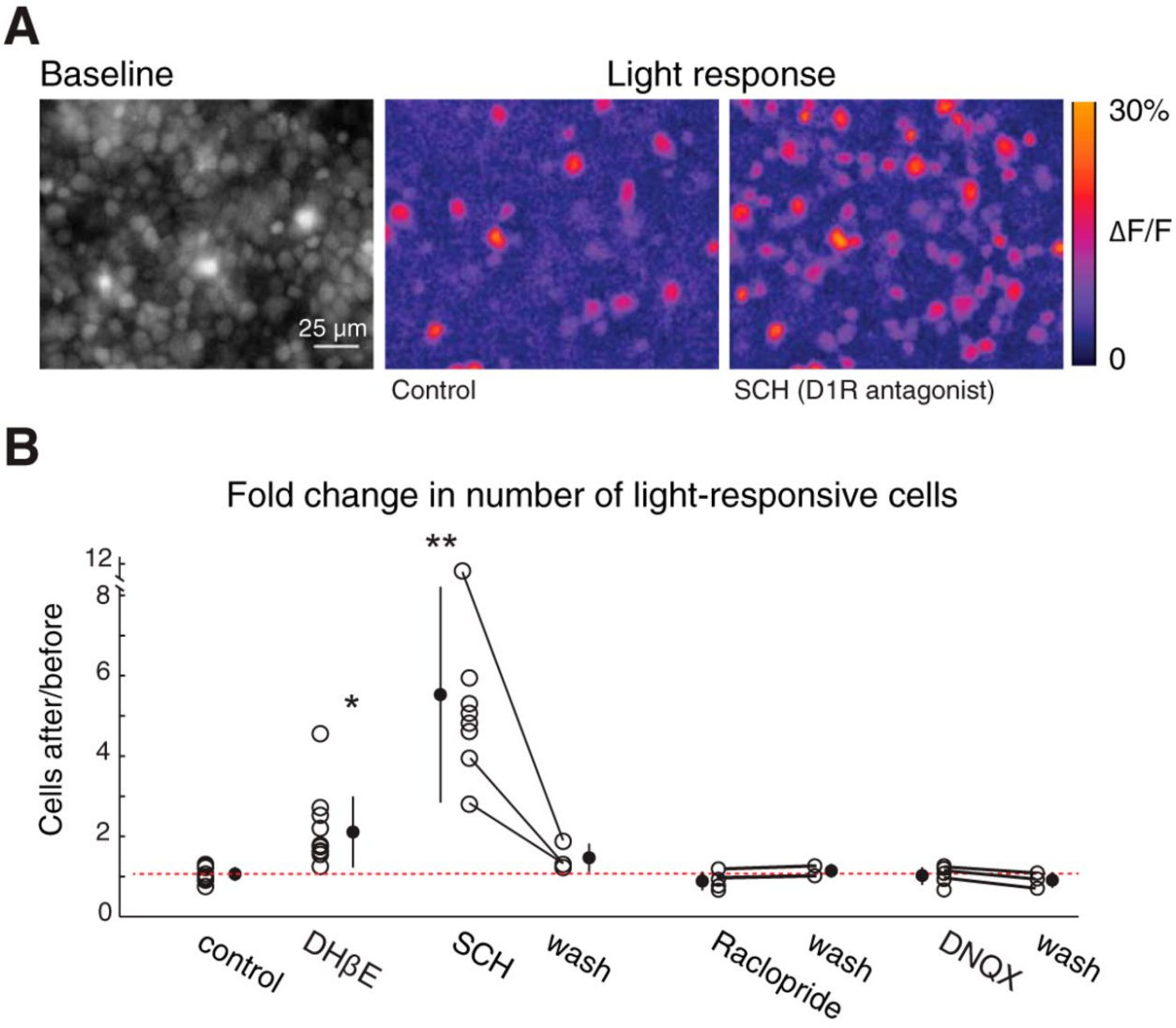
A
Baseline
Light response
25 µm
30%
ΔF/F
0
Control
SCH (D1R antagonist)
B
Fold change in number of light-responsive cells
Cells after/before
12
8
6
4
2
0
**
*
control
DHβE
SCH
wash
Raclopride
wash
DNQX
wash

Figure 7: Gap junction networks contribute to ipRGC photocurrents.
A-B. Whole-cell voltage clamp recording of ipRGC during 3s blue light illumination in ACSF (control, black) and 1μM TTX (red). In **B,** shaded region is expanded (top) and 15 sample spikelets are displayed (bottom). **C**. Distribution of inter-spike intervals (ISIs) for spikelets during 10s following light onset (black) and of ISIs for spikes recorded in cell-attached configuration (gray). **D**. Top: Diagram of setup illustrates that wide-field illumination stimulates multiple gap junction coupled ipRGCs in the field of view. Bottom: Example traces of ipRGC photocurrents in response to 3s blue light illumination in control and in the gap junction blocker meclofenamic acid (MFA, 50μM, 30 minutes). **E**. Peak photocurrent amplitude for control and MFA groups. Error bars represent S.D. around the mean. $*p < 0.05$, two-tailed student's t-test. Gray circles were considered a different cell population and thus were not included in the analysis.

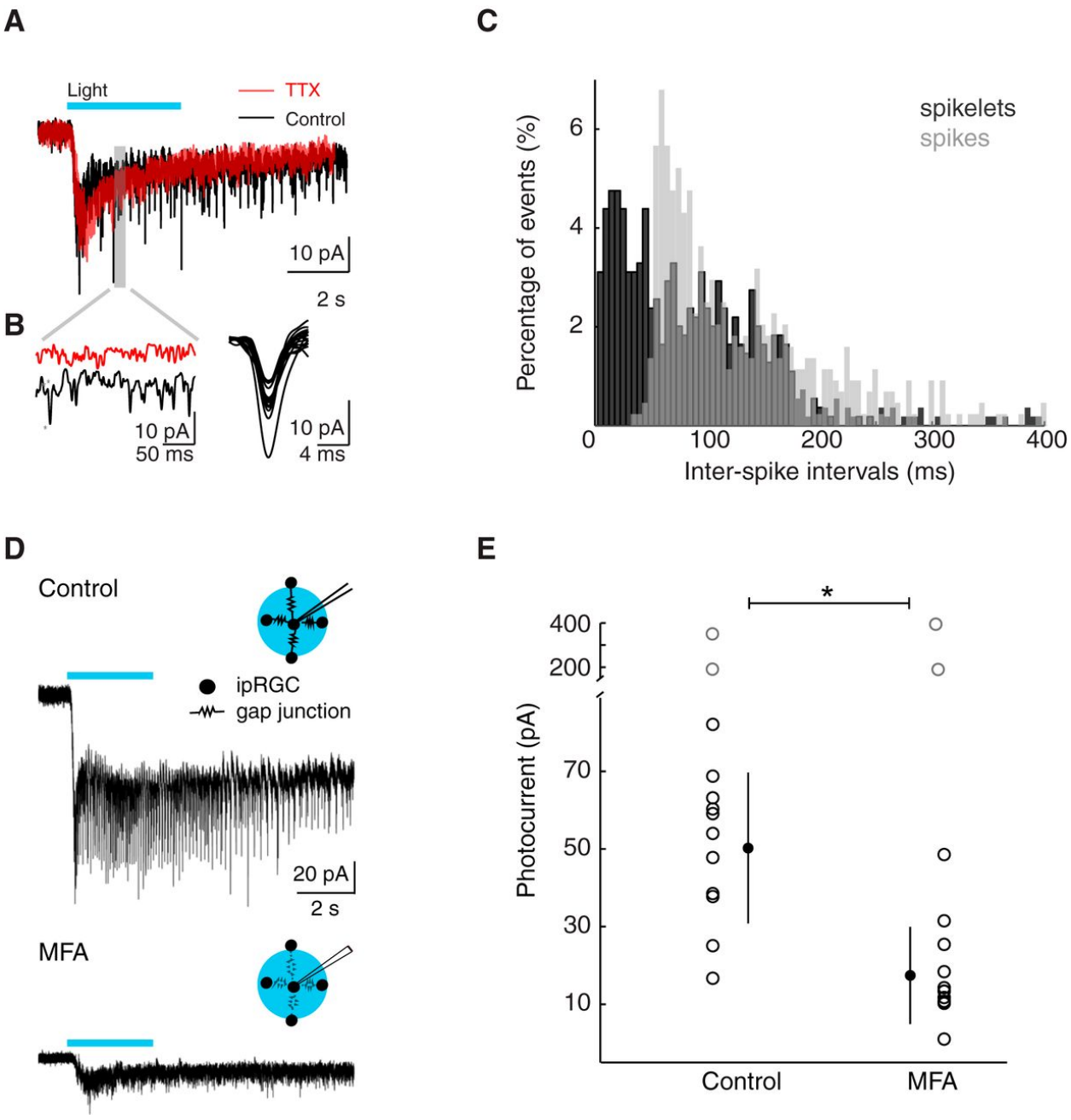
A
Light
TTX
Control
10 pA
2 s
B
10 pA
50 ms
10 pA
4 ms
C
spikelets
spikes
Percentage of events (%)
6
4
2
0
100
200
300
400
Inter-spike intervals (ms)
D
Control
ipRGC
gap junction
20 pA
2 s
MFA
E
*
400
200
70
50
30
10
Photocurrent (pA)
Control
MFA

Figure 8: Gap junction networks shape the light response of the developing retina.
A. Left: Fluorescent image of a retina loaded with OGB-1 (average of 30 sequential images); Middle/Right: Heat maps of maximal ΔF/F during the first 7s of light stimulation in control conditions (middle) and after 30 min bath application of the gap junction blocker MFA (50μM, right). Numbers indicate example cells shown in **B**. **B.** Time course of ΔF/F for the 10 cells of the ganglion cell layer indicated in **A** in response to light stimulation. Left traces are in control ACSF and right traces are after 30 min of MFA exposure (50 μM). **C.** Number of light-responsive cells after a manipulation given as a fraction of the number of light-responsive cells before the manipulation for three conditions: 60 min in ACSF (control/control); 30 min exposure to MFA (MFA/control); and 20 min washout of MFA (wash/control). Lines connect data points from the same retina. Dashed red line indicates the mean of control/control. Error bars represent S.D. around the mean. $^{**}p < 0.01$ compared to ratio of 1, one-sample student's t-test. **D.** Amplitude of light-evoked calcium transients for individual cells in control conditions and after application of MFA for 30 minutes (5 retinas, 101 cells). Black lines indicate cells that exhibited little or no change in their response amplitude.

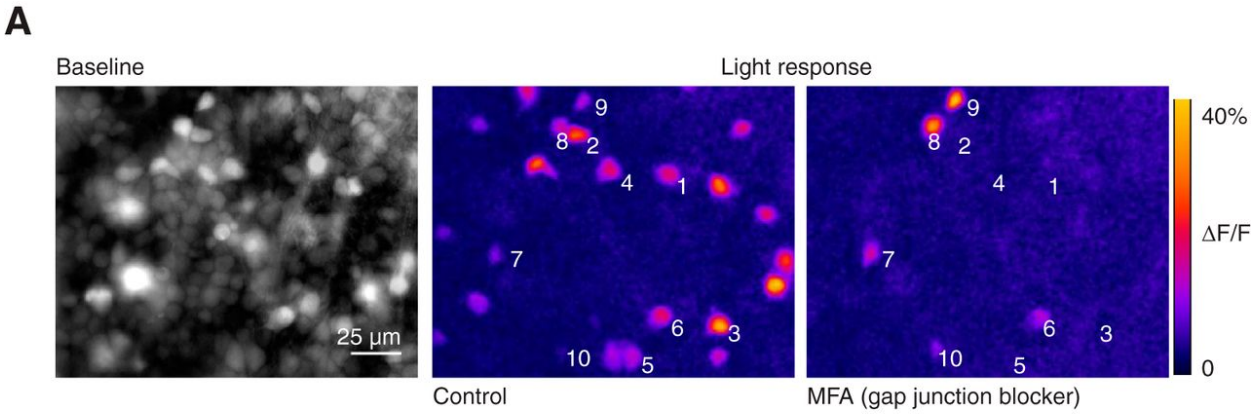
A
Baseline
Light response
25 µm
40%
ΔF/F
0
Control
MFA (gap junction blocker)

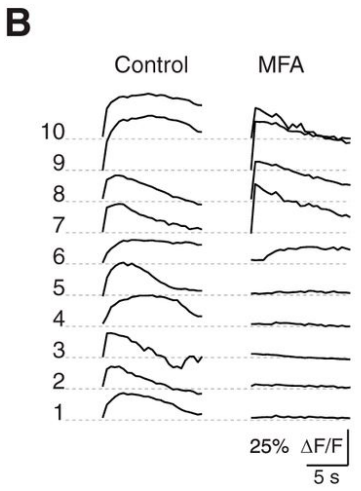
B
Control
MFA
25% ΔF/F
5 s

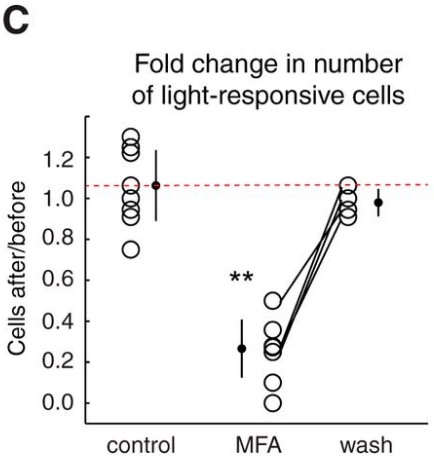
C
Fold change in number of light-responsive cells
Cells after/before
control
MFA
wash

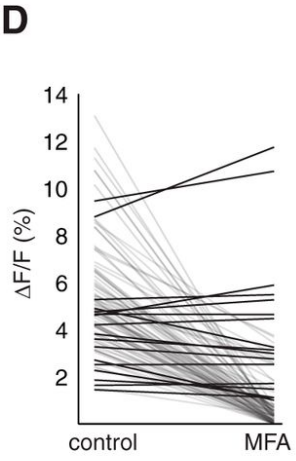
D
ΔF/F (%)
control
MFA

IV. Response decay kinetics of developing ipRGCs as a potential identifier of different cell types

Abstract

Early in development intrinsically photosensitive retinal ganglion cells (ipRGCs) provide the first and only source of light detection in the retina. The characteristics of multiple types of ipRGCs and their function are well understood in adult mice. On the other hand, distinction of ipRGC types and their functions in the in developing mice are not nearly as established. Here we use calcium imaging to explore whether different characteristics of the light response can be used to identify different populations of developing ipRGCs. We found that light responses exhibited broad variance in terms of amplitude, latency, and the kinetics of the decay. The distributions of amplitude and latency are unimodal suggesting that they arise from a single population while the decay kinetics are bimodal, suggesting that they represent two cell types. Future experiments will correlate decay kinetics with other morphological properties to determine if these are distinct developing ipRGC types.

Introduction

Intrinsically photosensitive retinal ganglion cells (ipRGCs) are the first known source of light detection. In contrast with rod and cone photoreceptors, ipRGCs, as all retinal ganglion cells (RGCs) are, projection neurons that relay information from the retina directly to the brain. Similar to photoreceptors, ipRGCs express an opsin protein that enables their photosensitivity (Panda et al. 2005). Some reports indicate that ipRGC-dependent light detection starts in embryonic mice, long before maturation of canonical photoreceptors (Olney 1968), and influences eye development (Rao et al. 2013), and the development of retinopathy later in life (Panda et al. 2005; Yang et al. 2013). The understanding of the physiology, anatomy, and functionality of ipRGCs has grown tremendously over the last couple of decades (Olney 1968; Schmidt, Do, et al. 2011; Do & Yau 2010). However, an overwhelming majority of our ipRGC knowledge is based on adult organisms, especially mouse, while the properties and functions of developing ipRGCs are not as well understood.

There are at least five subtypes of ipRGCs in the adult retina (Rao et al. 2013; Hu et al. 2013; Ecker et al. 2010). IpRGC subtype classifications are based on several factors including dendritic morphology, stratification, projection targets in the brain and the responses to light. In independent studies in the developing retina, 3 subtypes have been identified based on their light response properties as measured with a multielectrode array (Tu et al. 2005). The source of this difference could be due to the method of classification but it is also possible that ipRGC differentiation continues into adulthood. Furthermore, light responses recorded in patch-clamp and morphological analysis of ipRGCs have not yielded distinguishable ipRGC types in the developing retina (Schmidt et al. 2008). Here, we use calcium imaging to attempt to classify the light responses of ipRGCs in the developing retina.

Together our data indicate that, under our experimental conditions, the light responses of developing ipRGCs, as determined by calcium imaging, are highly diverse but for the most part do not provide insights into different types of ipRGCs. One exception is the decay properties of the light response, which show potential as a classifier of ipRGC subtypes.

Methods

Animals and sample preparation, as it appears in Chapter III:

Animals. All experiments were performed on mice aged postnatal day P4–P7 of either sex from C57BL/6 WT (Harlan Laboratories, Indianapolis) or Opn4-EGFP (P. Kofuji, Minnesota University, Minneapolis(Schmidt et al. 2008)) lines. Animal procedures were approved by the University of California, Berkeley Institutional Animal Care and Use Committees and conformed to the National Institutes of Health Guide for the Care and Use of Laboratory Animals, the Public Health Service Policy, and the Society for Neuroscience Policy on the Use of Animals in Neuroscience Research. Animals were anesthetized with isofluorane and decapitated, and the eyes were enucleated. Retinas were removed from eyecups in 95% O2–5% (vol/vol) CO2 bicarbonate buffered artificial cerebrospinal fluid (ACSF, in mM: 119 NaCl, 26.2 NaHCO3, 11 glucose, 2.5 KCl, 1 K2HPO4, 2.5 CaCl2, 1.3 MgCl2).

Whole-mount retinal preparations. Isolated retinas were mounted RGC-side up on filter paper. Retinas were dark adapted for at least 30 minutes at room temperature in oxygenated ACSF until transfer to the recording chamber, where they were continually superfused (1–2 ml/min) with oxygenated ACSF at 29–32°C.

Calcium imaging and visual stimulation. Retinas were bulk loaded with the calcium indicator Oregon Green BAPTA-1 AM (OGB-1) using the multi-cell bolus loading technique and epifluorescent imaging described previously (Blankenship et al. 2009). Excitation light was filtered with a 470/40 optical filter and yielded approximately 3.4 x 10^{15} photons $s^{-1}cm^{-2}$ to maximally stimulate the ipRGC intrinsic light response. Time series images of 30 or 40 seconds were acquired at 2 Hz with a 225 ms exposure time using a 40X water immersion objective. Elliptical regions of interest were drawn automatically with an ImageJ algorithm that identifies cells displaying increases in fluorescence within the first 7 seconds after imaging onset. Cells were classified as light responsive if they exhibited ΔF/F above threshold within 7 s of light onset. Thresholds was defined as ΔF/F = 1%.
ΔF/F was defined as:

$$\Delta F/F = \frac{F_n - F_i}{F_i}$$

where F_n is the raw F value at a given time point and F_i is s constant given by the initial F value (baseline F), measured at the onset of visual stimulation. We chose this method to fit the relatively slow kinetics of the light-evoked calcium transients in ipRGCs.

Light response properties and correlations.
Peak amplitude,

$$(\frac{\Delta F}{F})_{max} = \frac{F_{max} - F_i}{F_i}$$

where F_{max} corresponds to the maximum F value within the first 7 seconds of visual stimulation, and F_i is the F value at baseline fluorescence.

Peak latency (t_{max}) is the time value at which F_{max} is found.

Response decay (R_t) is computed by the following quantity,

$$R_t = \frac{(\Delta F/F)_{max} - (\Delta F/F)_{t_{max}+n}}{(\Delta F/F)_{max}}$$

where n is a length of time, in seconds, assigned deliberately and $(\Delta F/F)_{t_{max}+n}$ is the ΔF/F value measured n seconds after peak amplitude. We used n values of 5s, 10s, and 15s. This quantity corresponds to the fraction of the peak that has decayed.

Statistical analysis. Correlation coefficients were obtained with the Matlab function 'corrcoef'. Linear fit were obtained with the Matlab 'basic fitting' tool. Normal fits to the distributions were plotted with the Matlab function 'histfit'. Normal distribution plots were obtained with the Matlab function 'normplot'. Bimodal distributions were obtained with the Matlab function 'fit', integrating the function 'fitoptions' to specify a 'NonLinearLeastSquare' method.

Results

Light response properties of developing ipRGCs assessed with calcium imaging

We first wanted to use calcium imaging to characterize the properties of ipRGC light responses in the developing retina (postnatal days 4 – 7). Previous studies have used extracellular patch clamp techniques (Schmidt et al. 2014) or calcium imaging (Sekaran et al. 2005). Only experiments using extracellular recordings of light-evoked action potential firing have been able to classify developing ipRGCs into different types (Tu et al. 2005; Sexton et al. 2015). Here, we used the calcium imaging data acquired in the experiments described in Chapter II (Arroyo et al. 2016) to identify the cells that exhibited light responses in control conditions (Figure 1A). As expected, ipRGC light responses exhibited high diversity in terms of latency, response amplitude, and response decay (Figure 1B). This observation was confirmed by the large variation of the average response for 20 random cells (Figure 1C). The observed diversity in the properties of ipRGC light responses is consistent with previous studies that have used action potentials to characterize ipRGCs (Schmidt et al. 2008; Tu et al. 2005).

We analyzed several properties of ipRGC light-evoked calcium transients. First, we computed peak amplitude as the difference between the largest value of the calcium transient $\Delta F/F$ during the light response and the value at the baseline signal, before light response onset. The peak amplitude of the response exhibited a normal distribution centered at $\Delta F/F = 7.0 \pm 2.0\%$ (average ± standard deviation, Figure 1D, Table 1, n = 1765 cells). Second, we computed peak latency as the time point at which the peak occurs. The histogram distribution of peak latency data was complex but did not exhibit a clear multimodal distribution at 4.5 ±2.2 seconds (Figure 1E, Table 1, n = 1765 cells), which is notably shorter than the previously reported shortest latency of approximately 20 seconds. (Sekaran et al. 2005; Tu et al. 2005; Schmidt et al. 2008). Note that other latency parameters where explored but were determined to be imprecise measures due to our sampling rate of 2 Hz, discussed below. Lastly, we analyzed the signal decay of the responses by computing the percentage of signal reduction 10 seconds after peak time. The signal decay data had a bimodal distribution, rather than unimodal. Several responses fell at the right tail of the distribution indicating that a major portion of cell responses cells decay almost completely 10 seconds after peak time (Figure 1F, Table 1, mean = 62.8 ±29.7%, n = 1315 cells). Together our data suggest that response decay might be more useful than amplitude or latency for classifying developing ipRGCs into different types. It should be noted that similar parameters have been used to describe light-evoked calcium transients in developing ipRGCs, using different light stimulation and imaging protocols (Sekaran et al. 2005).

Table 1 displays a complete list of the analyzed light response properties and the estimated soma size of developing ipRGCs.

Response decay of ipRGC light responses fall into bimodal distributions

While previous studies that looked at light-evoked action potential firing have mainly focused on latency, sensitivity and intensity of the light responses to assign developing ipRGCs to different types (Tu et al. 2005; Sexton et al. 2015), little is known about the response decay as a classifying parameter. We chose time points of 5, 10 and 15 seconds after the determined peak time for each cell and computed the fractional decay. In order to determine which of the time points would be most effective at separating light responses we first plotted normal probability plots (see Methods) to observe the cumulative distribution of the decay data for each time point against their theoretical normal cumulative distribution (Figure 2 A-C, black '+' = data points, red line = theoretical normal cumulative distribution). Histogram distributions of percentage decay for all three times showed marked departures from normality, particularly for cells with larger decay values. The departure from normality of the data was indicative that the data is sampled from more than one population, as expected from distribution for response decay at 10 seconds in Figure 1F.

Next, we fitted the response decay distributions to bimodal curves in order to reveal different response types. First, the response decay at 5 seconds post-peak time exhibited a large peak at low decay values and a more uniform distribution at larger decay values (Figure 2D). This bias in the distribution suggests that at 5 seconds post-peak time most cells show little response decay, thus 5 seconds might not be long enough to observe separation of the responses. Second, the response decay at 10 seconds post-peak time exhibited a fairly bimodal distribution with a large peak at the larger decay values (Figure 2E). This distribution suggests that at 10 seconds post-peak time there are at least two type of responses, slow decaying (long) responses and fast decaying (short) responses, with a possible third type of responses for which decay approached baseline signal. Third, the response decay 15 seconds post-peak time exhibited two smaller peaks, resembling response decay data at 10 seconds, with a very large peak at the tail end of the distribution (Figure 2F). This distribution suggests that a large portion of the responses have already decayed to baseline levels. Also note that the large amount of data at the tail end of the distribution might be throwing off the bimodal fit curve.

To test how separating the responses with faster decays would affect the distribution of cells with intermediate and slow decays we eliminated cells with response decay greater than 0.95%. This exclusion had little effect on the response decay at 5 seconds post-peak (Figure 2G), it seemed to slightly improve the bimodal distribution of response decay at 20 seconds post-peak (Figure 2H), and it notably improved the bimodal fit of the response decay at 15 seconds post peak.

We separated cells into 3 groups by dividing the data at or near the middle of the double peak and treating the largest decays (>95%) as a different group. Such partition would yield slow, moderate, and fast decaying groups of responses. These data are summarized in Table 2. While

the number of cells distributes more even among the 3 groups at 10 and 15 seconds, as opposed to 5 seconds post-peak, further experimental evidence is needed to confirm this suggestion.

Correlation analysis of light response properties

What physiological properties are represented by response decay? Classically, decay kinetics of calcium transients are thought to be dominated calcium clearance, such as by calcium pumps, which is modeled by a single exponential, quite different from the complex decay kinetics we observed. For ipRGCs, response decay may reflect the time course of action potential firing of ipRGCs, which are often quick bursts of action potentials followed by lower frequency sustained firing (Kirkby & Feller 2013).

To test whether response decay is an independent parameter from response amplitude or latency, we studied the cell-by-cell correlation of these parameters as a function of response decay (Figure 3). Our data does not indicate strong correlations between any pair of light response properties. However, the stronger correlations were observed comparing peak latency with response decay (Figure 3 A-C), and peak amplitude with response decay (Figure 3 D-F). In all cases, we observed rather weak negative correlation coefficients indicating that response decay is independent of response amplitude and latency. Note that comparing response amplitude and peak latency yields a very small correlation coefficient (0.15). All our correlation data are summarized in Table 3.

Baseline fluorescence, measured before light stimulation, does not appear to be correlated with either response amplitude or peak time (Table 3), indicating that our calcium indicator sensitivity did not influence the response decay.

Discussion

There are at least five well defined types of ipRGCs in the adult retina, distinguished by their physiological and anatomical properties (Hu et al. 2013; Schmidt, Chen, et al. 2011), their brain projections (Hattar et al. 2002), and their function (Lucas et al. 2003). Much less is understood about the different ipRGC types in developing animals. As a general population we know that developing ipRGCs are involved in important functions such as development of eye vasculature (Rao et al. 2013), and light-guided behavior (Delwig et al. 2012; Johnson et al. 2010). However whether specific types of developing ipRGCs mediate specific functions of developing ipRGCs is unknown. New ways of identifying and studying developing ipRGCs would facilitate access to ipRGC type to function designation in developing animals.

Our work describes properties of ipRGC light responses as characterized by calcium imaging in the developing retina. We have complemented previous work that characterized ipRGC early light response with electrophysiological methods (Schmidt et al. 2008; Tu et al. 2005) and expanded similar calcium imaging studies (Sekaran et al. 2005).

Under our experimental conditions, light responses of developing ipRGCs show unimodal distributions for response amplitude, peak latency, baseline signal, and size. It is well established that developing ipRGCs are a diverse group in terms of physiological and morphological properties (Tu et al. 2005; Schmidt et al. 2008; Arroyo et al. 2016). Indeed, the before mentioned properties showed large variations, however they exhibited normal distributions which suggests a single population rather than separable types.

Interestingly, the decay of the observed light responses showed potential as a property that can be used for classifying subtypes of ipRGCs. The distribution of response decay at 10 or 15 seconds post-peak time exhibited bimodal distributions. Separating cells with fully decayed light responses improved bimodal distribution of the data. Thus, we propose that the response decay of developing ipRGC could potentially be used to distinguish ipRGC types in the developing retina. Further research is necessary to assess the relationship between response decay and other ipRGC properties in the developing retina. This would expand our knowledge of ipRGC types and their development. It should be noted that our decay analysis was limited by cholinergic retinal waves. Since waves happen periodically at about 1 per minute (Feller et al. 1996) we chose short post-peak times in order to decrease the likelihood of contamination with wave-induced increases in signal.

Light-sensitivity and response latency are known to distinguish ipRGCs types in development and adulthood (Sexton et al. 2015; Tu et al. 2005; Hu et al. 2013). However this information is inaccessible with our current data. First, our light stimulation is acquired with a fixed intensity optimized for the calcium imaging which is an order of magnitude above the reported ipRGC

maximal stimulation (see Mehods). Based on previous studies, our experimental conditions would yield mostly short peak latencies (Sexton et al. 2015; Tu et al. 2005). Additionally, response onset parameters are different for specific ipRGC types. However, we observed very fast rise times that were too fast relative to our sampling rate and thus response onsets cannot be appropriately resolved.

Lastly, we analyzed correlations between the response decay and response amplitude and latency of developing ipRGC. For the most part we observed rather small correlation coefficients. Our data suggests that the different light-evoked calcium transient properties of developing ipRGCs are mostly independent from one another. Thus, we conclude that response decay is an independent property of developing ipRGCs and that it is unlikely to be confounded by the kinetics of our calcium indicator.

In the future we will compare these response properties to cells that gain a light response Chapter III Figure III-1). Using this strategy we will determine if light responses as measured with calcium imaging can be used to distinguish ipRGCs in control conditions from those that gain a light response.

References

Arroyo, D.A., Kirkby, L.A. & Feller, M.B., 2016. Retinal Waves Modulate an Intraretinal Circuit of Intrinsically Photosensitive Retinal Ganglion Cells. *The Journal of neuroscience : the official journal of the Society for Neuroscience*, 36(26), pp.6892–6905.

Blankenship, A.G. et al., 2009. Synaptic and extrasynaptic factors governing glutamatergic retinal waves. *Neuron*, 62(2), pp.230–241.

Delwig, A. et al., 2012. Light evokes melanopsin-dependent vocalization and neural activation associated with aversive experience in neonatal mice. *PloS one*, 7(9), pp.e43787–e43787.

Do, M.T.H. & Yau, K.W., 2010. Intrinsically Photosensitive Retinal Ganglion Cells. *Physiological Reviews*, 90(4), pp.1547–1581.

Ecker, J.L. et al., 2010. Melanopsin-expressing retinal ganglion-cell photoreceptors: cellular diversity and role in pattern vision. *Neuron*, 67(1), pp.49–60.

Feller, M.B.M. et al., 1996. Requirement for cholinergic synaptic transmission in the propagation of spontaneous retinal waves. *Science*, 272(5265), pp.1182–1187.

Hattar, S. et al., 2002. Melanopsin-containing retinal ganglion cells: architecture, projections, and intrinsic photosensitivity. *Science (New York, N.Y.)*, 295(5557), pp.1065–1070.

Hu, C., Hill, D.D. & Wong, K.Y., 2013. Intrinsic physiological properties of the five types of mouse ganglion-cell photoreceptors. *Journal of neurophysiology*, 109(7), pp.1876–1889.

Johnson, J. et al., 2010. Melanopsin-dependent light avoidance in neonatal mice. *PNAS*, 107(40), pp.17374–17378.

Kirkby, L.A. & Feller, M.B., 2013. Intrinsically photosensitive ganglion cells contribute to plasticity in retinal wave circuits. *Proceedings of the National Academy of Sciences of the United States of America*, 110(29), pp.12090–12095.

Lucas, R.J. et al., 2003. Diminished pupillary light reflex at high irradiances in melanopsin-knockout mice. *Science*, 299(5604), pp.245–247.

Olney, J.W., 1968. An electron microscopic study of synapse formation, receptor outer segment development, and other aspects of developing mouse retina. *Investigative ophthalmology*, 7(3), pp.250–268.

Panda, S. et al., 2005. Illumination of the melanopsin signaling pathway. *Science,* 307(5709), pp.600-604.

Rao, S. et al., 2013. A direct and melanopsin-dependent fetal light response regulates mouse eye development. *Nature*, 494(7436), pp.243–246.

Schmidt, T.M. et al., 2014. A role for melanopsin in alpha retinal ganglion cells and contrast detection. *Neuron*, 82(4), pp.781–788.

Schmidt, T.M., Chen, S.-K. & Hattar, S., 2011. Intrinsically photosensitive retinal ganglion cells: many subtypes, diverse functions. *Trends in neurosciences*, 34(11), pp.572–580.

Schmidt, T.M., Do, M.T.H., et al., 2011. Melanopsin-positive intrinsically photosensitive retinal ganglion cells: from form to function. *The Journal of neuroscience : the official journal of the Society for Neuroscience*, 31(45), pp.16094–16101.

Schmidt, T.M., Taniguchi, K. & Kofuji, P., 2008. Intrinsic and extrinsic light responses in melanopsin-expressing ganglion cells during mouse development. *Journal of neurophysiology*, 100(1), pp.371–384.

Sekaran, S. et al., 2005. Melanopsin-dependent photoreception provides earliest light detection in the mammalian retina. *Current biology : CB*, 15(12), pp.1099–1107.

Sexton, T.J. et al., 2015. Type I intrinsically photosensitive retinal ganglion cells of early post-

natal development correspond to the M4 subtype. *Neural development*, 10, p.17.
Tu, D.C. et al., 2005. Physiologic diversity and development of intrinsically photosensitive retinal ganglion cells. *Neuron*, 48(6), pp.987–999.
Yang, M.B. et al., 2013. Length of day during early gestation as a predictor of risk for severe retinopathy of prematurity. *Ophthalmology*, 120(12), pp.2706–2713.

Table 1. Properties of calcium transients based light response and soma size of developing ipRGCs

Parameter	units	n	median	average	std. deviation
peak amplitude	% ΔF/F	1765	6.68	6.99	2.15
peak latency	sec	1765	4	4.54	2.20
Decay* 5 s after peak	%	1315	26.01	36.66	27.44
decay 10 s after peak	%	1315	70.25	62.85	29.68
decay 15 s after peak	%	1308	85.02	74.13	25.62
baseline F (Fi)	F units	1765	843.4	925.5	402.4
Soma size	μm^2	1765	71.70	77.46	42.67

*Decay is computed as the "fraction of the peak that has decayed". See Methods.

Table 2. IpRGC light responses separated by their decay properties

Time of decay	total cells	cells with decay > 95%	cells with small decay*	cells with large decay*
5 sec after peak	1315	49	910	356
10 sec after peak	1315	239	584	492
15 sec after peak	1308	344	455	509

*The threshold value to separate cells with small and large decay values was 45% for 5 sec decay, 60% for 10 sec decay, and 70% for 15 sec decay. Threshold values are an approximate of the midpoint between the two peaks of the bimodal distributions.

Table 3. Correlations of light response properties

Correlation	C.C.*	Linear fit (m / b)**
Peak amp. v decay 5s	-0.33	-0.80 / 1.8
Peak amp. v decay 10s	-0.25	-0.38 / 1.4
Peak amp. v decay 15s	-0.23	-0.25 / 1.2
Peak latency v decay 5s	-0.33	-0.50 / 1.5
Peak latency v decay 10s	-0.39	-0.38 / 1.4
Peak latency v decay 15s	-0.35	-0.25 / 1.2
Peak amp. v baseline F	-0.12	-0.16 / 1.2
Peak amp. v peak latency	0.15	0.24 / 0.76
Peak latency v baseline F	-0.10	-0.11 / 1.1
Baseline v decay 10 s	0.24	0.25 / 0.75

*C.C. = correlation coefficient

** $y = mx + b$

Figure 1. Properties of developing ipRGCs assessed with calcium imaging

A, Left: Fluorescent image of the ganglion cell layer loaded with the calcium indicator OGB-1 BAPTA-AM, average image of the first 30 frames of imaging. Middle: ΔF induced by light stimulation (480nm), baseline F was subtracted from maximal F over the first 7.5 seconds of imaging. Right: Binarized ΔF image to generate regions of interest over the light-responsive cells. Color dots correspond to sample traces shown in B. **B**. ΔF/F over time for sample traces of light-responses from cells indicated in A. Dotted gray line indicates base signal before light stimulation. **C**. Average light response (ΔF/F over time) of 20 random cells. Gray traces indicate the standard deviation. **D**. Histogram distribution for the peak amplitude of the light-evoked response, all cells included (n = 1,765 cells). Red curve represents a gaussian fit of the data. **E**. Histogram distribution for the latency to peak of light-evoked responses (n = 1,765 cells). Red curve represents a gaussian fit of the data. **F**. Histogram distribution for the percent decay of the peak ΔF/F 10 seconds after peak time (n = 1,315 cells). Red curve represents a bimodal fit of the data.

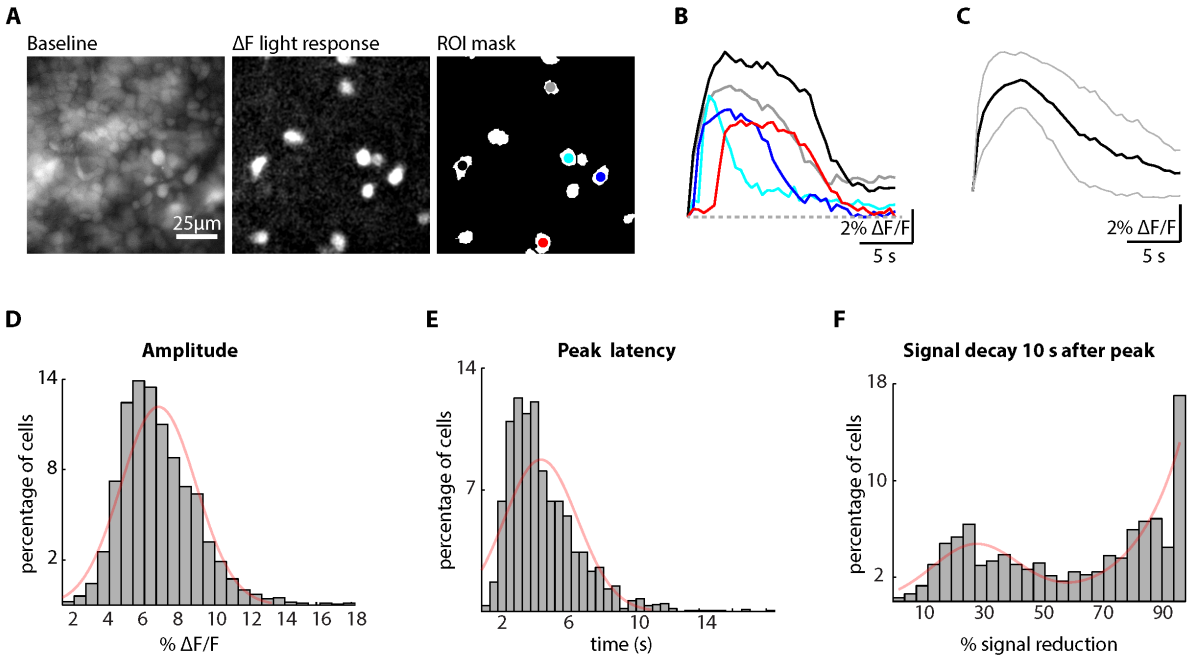
A
Baseline
ΔF light response
ROI mask
25µm
B
2% ΔF/F
5 s
C
2% ΔF/F
5 s
D
Amplitude
percentage of cells
% ΔF/F
E
Peak latency
percentage of cells
time (s)
F
Signal decay 10 s after peak
percentage of cells
% signal reduction

Figure 2. Response decay of ipRGC light responses fall into bimodal distributions

A-C. Cumulative distribution plots for signal decay data; 5 seconds after peak (A), 10 seconds after peak (B), 15 seconds after peak (C). Data points (+) are plotted against a fixed gaussian cumulative distribution (red line) to observe deviation from normality. **D-F**. Histogram distribution for the percentage of ΔF/F decay; 5 seconds after peak time (D), 10 seconds after peak time (E, as in 1F), and 15 seconds after peak time (F). Red curves indicate a bimodal fit to the data. **G-I**. Bimodal fit of signal decay distributions after removing cells with signal decays over 95% (short duration responses). G. 5 seconds after peak time. H. 10 seconds after peak time. F. 15 seconds after peak time.

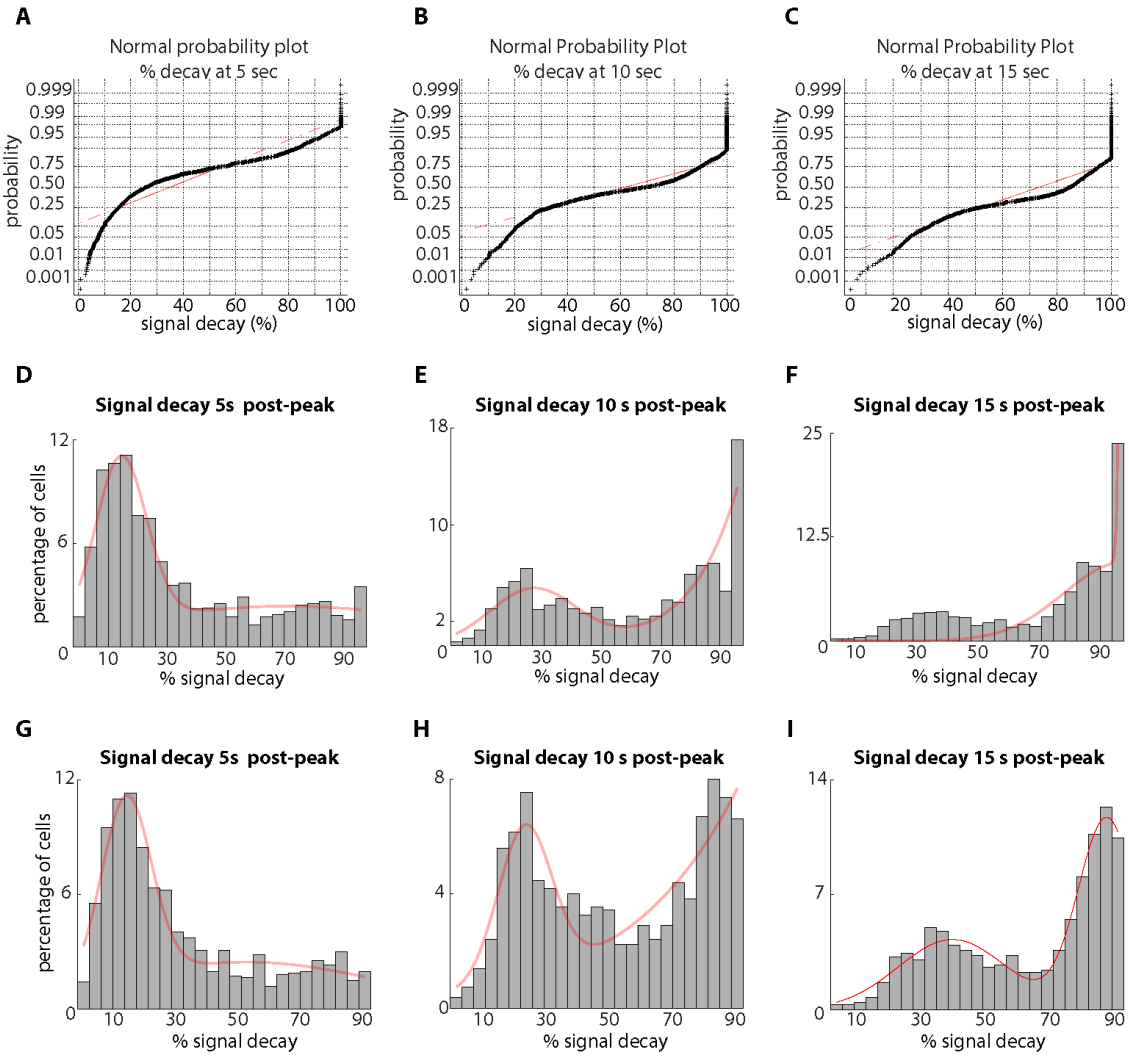
A
Normal probability plot
% decay at 5 sec
probability
0.999
0.99
0.95
0.75
0.50
0.25
0.05
0.01
0.001
0
20
40
60
80
100
signal decay (%)
B
Normal Probability Plot
% decay at 10 sec
probability
signal decay (%)
C
Normal Probability Plot
% decay at 15 sec
probability
signal decay (%)
D
Signal decay 5s post-peak
percentage of cells
12
6
0
10
30
50
70
90
% signal decay
E
Signal decay 10 s post-peak
18
10
2
% signal decay
F
Signal decay 15 s post-peak
25
12.5
% signal decay
G
Signal decay 5s post-peak
percentage of cells
% signal decay
H
Signal decay 10 s post-peak
8
4
% signal decay
I
Signal decay 15 s post-peak
14
7
% signal decay

Figure 3. Correlations of ipRGC light response properties

A-C. Peak amplitude vs. response decay after 5 seconds (D), 10 seconds (E) and 15 seconds (F) of peak, red line indicates the linear fit of the data for all cells. Red line: linear fit to data for computing correlation coefficient. **D-F**. Peak latency vs. response decay after 5 seconds (G), 10 seconds (H) and 15 seconds (I) of peak, red line indicates the linear fit of the data.

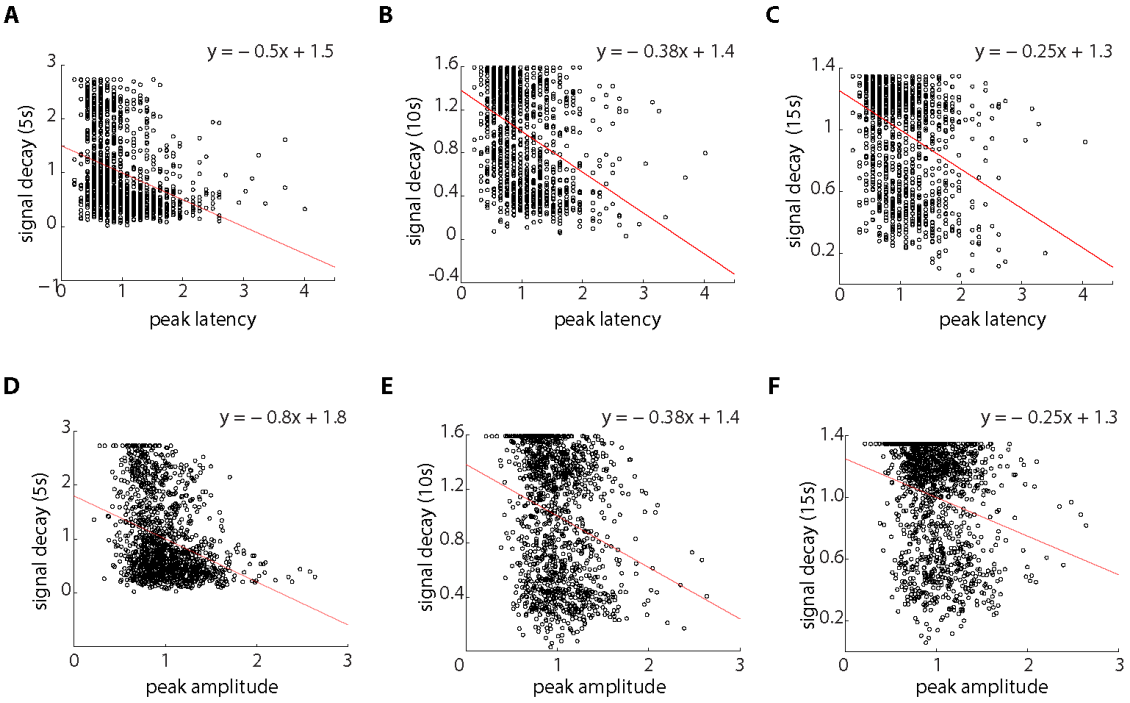
A
y = – 0.5x + 1.5
signal decay (5s)
peak latency
B
y = – 0.38x + 1.4
signal decay (10s)
peak latency
C
y = – 0.25x + 1.3
signal decay (15s)
peak latency
D
y = – 0.8x + 1.8
signal decay (5s)
peak amplitude
E
y = – 0.38x + 1.4
signal decay (10s)
peak amplitude
F
y = – 0.25x + 1.3
signal decay (15s)
peak amplitude